VOLUME 5 NUMBER 1 2018 ISSN 2409-6121

Physical Sciences and Technology

National Nanotechnological Laboratory of Open Type
Institute of Experimental and Theoretical Physics

Physical Sciences and Technology is publishing two number in a year by al-Farabi Kazakh National University, al-Farabi ave., 71, 050040, Almaty, the Republic of Kazakhstan
website: http://phst.kaznu.kz/

Any inquiry for subscriptions should be send to:
Gauhar Mussabek, al-Farabi Kazakh National University
al-Farabi ave., 71, 050040, Almaty, the Republic of Kazakhstan
e-mail: gauharmussabek@gmail.com

SCOPE AND AIM

Physical Sciences and Technology provides an original paperback for the publication of peerreviewed research and review articles in all fields of Physics and related Technology. The topics, included in the scope, especially emphasize understanding of the physics underlying modern technology.

Subject areas may include, but are not limited to the following fields: Astronomy and Space Research, Theoretical Physics and Astrophysics, Plasma Physics and Related Technology, Chemical Physics and Related Technology, Condensed Matter Physics and Related Technology, Thermal physics and Related Technology, Nuclear Physics and Related Technology, Nanomaterials and Nanotechnology, Applied Atomic and Molecular Physics, Material Sciences and Related Technology, Electronics and Related Technology, Instrumentation, Photonics and Quantum Electronics, Signal processing.

The Journal is issued under the auspices of the National Nanotechnological Laboratory of Open Type and Institute of Experimental and Theoretical Physics and is published two times a year by the «Kazakh University» Publishing House. The International Editorial Board of the Journal consists of leading researchers from different countries of the world. The Journal is wide open for contributions that both lie at the far frontiers of contemporary physics and are particularly aimed at applications of the scientific principles of physics to modern technological problems.

IRSTI 29.27.39; 29.27.47.

Plasma expansions in terms of self-similar solutions

M. Murakami

Institute of Laser Engineering, Osaka University, Osaka 565-0871, Japan
e-mail: murakami-m@ile.osaka-u.ac.jp

Simple analytical models are presented for hydrodynamic expansion of laser-produced plasma governed by the nonlinear heat conduction. To neatly describe the fluid systems, we put forward new self-similar solutions, which are very useful to completely reveal the essential behavior of the underlying physics. The targets are assumed to have a limited mass. The physical picture significantly contrasts with that well described by the orthodox self-similar solution for a semi-infinite planar rarefaction wave. The ion energy spectrum obtained by the model reproduces well experimental results obtained under different geometrical conditions. It is strictly shown that the hydrodynamic system of an accelerating foil admits a new self-similar solution describing the nonstationary ablation process, through which the payload mass decreases to burn out at the end. The system is appropriately solved as a novel eigenvalue problem such that the acceleration and the heat conductivity are restrictive with each other under the self-similar evolution.

Key words: laser-plasma acceleration of electrons and ions, two-fluid and multi-fluid plasmas, plasma sheaths, plasma simulation.
PACS numbers: 52.38.Kd, 52.30.Ex, 52.40.Kh, 52.65.-y.

1 Introduction

Dimensional and similarity theory provides one with the possibility of prior qualitative-theoretical analysis and the choice of a set for characteristic dimensionless parameters. The theory can be applied to the consideration of quite complicated phenomena and makes the processing of experiments much easier. What is more, at present, the competent setting and processing of experiments in inconceivable without taking into account dimensional and similarity reasoning. Sometimes at the initial stage of investigation of certain complicated phenomena, dimensional and similarity, theory is the only possible theoretical method, though the possibilities of this method should not be overestimated. The combination of similarity theory with considerations resulting from experiments or mathematical operations can sometimes lead to significant results. Most often dimensional and similarity theory is very useful for theoretical as well for practical use. All the results obtained with the help of this theory can be obtained quite easily and without much trouble.

A phenomenon is called self-similar if the spatial distributions of its properties at various moments of time can be obtained from one another by a similarity transformation. Establishing self-similarity has always represented progress for a researcher: self-similarity has simplified computations and the representation of the characteristics of phenomena under investigation. In handling experimental data, self-similarity has reduced what would seem to be a random cloud of empirical points so as to lie on a single curve of surface, constructed using self-similar variables chosen in some special way. Self-similarity enables us to reduce its partial differential equations to ordinary differential equations, which substantially simplifies the research. Therefore, with the help of self-similar solutions researchers have attempted to find the underlying physics. Self-similar solutions also serve as standards in evaluating approximate methods for solving more complicated problems.

Scaling laws, which are obtained as a result of the dimensional analysis and other methods, play an important role for understanding the underlying physics and applying them to practical systems. When constructing a full-scale system in engineering, numerical simulations will be first made in most cases. Its feasibility should be then demonstrated experimentally with a reduced-scale system. For astrophysical studies, for instance, such scaling considerations are indispensable and play a

decisive role in designing laboratory experiments. Then one should know how to design such a miniature system and how to judge whether two experimental results in different scales are hydrodynamically equivalent or similar to each other. Lie group analysis [1], which is employed in the present chapter, is not only a powerful method to seek self-similar solutions of partial differential equations (PDE) but also a unique and most adequate technique to extract the group invariance properties of such a PDE system. Lig group analysis and dimensional analysis are useful methods to find self-similar solutions in a complementary manner.

An instructive example of self-similarity is given by an idealized problem in the mathematical theory of linear heat conduction: Suppose that an infinitely stretched planar space ($-\infty < x < \infty$) is filled with a heat-conducting medium. At the initial instant $t = 0$ and at the origin of the coordinate $x = 0$, a finite amount of heat E is supplied instantaneously. Then the propagation of the temperature Θ is described by

$$\frac{\partial \Theta}{\partial t} = \kappa \frac{\partial^2 \Theta}{\partial x^2}, \tag{1}$$

where κ is the constant heat diffusivity of the medium. Then the temperature Θ at an arbitrary time t and distance from the origin x is given by

$$\Theta = \frac{E}{c\sqrt{4\pi\kappa t}} \exp\left(-\frac{x^2}{4\kappa t}\right), \tag{2}$$

where c is the specific heat of the medium. As a matter of fact, it is confirmed with the solution (2) that the integrated energy over the space is kept constant regardless of time:

$$\int_{-\infty}^{\infty} c\,\Theta(x,t)dx = E \tag{3}$$

The structure of Eq. (2) is instructive: There exist a temperature scale $\Theta_0(t)$ and a linear scale $x_0(t)$, both depending on time,

$$\Theta_0(t) = \frac{E}{c\sqrt{4\pi\kappa t}}, \quad x_0(t) = \sqrt{\kappa t}, \tag{4}$$

such that the spatial distribution of temperature, when expressed in these scales, ceases to depend on time at least in appearance:

$$\frac{\Theta}{\Theta_0} = f(\xi), \quad f(\xi) = \exp\left(-\frac{\xi^2}{4}\right), \quad \xi = \frac{x}{x_0}. \tag{5}$$

Suppose that we are faced with a more complex problem of mathematical physics in two independent variables x and t, requiring the solution of a system of partial differential equations on a variable $u(x,t)$ of the phenomenon under consideration. In this problem, self-similarity means the we can choose variable scales $u_0(t)$ and $x_0(t)$ such that in the new scales, $u(x,t)$ can be expressed by functions of one variable:

$$u = u_0(t)U(\xi), \quad \xi = x/x_0(t) \tag{6}$$

The solution of the problem thus reduces to the solution of a system of ordinary differential equations for the function $U(\xi)$.

At a certain point of analysis, dimensional consideration called Π-theorem plays a crucial role in a complementary manner to the self-similar method. Suppose we have some relationship defining a quantity a as a function of n parameters $a_1, a_2, \ldots, a_n$:

$$a = f(a_1, a_2, \ldots a_n). \tag{7}$$

If this relationship has some physical meaning, Eq. (7) must reflect the clear fact that although the numbers $a_1, a_2, \ldots, a_n$ express the values of corresponding quantities in a definite system of units of measurement, the physical law represented by this relation does not depend on the arbitrariness in the choice of units. To explain this, we shall divide the quantities $a, a_1, a_2, \ldots a_n$ into two groups. The first group, $a_1, \ldots a_k$, includes the governing quantities with independent dimensions (for example, length, mass, and time). The second group, $a, a_{k+1}, \ldots a_n$, contains quantities whose dimensions can be expressed in terms of dimensions of the quantities of the first group. Thus, for example, the quantity a has the dimensions of the product $a_1^p a_2^q \cdots a_k^r$, the quantity a_{k+1} has the dimensions of the

product $a_1^{p_{k+1}} a_2^{q_{k+1}} \cdots a_k^{r_{k+1}}$, etc. The exponents $p, q, \ldots$ are obtained by a simple arithmetic. Thus the quantities,

$$\Pi = \frac{a}{a_1^p a_2^q \cdots a_k^r},$$

$$\Pi_1 = \frac{a_{k+1}}{a_1^{p_{k+1}} a_2^{q_{k+1}} \cdots a_k^{r_{k+1}}}, \ \ldots, \tag{8}$$

$$\Pi_{n-k} = \frac{a_n}{a_1^{p_n} a_2^{q_n} \cdots a_k^{r_n}},$$

turn out to be dimensionless, so that their values do not depend how one choose the units of measurement. This fact follows that the dimensionless quantities can be expressed in the form,

$$\Pi = \Phi(\Pi_1, \Pi_2, \ldots, \Pi_{n-k}), \tag{9}$$

where no dimensional quantity is contained. What should be stressed is that in the original relation (7), $n+1$ dimensional quantities $a, a_1, a_2, \ldots, a_n$ are connected, while in the reduced relation (9), $n-k+1$ dimensionless quantities Π, $\Pi_1, \Pi_2, \ldots, \Pi_{n-k}$ are connected with k quantities being reduced from the original relation.

We now apply dimensional analysis to the heat conduction problem considered above. Below we shall use the symbol [a] to give its dimension, as Maxwell first introduced, in terms of the unit symbols for length, mass, and time by the letters L, M, and T, respectively. For example, velocity v has its dimension $[v] = L/T$. Then the physical quantities describing the present system have following dimensions,

$$\begin{aligned} &[x] = L, \ \ [t] = T, \ \ [\kappa] = L^2 T^{-1}, \\ &[E] = ML^2 T^{-2}, \ \ [c\,\Theta] = ML^3 T^{-2}. \end{aligned} \tag{10}$$

From Eq. (10), in which five dimensional quantities $(n+1=5)$ under the three principal dimensions ($k=3$ for L, M, and T), one can construct the following dimensionless system with two dimensionless parameters Π and ξ $(=\Pi_1)$:

$$\Pi = f(\xi), \quad \Pi = \frac{c\,\Theta\sqrt{\kappa t}}{E}, \quad \xi = \frac{x}{\sqrt{\kappa t}}, \tag{11}$$

where f is unknown function. Substituting Eq. (11) for Eq. (1), one obtains,

$$f'' + \frac{1}{2}(f + \xi f') = 0, \tag{12}$$

where the prime denotes the derivative with respect to ξ; also the transform relation from partial to ordinary derivatives

$$\begin{aligned} \frac{\partial f(\xi)}{\partial t} &= -\frac{\xi}{2t} f'(\xi), \\ \frac{\partial f(\xi)}{\partial x} &= \frac{1}{\sqrt{\kappa t}} f'(\xi), \end{aligned} \tag{13}$$

are used. With the help of the boundary condition, $f'(0) = 0$, and Eq. (3), Eq. (12) is integrated to give

$$f(\xi) = \frac{1}{\sqrt{4\pi}} \exp\left(-\frac{\xi^2}{4}\right). \tag{14}$$

Thus Eqs. (11) and (14) reproduce the solution of the problem, Eq. (2).

What is described above is the simple and essential scenario of the approach in terms of self-similar solution and dimensional analysis, more details of which can be found, for example, in Refs. [1-4]. In the following subsections, we show three specific examples with new self-similar solutions, as reviews of previously published papers for readers' further understanding how to use the dimensional analysis and to find self-similar solutions: The first is on plasma expansion of a limited mass into vacuum, in which two fluids composed of cold ions and thermal electrons expands via electrostatic field [5]. The second is on laser-driven foil acceleration due to nonlinear heat conduction [6]. Finally, the third is an astrophysical problem, in which self-gravitation and non-linear radiation heat conduction determines the temporal evolution of star formation process in a self-organizing manner [7].

2 Isothermally expansion of laser-plasma with limited mass

Plasma expansion into a vacuum has been a subject of great interest for its role in basic physics and its many applications, in particular, its use in lasers. The applied laser parameter spans a wide range, $10^{10} \le \hat{I}_L \hat{\lambda}_L^2 \le 10^{19}$, where $\hat{I}_L$ is the laser

intensity normalized by $10^{11}\ W/cm^2$ and $\hat{\lambda}_L$ is the laser wavelength normalized by $1\ \mu m$ and. For $\hat{I}_L\hat{\lambda}_L^2 \geq 10^{14}$, generation of fast ions is governed by hot electrons with an increase in $\hat{I}_L\hat{\lambda}_L^2$. In this subsection, we focus on rather lower intensity range, $10^{10} \leq \hat{I}_L\hat{\lambda}_L^2 \leq 10^{14}$, where the effect of hot electrons is negligibly small and background cold electrons can be modeled by one temperature. Typical examples of applications for this range are laser driven inertial confinement fusion [8] and laser-produced plasma for an extreme ultra violet (EUV) light source [9]. As a matter of fact, the experimental data employed below for comparison with the analytical model were obtained for the EUV study. Theoretically, this topic had been studied only through hydrodynamic models until the early 1990s. In such theoretical studies, a simple planar (SP) self-similar solution has often been used [10]. In the SP model, a semi-infinitely stretched planar plasma is considered, which is initially at rest with unperturbed density ρ_0. At $t = 0$, a rarefaction wave is launched at the edge to penetrate at a constant sound speed c_s into the unperturbed uniform plasma by being accompanied with an isothermal expansion. The density and velocity profiles of the expansion are given by [11] $\rho = \rho_0 \exp[-(1 + x/(c_s t)]$ and $v = c_s + x/t$, respectively. The solution is indeed quite useful when using relatively short laser pulses or thick targets such that the density scale can be kept constant throughout the process.

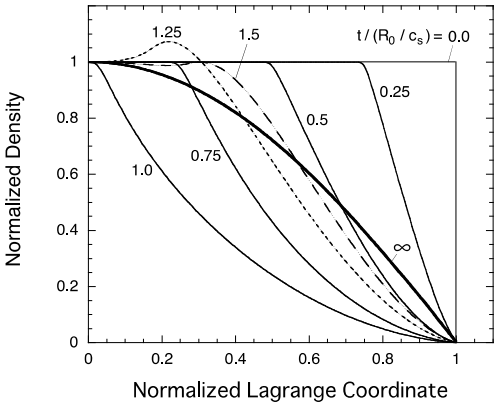

Figure 1 – Temporal evolution of the density profile of a spherical isothermal plasma, which is normalized by that at the center; R_0 and c_s are the initial radius and the sound speed, respectively. After the rarefaction wave reflects at the center, the density distribution asymptotically approaches its final self-similar profile (the thick curve with "∞").

However, in actual laser-driven plasmas, a shock wave first penetrates the unperturbed target instead of the rarefaction wave. Once this shock wave reaches the rear surface of a finite-sized target and the returning rarefaction wave collides with the penetrating rarefaction wave, the entire region of the target begins to expand, and thus the target disintegration sets in. If the target continues to be irradiated by the laser even after the onset of target disintegration, the plasma expansion and the resultant ion energy spectrum are expected to substantially deviate from the physical picture given by the SP solution. Figure 1 demonstrates a simplified version of the physical picture mentioned above with temporal evolution of the density profile obtained by hydrodynamic simulation for an isothermal expansion. A spherical target with density and temperature profiles being uniform is employed as an example. In Figure 1, the density is always normalized by one at the center, and the labels assigned to each curve denote the normalized time $t/(R_0 c_s)$, where R_0 is the initial radius. The horizontal Lagrange coordinate is normalized to unity at the plasma edge. It can be discerned from Figure 1 that the profile rapidly develops in the early stage for $t/(R_0 c_s) \leq 1$. After the rarefaction wave reflects at the center, the density distribution asymptotically approaches its final self-similar profile (the thick curve with label "∞"), which is expressed in the Gaussian form, $\rho \propto \exp[-(r/R)^2]$ as will be derived below. The initial and boundary conditions employed in Figure 1 are substantially simplified such that the laser-produced shock propagation and resultant interactions with the rarefaction wave are not described. However, the propagation speeds of the shock and rarefaction waves are always in the same order as the sound speed c_s of the isothermally expanding plasma. Therefore the physical picture shown in Figure 1 is expected to be qualitatively valid also for realistic cases. Below, we present a self-similar solution for the isothermal expansion of limited masses [5]. The solution explains plasma expansions under relatively long laser pulses or small-sized targets so that the solution responds to the above argument on target disintegration. Note that other self-similar solutions of isothermal plasma expansion have been found for laser-driven two-fluid expansions in light of ion acceleration physics [9] and heavy-ion-driven cylindrical x-ray converter [12], though they are not discussed here.

2.1. Isothermal expansion

The plasma is assumed to be composed of cold ions and electrons described by one temperature T_e, which is measured in units of energy as follows. Furthermore, the electrons are assumed to obey the Boltzmann statistics,

$$n_e = n_{ec} \exp(e\Phi/T_e) , \tag{15}$$

where $n_{ec}(t)$ is the temporal electron density at the target center, e is the elementary charge, and $\Phi(r,t)$ is the electrostatic potential, the zero-point of which is set at the target center, i.e., $\Phi(0,t) = 0$. The potential Φ satisfies the Poisson equation,

$$\frac{1}{r^{\alpha-1}}\frac{\partial}{\partial r}\left(r^{\alpha-1}\frac{\partial \Phi}{\partial r}\right) = 4\pi e(n_e - Zn_i) , \tag{16}$$

where Z is the ionization state; the superscript α stands for the applied geometry such that α = 1, 2, and 3 correspond to planar, cylinder, and spherical geometry, respectively. Throughout the present analysis, the electron temperature T_e and the ionization state Z are assumed to be constant in space and time.

An ion in the plasma is accelerated via the electrostatic potential in the form,

$$\frac{\partial v}{\partial t} + v\frac{\partial v}{\partial r} = -\frac{Ze}{m_i}\frac{\partial \Phi}{\partial r} , \tag{17}$$

where m_i is the ion mass and v is the ion velocity. Note that, in the following, we consider such a system that the plasma has quasi-neutrality, i.e., $n_e \approx Zn_i$, where n_i and n_e are the number densities of the ions and the electrons, respectively. Equations (15) and (17) are combined to derive a single-fluid description,

$$\frac{\partial v}{\partial t} + v\frac{\partial v}{\partial r} = -\frac{c_s^2}{\rho}\frac{\partial \rho}{\partial r} , \tag{18}$$

where $c_s = \sqrt{ZT_e/m_i}$ is the sound speed. Also, a fluid element with mass density $\rho(r,t) = m_i n_i$ satisfies the following mass conservation law,

$$\frac{\partial \rho}{\partial t} + \frac{1}{r^{\alpha-1}}\frac{\partial}{\partial r}(r^{\alpha-1}\rho v) = 0 . \tag{19}$$

We now seek a self-similar solution to Eqs. (18) and (19) on $\rho(r,t)$ and $v(r,t)$ under the similarity ansatz,

$$v = \dot{R}\xi , \ \ \xi \equiv \frac{r}{R} , \tag{20}$$

$$\rho = \rho_{00}\left(\frac{R}{R_0}\right)^{-\alpha} G(\xi), \tag{21}$$

where $R(t)$ stands for a time-dependent characteristic system size, and ξ is the dimensionless similarity coordinate; the over-dot in Eq. (20) denotes the derivative with respect to time; $\rho_{00} \equiv \rho(0,0)$ and $R_0 \equiv R(0)$ are the initial central density and the size, respectively; $G(\xi)$ is a positive unknown function with the normalized boundary condition $G(0) = 1$. Then, Eqs. (15) and (21) give

$$n_e \approx n_{ec}(t)G(\xi) \approx Z\frac{\rho_{00}}{m_i}\left(\frac{R}{R_0}\right)^{-\alpha} G(\xi), \tag{22}$$

Under the similarity ansatz, Eqs. (20) and (21), the mass conservation, Eq. (19), is automatically satisfied. Substituting Eqs. (20) and (21) for Eq. (18), and making use of the derivative rules, $\partial/\partial r = R^{-1}(d/d\xi)$ and $\partial/\partial t = -\xi\dot{R}R^{-1}(d/d\xi)$, one obtains the following ordinary differential equations in the form of variable separation,

$$\frac{R\ddot{R}}{c_s^2} = -\frac{G'}{\xi G} = \psi_0 , \tag{23}$$

where $\psi_0(>0)$ is a separation constant, and the prime denotes the derivative with respect to ξ. Without losing generality, the constant ψ_0 can be set equal to an arbitrary numerical value, because this is always possible with a proper normalization of R and ξ. Here, just for simplicity, we set $\psi_0 = 2$ in Eq. (23). Then the spatial profile of the density, $G(\xi)$, is straightforwardly obtained under $G(0) = 1$ in the form [13-14],

$$G(\xi) = \exp(-\xi^2) . \tag{24}$$

As was seen in Figure 1, the density profile of isothermally expanding plasma with a limited mass is found to approach asymptotically the solution, Eq. (24), even if it has a different profile in the beginning. Meanwhile, $R(t)$ in Eq. (23) cannot be given explicitly as a function of time but has the following integrated forms,

$$\dot{R} = 2c_s\sqrt{\ln(R/R_0)}\,, \tag{25}$$

$$\frac{c_s t}{R_0} = \frac{1}{2}\int_1^{RR_0} \frac{dx}{\sqrt{\ln x}}\,, \tag{26}$$

where in obtaining Eqs. (25) and (26), the system is assumed to be initially at rest, i.e., $\dot{R}(0) = 0$. Here it should be noted that Eqs. (23) - (26) do not explicitly include the geometrical index α, and therefore they apply to any geometry.

Based on the solution given above, some other important quantities are derived as follows. First, the total mass of the system M_0 is conserved and given with the help of Eqs. (21) and (24) in the form,

$$M_0 == (4\pi)_\alpha \rho_{00} R_0^\alpha \int_0^\infty \xi^{\alpha-1} \times \\ \times \exp(-\xi^2)\, d\xi = \left(\sqrt{\pi}R_0\right)^\alpha \rho_{00}\,, \tag{27}$$

with

$$(4\pi)_\alpha \equiv \begin{cases} 2, & (\alpha = 1) \\ 2\pi, & (\alpha = 2) \\ 4\pi, & (\alpha = 3) \end{cases} = \frac{2\pi^{\alpha/2}}{\Gamma(\alpha/2)}\,, \tag{28}$$

where Γ is the Gamma function. Although the quantitative meaning of $R(t)$ was somewhat unclear when first introduced in Eq. (20), it can be now clearly understood by relating it to the temporal central density, $\rho_c(t) \equiv \rho(0,t) \approx m_i n_{ec}(t)/Z$, with the help of Eqs. (21) and (27) in the form,

$$R(t) = \frac{1}{\sqrt{\pi}}\left(\frac{M_0}{\rho_c(t)}\right)^{1/\alpha}. \tag{29}$$

Additionally the potential Φ and corresponding electrostatic field $E = -\nabla\Phi$ are obtained from Eqs. (15), (21), (22), and (24) in the following forms,

$$\frac{e\Phi}{T_e} = -\xi^2\,, \tag{30}$$

$$\frac{eE}{T_e} = \frac{2\xi}{R}\,. \tag{31}$$

The above field quantities contrast well with the fields of the SP solution obtained for a semi-infinitely stretched planar plasma: $e\Phi/T_e = -1 - x/c_s t$ and $eE/T_e = 1/c_s t$ for $x/c_s t \geq -1$ and $t > 0$. It is here worth emphasizing that the electrostatic field increases linearly with ξ for the present model, while it is constant in space for the SP model. Furthermore, the kinetic energy of the system $E_k(t)$ is given with the help of Eqs. (20), (21) and (27) by

$$E_k = \frac{(4\pi)_\alpha}{2}\rho_{00}R_0^\alpha \dot{R}^2 \int_0^\infty \xi^{\alpha+1} \times \\ \times \exp(-\xi^2)\, d\xi = \frac{\alpha}{4} M_0 \dot{R}^2, \tag{32}$$

while the internal (thermal) energy of the system $E_i(t)$ is kept constant,

$$E_i = \frac{3M_0 Z T_e}{2m_i} = \frac{3}{2} M_0 c_s^2\,. \tag{33}$$

Correspondingly, the power required to keep the isothermal expansion, $P(t) = dE_k/dt$, is given from Eqs. (23), (25), and (32) in the form,

$$P/P_0 = \sqrt{\ln(R/R_0)}\,/(R/R_0\,), \tag{34}$$

where $P_0 = 2\alpha M_0 c_s^3/R_0$.

The ion energy spectrum is a physical quantity of high interest. In the present model, the kinetic energy of an ion in flight directly relates its location, in other words, the further an ion is located, the faster it flies. Then, the number of ions contained in an infinitesimally narrow area of the similarity coordinate between ξ and $\xi + d\xi$ is given by

$$dN = (4\pi)_\alpha n_{i00} R_0^\alpha \xi^{\alpha-1} \exp(-\xi^2)\, d\xi\,, \tag{35}$$

where $n_{i00} = \rho_{00}/m_i$ is the initial number density of the ions at the center. Meanwhile, the kinetic energy of an ion at ξ is $\varepsilon = m_i \dot{R}^2 \xi^2/2$, and therefore

$$d\varepsilon = m_i \dot{R}^2 \xi d\xi\,. \tag{36}$$

From Eqs. (35) and (36), the ion energy spectrum is obtained,

$$\frac{d\hat{N}}{d\hat{\varepsilon}} = \frac{\hat{\varepsilon}^{(\alpha-2)/2}\exp(-\hat{\varepsilon})}{\Gamma(\alpha/2)}, \quad (37)$$

where $\hat{N} \equiv N/N_0$ and $\hat{\varepsilon} \equiv \varepsilon/\varepsilon_0$ are normalized quantities with

$$\varepsilon_0(t) = m_i\dot{R}^2/2\,, \quad (38)$$

$$N_0 = (\sqrt{\pi}R_0)^{\alpha} n_{i00}\,. \quad (39)$$

It should be noted that, for α = 3, the energy spectrum, Eq. (37), coincides with the well-known Maxwellian energy distribution; this is not just a coincidence because an isotropically heated mass always has such a distribution.

Although the spectrum, Eq. (37), is for the ion number density, another spectrum for the energy density, $dE_k/d\varepsilon$, is an even more interesting quantity. It can be easily obtained quite in the same manner as for $dN/d\varepsilon$ taking the specific kinetic energy $v^2/2$ into account:

$$\frac{dE_k}{d\hat{\varepsilon}} = \frac{\varepsilon_0 N_0}{\Gamma(\alpha/2)}\hat{\varepsilon}^{\alpha/2}\exp(-\hat{\varepsilon})\,. \quad (40)$$

The peak value of Eq. (40) is attained at $\hat{\varepsilon} = \alpha/2$, which is three times higher than that of Eq. (37) for the spherical case ($\alpha = 3$).

2.2. Comparison with experiments

We apply the analytical model to two different laser experiments focusing on the ion energy spectrum. The two experimental results were separately obtained under different conditions by means of the time-of-flight method. In both cases, the laser conditions were almost the same, i.e., the wavelength $\lambda_L = 1.06\,\mu m$, the irradiation intensity $I_L = 0.5 - 1.0 \times 10^{11}\,W/cm^2$, and the pulse length τ_L~$10\,ns$ with a sufficiently large F-number of a focal lens. Moreover, the target thicknesses were R_0~$10\,\mu m$. Once the key laser parameters, I_L and τ_L, are given, the other basic parameters required for the model analysis are calculated. For example, the plasma temperature is roughly estimated from the power balance, $\eta_a I_L \approx 4\rho_{cr}c_s^3$ [15], where η_a is the absorption efficiency and ρ_{cr} is the critical mass density:

$$T_e\,[eV] = 27(A/Z)^{1/3}\hat{\lambda}_L^{4/3}\left(\eta_a \hat{I}_L\right)^{2/3}, \quad (41)$$

where A is the ion mass number. The corresponding sound speed turns out to be in the order of $10^6 cm/s$, and the disintegration time ~$2R_0/c_s$ (recall Figure 1) is calculated to be about 1 ns ($\ll \tau_L$~$10\,ns$). The normalized radius R/R_0 at the laser turn-off is obtained by Eq. (26) as a function of the normalized time $\tau_L/(R_0/c_s)$. In addition, the scale length of the plasma expansion is $c_s\tau_L$~$100\,\mu m$($\gg R_0$~$10\,\mu m$). Therefore, the present self-similar analysis is considered to be applicable to the experiments under consideration. From the above key numerical values, the characteristic ion kinetic energy at the laser turn-off defined by Eq. (38) is roughly estimated to be $\varepsilon_0 = 2.5 - 3.5$ keV.

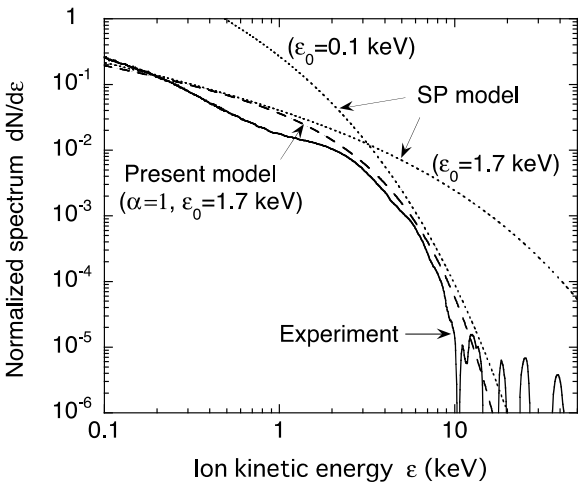

Figure 2 – Comparison of the experimental result (solid line) and the analytical curve (dashed line) obtained by Eq. (37) under planar geometry. Dotted curves for reference are obtained by the SP model, Eq. (42)

In the first case, a laser beam was irradiated on a spherical target with diameter of $500\,\mu m$, which was composed of $8\mu m$-thick plastic shell coated by a 100 nm-thick tin (Sn) layer. In this case, the plasma expansion during the laser irradiation can be regarded as quasi-planar, because the plasma scale ~$100\,\mu m$ is appreciably smaller than the laser spot size ~$500\,\mu m$. As mentioned in the introduction, the purpose of the Sn-coat was to observe the characteristics of the EUV light and energetic ion fluxes emitted from the Sn plasma. The detector was tuned to observe massive Sn ions in the direction of 30 degrees with respect to the beam axis. Figure 2 shows the ion energy spectrum comparing the experimental result (solid line) and the analytical curve (dashed line) obtained by Eq. (37) with a fitted numerical factor $\varepsilon_0 = 1.7$ keV and $\alpha = 1$ (planar

geometry). With respect to the vertical axis, the physical quantities are properly normalized such that the peak values stay in the order of unity. The fluctuated structure of the experimental data for $\varepsilon > 10$ keV cannot be clearly judged as concerns whether the signals simply span the region with less precision of diagnosis, or whether they should be attributed to other causes such as carbon ions, protons, and photons. In Figure 2, two other curves (dotted lines) are also plotted for comparison. They are obtained by the SP model [16],

$$\frac{dN}{d\hat{\varepsilon}} \propto \frac{\exp\left(-\sqrt{\hat{\varepsilon}}\right)}{\sqrt{\hat{\varepsilon}}}, \tag{42}$$

where $\varepsilon_0 = 1.7$ keV and $\varepsilon_0 = 0.1$ keV are used to draw the fitted curves to relatively low and high energy regions, respectively. It can be seen that it is hard to reproduce the experimental result by Eq. (42). The essential difference of the two analytical models is attributed to their density profiles, i.e., $\rho \propto \exp(-\xi^2)$ for the present model and $\rho \propto \exp(-\xi)$ for the SP model. This can be elaborated on as follows: The pressure scale decreases with time all over the region in the present model, while it is kept constant in time in the SP model. Therefore, the ions in the former model are less accelerated due to the pdV work than those in the latter model.

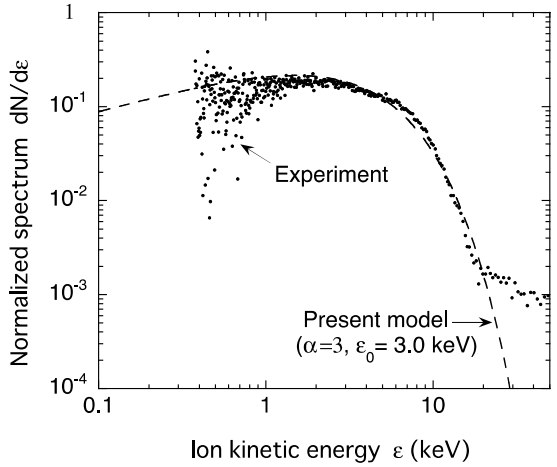

Figure 3 – Comparison of the experimental result (dots) and the analytical curve (dashed line) obtained by Eq. (37) under spherical geometry

In the second case, a laser beam was irradiated from a single side with a liquid-Xe jet ejected through a nozzle with diameter of 30 μm. The focal spot size was also 30 μm in diameter. Therefore, the resultant plasma expansion was very likely unsymmetrical. In this case, however, the specific mass can expand into much larger space three-dimensionally than in the first case, and thus is regarded as a quasi-spherical expansion ($\alpha = 3$). Figure 3 shows the experimental result and an analytical curve obtained by Eq. (37) with a fitted numerical factor $\varepsilon_0 = 3.0$ keV. Again, with respect to the vertical axis, the physical quantities are properly normalized such that the peak values stay in the order of unity. The ion fluxes were observed at an angle of 45 degrees with respect to the laser beam axis. The experimental signals strongly fluctuate at energies close to the lowest detection limit at around $\varepsilon \sim 400$ eV, but are otherwise well reproduced by the analytical curve.

3. Laser-driven nonstationary accelerating foil due to nonlinear heat conduction

When one side of a thin planar foil is heated by an external heat source, typically by laser or thermal x-ray radiation, the heated material quickly expands into vacuum with its density being reduced drastically - this phenomenon is called “ablation”. In inertial confinement fusion (ICF) research, for example, it is indispensable to correctly understand the shell acceleration due to ablation. Thereby self-similar solutions play a crucial role in the analysis and prediction of the detailed behavior of the shell acceleration. Although some analytical models have been proposed to study the shell acceleration due to mass ablation [17-19], most of them have assumed a stationary ablation layer. In Ref. [20], for example, reported a self-similar solution for the ablative heat wave. In the solution, however, the ablation surface is ideally treated such that the density goes to infinity, and the surface does not accelerate. Below, we present a new self-similar solution [6], which describes non-stationary acceleration dynamics of a planar foil target ablatively driven by non-linear heat transfer. The most striking differences from the other models are that the target has a decreasing mass with a peak density, and that it has a distinct shell/vacuum boundary, where the density and the temperature converge to null.

3.1. Basic equations and similarity ansatz

Suppose that a planar shell is being accelerated in the positive direction of the x-axis in an inertial laboratory frame via the recoil force due to the ablation. The characteristic scale length of the shell $D(t)$ decreases with time. Let us assume that the shell is burnt out at the origin of the coordinates, i.e., $D(0) = 0$ at $x = 0$. One can always find such an

inertial frame by appropriately choosing relative position and velocity to another reference inertial frame. In this case the shell velocity is initially ($t < 0$) negative, its absolute value gradually decreases due to the positive acceleration, and finally the burned-out shell halts at $(x, t) = (0,0)$. The fluid system is then described by the following equations:

$$\frac{\partial \rho}{\partial t} + \frac{\partial (\rho v)}{\partial x} = 0 \,, \tag{43}$$

$$\frac{\partial v}{\partial t} + v\frac{\partial v}{\partial x} = -\frac{\partial p}{\partial x} \,, \tag{44}$$

$$\rho\left(\frac{\partial \epsilon}{\partial t} + v\frac{\partial \epsilon}{\partial x}\right) + p\frac{\partial v}{\partial x} = \frac{\partial}{\partial x}\left(\kappa\frac{\partial T}{\partial x}\right) \,, \tag{45}$$

where ρ is the mass density, v is the flow velocity, ϵ is the specific internal energy, T is the temperature in units of energy, and κ is the thermal conductivity. We assume an ideal gas equation of state in the form,

$$p = \rho T, \ \epsilon = T/(\gamma - 1), \tag{46}$$

where γ is the specific heats ratio. We assume that the thermal conductivity is expressed in the following power-law form with m, n, and κ_0 being constants,

$$\kappa = \kappa_0 T^n/\rho^m. \tag{47}$$

We introduce the following well-known similarity ansatz [21] to eliminate the temporal dependence of the system and thus to find a self-similar solution:

$$\eta = x/D(t) \,, \ D(t) = A(-t)^\alpha \,, \ \alpha \geq 1 \,, \tag{48}$$

$$v = \alpha A(-t)^{\alpha-1} u(\eta) \,, \tag{49}$$

$$T = (\alpha A)^2 (-t)^{2(\alpha-1)} \theta(\eta) \,, \tag{50}$$

$$\rho = B(-t)^\beta g(\eta) \,, \quad \beta = \frac{2(n-1)(\alpha-1) - 1}{1+m} \,, \tag{51}$$

where η is the self-similar variable; $u(\eta)$, $\theta(\eta)$, and $g(\eta)$ stand for the self-similar profiles of the velocity, temperature, and density, respectively; α, A and B are arbitrary constants. In most of numerical calculations in this paper, we employ $\alpha = 2$ (constant acceleration), $(m, n) = (0, 5/2)$ (electron heat conductivity) and $\gamma = 5/3$ as a reference case. The constraint, $\alpha \geq 1$, in Eq. (48) stems from Eqs. (49) and (50) in order that v and T do not diverge to infinity as $t \to 0$. The limiting value, $\alpha = 1$, corresponds to a special case, where the characteristic scale of v and T are kept constant in time, while $\alpha = (2n-1)/2(n-1) = 4/3$ corresponds to another special case, where the density scale does not change in time, i.e., $\beta = 0$ [see Eq. (51)].

Using ansatz (48) - (51), Eqs. (43) - (45) are reduced to the following set of ordinary differential equations:

$$(u + \eta) g' + \left(u' - \frac{\beta}{\alpha}\right) g = 0 \,, \tag{52}$$

$$(u + \eta)\, u' + (\alpha^{-1} - 1)u + (g\theta)'/g = 0 \,, \tag{53}$$

$$(\gamma - 1)^{-1}[(u + \eta)\theta' + 2(\alpha^{-1} - 1)\theta] + \\ + \theta u' = K g^{-1}(g^{-m}\theta^n \theta')' \tag{54}$$

where the prime denotes the derivative with respect to η, and

$$K = \kappa_0 \alpha^{2n-1} A^{2n-2} B^{-1-m} \tag{55}$$

is a dimensionless parameter. Solving Eqs. (52) and (53) algebraically for g' and u', one finds that a singular point appears when $u + \eta = \pm\sqrt{\theta}$ (more details on the singular point will be given later). Let η_s, u_s, g_s, and θ_s be their values at the singular point. Here we introduce re-normalized variables, ξ, U(ξ), G(ξ), and Θ(ξ):

$$\xi = \frac{\eta - \eta_s}{\sqrt{\theta_s}} \,, \qquad \xi = \frac{u - \eta_s}{\sqrt{\theta_s}} \,, \\ G = \frac{g}{g_s} \,, \qquad \Theta = \frac{\theta}{\theta_s} \,, \tag{56}$$

At the singular point, $\xi = 0$, the re-normalized variables are specified to be

$$U(0) = -1, \quad G(0) = 1, \quad \Theta(0) = 1, \tag{57}$$

where we employ the flow direction such that $u_s + \eta_s = -\sqrt{\theta_s}$. Equations (10) - (12) are then transformed to

$$(U + \xi)\, G' + (U' - \beta/\alpha) G = 0 \,, \tag{58}$$

$$(U+\xi)U' + (\alpha^{-1}-1)U + \\ +(G\Theta)'/G + K_1 = 0\,, \tag{59}$$

$$(\gamma-1)^{-1}[(U+\xi)\Theta' + 2(\alpha^{-1}-1)\Theta] + \\ +\Theta U' = K_2 G^{-1}(G^{-m}\Theta^n\Theta')' \tag{60}$$

where the prime hereafter denotes the derivative with respect to ξ, and

$$K_1 = (1-\alpha^{-1})\eta_s/\sqrt{\theta_s}\,, \\ K_2 = K\theta_s^{n-1}g_s^{-m-1}\,, \tag{61}$$

are dimensionless constants representing the gravity (acceleration) and the heat conductivity, respectively. Thus the system is clearly defined by Eqs. (57) - (60). Equations (58) and (59) yield

$$G' = \frac{\Delta_2}{\Delta_1}G\,, \\ U' = \frac{\beta}{\alpha} - (U+\xi)\frac{\Delta_2}{\Delta_1}, \tag{62}$$

where

$$\Delta_1 = (U+\xi)^2 - \Theta\,, \tag{63}$$

$$\Delta_2 = \left(\frac{\beta}{\alpha}\right)(U+\xi) + \\ +(\alpha^{-1}-1)U + \Theta' + K_1\,. \tag{64}$$

It is clear that G′ and U′ in Eq. (62) are singular when $\Delta_1 = 0$. This singular point corresponds to the sonic point, where the flow velocity relative to the surface $\xi = const$ is equal to the local isothermal sound speed. An integrated curve which is physically acceptable is expected to pass this singular sonic point smoothly, the condition of which is given by

$$\Delta_1 = \Delta_2 = 0\,. \tag{65}$$

Since $\xi = 0$ is the singular point, one should start numerical integration at its infinitesimally adjacent point. One then needs the four derivatives $G'(0)$, $U'(0)$, $\Theta'(0)$, and $\Theta''(0)$, which are fully provided by relation (65). At $\xi = 0$, the derivatives of Eq. (62) are reduced from L'Hopital's theorem to

$$G' = \frac{\Delta_2'}{\Delta_1'}\,, \quad U' = \frac{\beta}{\alpha} + \frac{\Delta_2'}{\Delta_1'}\,. \tag{66}$$

Thus all the four derivatives at the sonic point are explicitly obtained from Eqs. (57) - (60), and (66).

The present system has another singular point at the vacuum interface, the coordinate at which, $\xi = \xi_v$, is an eigenvalue of the system. On the vacuum interface the relative flow velocity to the free surface vanishes, i.e., $U(\xi_v) + \xi_v = 0$, which can also be interpreted as the definition of the free surface. Moreover at $\xi = \xi_v$ the pressure and thus the density are expected to vanish coherently, because practically no heat conduction prevails in this front region (typically characterized such that $G \gg 1$, $\Theta \ll 1$, and $(U+\xi)^2 \ll \Theta$) and thus the specific entropy is kept constant in time. It is then shown that Eqs. (16) and (18) (neglecting the heat conduction) have the adiabatic integral with an arbitrary constant c_0 [4]:

$$\Theta(U+\xi)^\mu G^{\mu+1-\gamma} = c_0, \\ \mu \equiv \frac{2(1-\alpha)+\beta(\gamma-1)}{\alpha+\beta}. \tag{67}$$

The vacuum interface is a singular point of the adiabatic flow of the saddle type [22], where the spatial profiles in the vicinity of $\xi = \xi_v$ is worked out from Eqs. (58) - (60) to a first-order approximation in $(\xi_v - \xi)$:

$$\Theta \approx \frac{\big((\gamma+1)\alpha-2\big)(\alpha K_1 + (\alpha-1)\xi_v)}{(\alpha+\beta)\gamma} \times \\ \times (\xi_v - \xi), \tag{68}$$

$$U + \xi \approx -\frac{\gamma+1-2\alpha^{-1}}{\gamma}(\xi_v - \xi), \tag{69}$$

$$G \approx c_1(\xi_v - \xi)^\nu, \quad \nu \equiv \frac{-\alpha+\beta\gamma+2}{\alpha(\gamma+1)-2}, \tag{70}$$

where c_1 is an arbitrary constant; $c_1 \approx G_a(\xi_v - \xi_a)^{-\nu}$ for a relatively high aspect shell, i.e., $G_a/(\xi_v - \xi_a) \gg 1$, where G_a and ξ_a are their corresponding values at the density peak; G_a and ξ_a are also eigenvalues of the system as will be given below together with ξ_v. In particular, under constant acceleration ($\alpha = 2$), the velocity becomes constant, $U = -\xi_v$, and $G \propto (\xi_v - \xi_a)$ apart from a linear temperature profile in space, as one can predict from Eqs. (69) and (70).

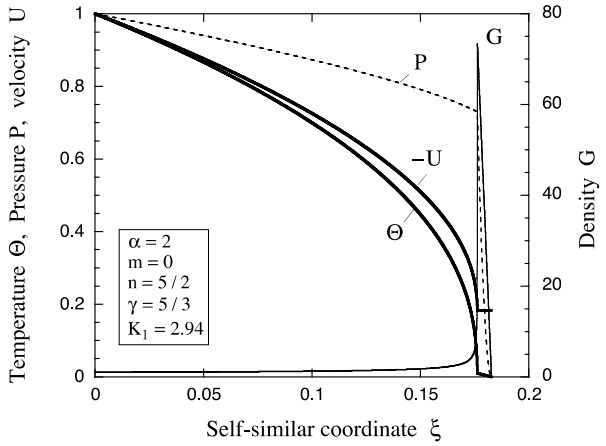

Figure 4 – Eigenstructure of the accelerated shell under a constant gravity ($\alpha = 2$)

3.2. Two dimensional eigenvalue problem and numerical results

Although one can start the numerical integration at $\xi = 0$ toward the positive direction of ξ-axis, it soon turns out that such numerical integrations produce physically unacceptable pictures under an arbitrary set of the values of K_1 and K_2 such that $G \to \infty$ on its way in the integration without showing the converging behavior, Eqs. (68) - (70), at the vacuum boundary. Therefore the present system is supposed to be an eigenvalue problem, in which only some special combinations of K_1 and K_2 can produce the converging behavior expected as a physically meaningful solution [7].

Figure 4 shows such an eigenstructure numerically obtained for the density G, the temperature Θ, the velocity U, and the pressure $P = G\Theta$ under the fixed parameters given in Figure 4. As mentioned earlier, the spatial profiles thus obtained strikingly contrast with ones for the stationary ablation models [16, 17].

Figure 5 shows the magnified view around the ablation surface of Figure 4, in which the mass flux relative to the surface with $\xi = const$, $F \equiv -(U + \xi)G$, is additionally depicted. Surprisingly the predicted profiles, (68) - (70), apply not only to the vicinity of the vacuum boundary but also to almost all the region beyond the ablation surface ($\xi > 0.1763$). This in turn supports the earlier argument that the heat conduction in the shell is practically negligible. It should also be noted that at $\xi = \xi_a$ the physical quantities seemingly have a sharp jump in their derivatives. However, all those quantities change smoothly but on a very narrow range, which can be observed in the further magnified view for G in the upper right corner in Figure 5. The characteristic scale length of the drastic change in the physical quantities can be roughly estimated from Eq. (60) to be $\Delta\xi_a \sim \Theta_a^n/|U_a|\, G_a^{1+m} \sim \mathcal{O}(10^{-5})$ as can be observed in Figure 5.

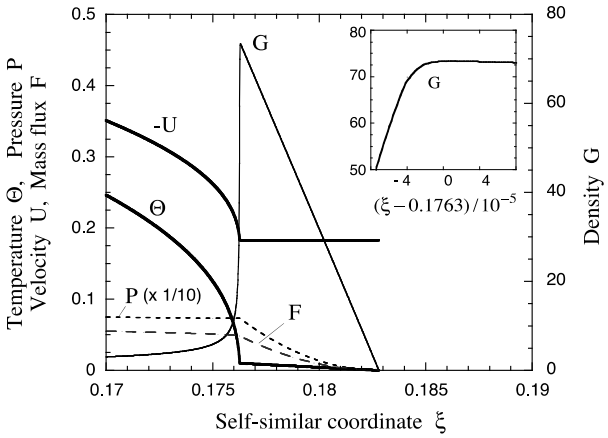

Figure 5 – Magnified view of Figure 4 around the ablation surface

4. Conclusions

The crucial role of dimensional analysis and self-similarity are discussed in the introduction and the three subsequent examples. Self-similar solutions for individual cases have been demonstrated to be derivable by applying the Lie group analysis to the set of PDE for the hydrodynamic system, taking nonlinear heat conductivity into account as the decisive physical ingredient. The scaling laws for thermally conductive fluids are conspicuously different from those for adiabatic fluids (not discussed in the present chapter; see Ref. [8] for details. The former has one freedom less than the latter due to the additional constraint of thermal conductivity. If a thermo-hydrodynamic system comprises multiple heat conduction mechanisms, self-similarity cannot be expected in a vigorous sense except for special cases. However, self-similarity and scaling laws can always be found at least in an approximate manner, by shedding light on the dominant conduction mechanism, which should give the basis of system design and diagnostics for scaled experiments for individual cases. The necessity of dimensional analysis and finding self-similar solutions is encountered in many problems over wide ranges of research. The simple general scheme and the examples mentioned in this chapter will help the reader who encounters a similar situation in his or her investigation find the underlying physics and prepare further theoretical and experimental setup.

References

1. S. Lie. Theorie der Transformationsgruppen. – New York: Chelsea, 1970. – 2043 p.
2. G.I. Barenblatt. Similarity, self-similarity, and intermediate asymptotics. – New York: Consultants Bureau, 1979. – 218 p.
3. L.I. Sedov. Similarity and dimensional methods in mechanics. – New York: Academic, 1959. – 380 p.
4. Ya.B. Zel'dovich, Yu.P. Raizer. Physics of shock waves and high temperature hydrodynamic phenomena. – New York: Academic Press, 1966. – 464 p.
5. M. Murakami, Y.-G. Kang, K. Nishihara, S. Fujioka, H. Nishimura. Ion energy spectrum of expanding laser-plasma with limited mass // Phys. Plasmas – 2005. – Vol. 12. – P. 062706.
6. M. Murakami, T. Sakaiya, J. Sanz. Self-similar ablative flow of nonstationary accelerating foil due to nonlinear heat conduction // Phys. Plasmas – 2007. – Vol. 14. – P. 022707.
7. M. Murakami, K. Nishihara, T. Hanawa. Self-similar gravitational collapse of radioactively cooling spheres // Astrophysical Journal – 2004. – Vol. 607. – P. 879.
8. M. Murakami, Sh. Iida. Scaling laws for hydrodynamically similar implosions with heat conduction // Phys. Plasmas – 2002. – Vol. 9. – P. 2745.
9. M. Murakami, M. M. Basko. Self-similar expansion of finite-size non-quasi-neutral plasmas into vacuum: Relation to the problem of ion acceleration // Phys. Plasmas – 2006. – Vol. 13. – P. 012105.
10. A.V. Gurevich, L.V. Pariiskaya, L.P. Pitaevskii. Self-similar motion of rarefied plasma // Sov. Phys. JETP – 1966. – Vol. 22. – P. 449.
11. L.D. Landau, E.M. Lifshitz. Fluid Mechanics. – New York: Pergamon, 1959. – 551 p.
12. M. Murakami, J. Meyer-Ter-Vehn, R. Ramis. Thermal x-ray emission from ion-beam-heated matter // J. X-ray Sci. Technol. – 1990. – Vol. 2. – P. 127.
13. M. A. True, J. R. Albritton, E. A. Williams. Fast ion production by suprathermal electrons in laser fusion plasmas // The Physics of Fluids – 1981. – Vol. 24. – P. 1885;
14. R. A. London, M. D. Rosen. Hydrodynamics of exploding foil x-ray lasers // Phys Fluids – 1986. – Vol. 29. – P. 3813-3822.
15. M. Murakami, J. Meyer-ter-Vehn. Indirectly driven targets for inertial confinement fusion // Nucl. Fusion – 1991. – Vol. 31. – P. 1315.
16. P. Mora. Plasma Expansion into a vacuum // Phys. Rev. Lett. – 2003. – Vol. 90. – P. 185002.
17. S. J. Gitomer, R.L. Morse, B.S. Newberger. Structure and scaling laws of laser□driven ablative implosions // Phys. Fluids – 1977. – Vol. 12. – P. 234.
18. H. Takabe, L. Montierth, R.L. Morse. Self□consistent eigenvalue analysis of Rayleigh–Taylor instability in an ablating plasma // Phys. Fluids – 1983. – Vol. 26. – P. 2299.
19. H.J. Kull. Incompressible description of Rayleigh–Taylor instabilities in laser□ablated plasmas //Phys. Fluids B – 1989. – Vol. 1. – P. 170.
20. R. Pakula, R. Sigel. Self□similar expansion of dense matter due to heat transfer by nonlinear conduction // Phys. Fluids – 1985. – Vol. 28. – P. 232.
21. G. Guderley. Starke kugelige und zylindrische verdichtungsstosse in der nahe des kugelmitterpunktes bnw. der zylinderachse // Luftfahrtforschung – 1942. – Vol. 19. – P. 302.
22. J. Sanz, J. A. Nicolás, J. R. Sanmartín, J. Hilario. Nonuniform target illumination in the deflagration regime: Thermal smoothing // Phys. Fluids – 1988. – Vol**.** 31**.** – P. 2320.

IRSTI 27.35.51

New developments in the application of the method of moments in Plasma Physics

I.M. Tkachenko

Departament of Applied Mathematics, Universitat Politècnica de València,
Camino de Vera s/n, 46022 Valencia, Spain
e-mail: imtk@mat.upv.es

This review article is based on a number of our research papers complemented by some mathematical developments which are usually not included to texts in Physics, and which can permit a reader to enter into the details of the self-consistent method of moments, recently suggested, and understand how it could be improved even further. The idea of the method of moments which appeared some 35 years ago is to employ several sum rules and other exact relations to determine the dynamic properties of strongly coupled classical or partially degenerate plasmas. Now this approach is complemented by new empirical and mathematical observations which permit to determine dynamic characteristics of strongly coupled completely ionized classical one-component plasmas without any data input from simulations or direct experiments and express the dynamic properties of the above systems entirely in terms of their static characteristics like the static structure factors. The obtained results are quite satisfactory and promising.

Key words: one-component plasmas, method of moments, dynamic structure factor.
PACS numbers: 517.958:530.1.072.11; 517.958:536.

1 Introduction

The challenge of the contemporary statistical plasma physics is the description, analytical and numerical, of the transition from collisionless to collision-dominated regimes in different Coulomb systems, of the crossover from classical to Fermi liquid behavior in dense plasmas [1, 2]. We refer to warm and hot dense matter or strongly coupled plasmas characterized by a wide range of variation of temperature ($10^4 - 10^7$ K) and mass density ($10^{-2} - 10^4$ g/cm^3) spanning a few orders of magnitude. Under such conditions thermal, Coulomb coupling, and quantum effects compete between them and impede the construction of a bridge theory capable of including of all these effects into the description of static, kinetic, and dynamic properties of the above systems of high relevance for inertial fusion devices [3] and advanced laboratory studies, e.g., in ultracold plasmas [4], etc.

The standard (electron) coupling and degeneracy parameters defined, respectively, as

$$\Gamma = \beta e^2 / a\,, \qquad D = \beta E_F\,, \tag{1}$$

vary in strongly coupled plasmas as follows:

$$\Gamma \in (4.9\times 10^{-3}, 490)\,,$$

$$D \in (1.4\times 10^{-3}, 1.4\times 10^{4})\,.$$

We employ above the Brueckner parameter

$$r_s = a / a_B \in (6.5\times 10^{-2}, 6.5)\,,$$

$a = (4\pi n/3)^{-1/3}$, a_B, and E_F are the electron Wigner-Seitz, Bohr radii and the Fermi energy, n being the number density of electrons; besides, the temperature $T = (k_B\beta)^{-1}$,

$$D = \frac{\Gamma}{2r_s}\left(\frac{9\pi}{4}\right)^{2/3} = 1.84158428\frac{\Gamma}{r_s}\,.$$

Throughout the text we will use the dimensionless wavenumber $q = ka$.

Despite the lack of small parameters, static structural and even kinetic characteristics of strongly

coupled plasmas are relatively easy to determine numerically, see, e.g., [2, 5]. Nevertheless, currently, there are no first-principle physical approaches capable of producing reliable results on dynamic properties of such systems within the above gaps between ideal-gas and solid-state conditions. Good agreement in a relatively wide realm of variation of Γ and/or D is finally achieved using up to four adjustable parameters [6]. Numerical data on the dynamic local-corrections remains unexplained theoretically [7].

The well-known model of the Quasi-Localized Charge Approximation [8] satisfies only the interaction-related sum rule and fails to describe the energy dissipation processes.

We suggest an alternative mathematical approach capable of taking all sum rules (which might be considered complementary conservation laws) into account automatically and to include into the scheme the collective mode decay. Specifics of physical systems are included into the sum rules calculated independently and rigorously using standard methods of quantum statistics, say within the Kubo linear-reaction theory. This approach seminal papers were published more than 30 years ago [9]; further development was proposed in the papers [10-13], and the book [14]. They were based on the classical monographs [15] and [16].

A new, self-consistent version of this method was suggested recently [17] applied to the direct determination of dynamic properties of one-component classical strongly coupled plasmas in terms of their static ones, without any adjustment to the dynamic data. The validity of the approach was confirmed by comparison with available simulation results. In addition, the robustness of the method was confirmed by applying several schemes of calculation of the plasma static structure factor, which provided results in good agreement with each other, within the precision of the simulations themselves.

The method of moments is based on the Nevanlinna theorem which establishes a unilateral correspondence between the dynamic characteristic in question and a non-phenomenological (Nevanlinna parameter) function of a certain mathematical class, see below. The above results were achieved in [17] and numerous relevant publications within a significant simplification: the Nevanlinna parameter function (NPF) was approximated by its static value. This simplification, in one-component plasmas, is equivalent [10] to the substitution of the dynamic local-field correction by its static value. It also impedes the extension of the approach to low coupling systems traditionally described within the random-phase approximation (RPA).

The aim of the present paper is two-fold: (i) provide a detailed introduction into the mathematical aspects of the method of moments and (ii) suggest and check some model expressions for the NPF both in classical and quantum–mechanical settings. The liquid systems we consider are presumed to be in thermal equilibrium and unmagnetized. Generalizations to more complex systems can be carried out within the matrix method of moments [14].

The paper is organized in the following way. In the next Section we provide mathematical details of the moment approach. Then, some dynamical models of the NPF are proposed and analyzed. Finally, we arrive to some conclusions important for further development of the method.

2 The mathematical introduction.

2.1 Nevanlinna (response) functions and their mathematical properties [4].

Definition 1 (*The Nevanlinna class of functions* $\mathfrak{R}$*): A function* $F(z) \in \mathfrak{R}$ *if*

1. $F(z)$ is analytic in $\mathrm{Im}\, z > 0$;
2. $\mathrm{Im}\, F(z) \geq 0$ in $\mathrm{Im}\, z > 0$.

Definition 2 *Let* $t \in \mathbb{R}$ *be a random variable with a distribution function σ(t). If*

$$\sigma(t) = \int_{-\infty}^{t} f(s)ds \qquad (2)$$

the function f(t) is called the probability density function, p.d.f.. Since σ(t) is, by definition, a non-decreasing function, f(t) ≥ 0 for any real t.

Claim 3. The Nevanlinna functions are determined by the Riesz – Herglotz transform:

$$F(z) = az + b + \int_{-\infty}^{\infty}\left(\frac{1}{t-z} - \frac{t}{1+t^2}\right)dg(t), \qquad (3)$$

where $\{a,b\} \in \mathbb{R}$ *, a ≥ 0 and g(t) is a non-decreasing bounded function (distribution) such that*

$$\int_{-\infty}^{\infty}\frac{dg(t)}{1+t^2} < \infty .$$

Claim 4 *Notice that we can always choose the function g(t) so that b was equal to*

$$b = \int_{-\infty}^{\infty} \frac{t dg(t)}{1+t^2};$$

and that

$$a = 0.$$

Definition 5 (*The class of functions* $\Re_0$*): A function* $G(z) \in \Re_0$ *if* $G(z) \in \Re$ *and*

$$\lim_{z\to\infty} \frac{G(z)}{z} = 0\,,\ \mathrm{Im}\, z > 0\,, \qquad (4)$$

so that for such functions from (3) we have:

$$G(z) = \int_{-\infty}^{\infty} \frac{dg(t)}{t-z} + ih\,,\ h > 0\,, \qquad (5)$$

where the non-negative parameter h does not depend on z, but might depend on other parameters, e.g., in Physics, on the wavenumber.

2.2 The classical Hamburger problem of moments

Definition 6 *The real numbers*

$$\mu_m = \int_{-\infty}^{\infty} t^m d\sigma(t)\,,\ m = 0,1,2,... \qquad (6)$$

are the (power) moments of the distribution σ(t). If the distribution σ(t) is differentiable and f(t) = σ'(t) is symmetric, all odd-order moments (6) vanish.

Let us summarize some notions and results of the classical theory of moments [18-20].

The Hamburger problem is formulated in the following way.

Problem 7 *Given a set of real numbers* $\{\mu_0,\mu_1,\mu_2,...\}$*, find all distributions* $\sigma(t)$ *such that*

$$\int_{-\infty}^{\infty} t^m d\sigma(t) = \mu_m\,,\ m = 0,1,2,... \qquad (7)$$

The Hamburger moment problem is solvable, i.e., there exists at least one distribution (p.d.f.) which satisfies (7), if and only if the given set of numbers $\{\mu_m\}_{m=0}^{\infty}$ *is non-negative, i.e., if the Hankel matrix* $(\mu_{m+n})_{m,n=0}^{\infty} \geq 0$*. If the problem is solvable, it can have a unique solution (a determinate problem) or an infinite number of solutions (an indeterminate problem).*

Definition 8. *Notice that if* $\sigma(t < 0) \equiv$ *const (i.e., if* $f(t < 0) \equiv 0$*), we have the Stieltjes moment problem, and if* $\sigma(t) \equiv$ *const (*$f(t) \equiv 0$*) for* $t < a$*,* $t > b$*,* $a,b \in \mathbb{R}$*, we deal with the Hausdorff problem finite interval moment problem.*

Theorem 9 *[21] A Hamburger moment problem (7) is solvable if*

$$\Delta_m = \det(\mu_{i+j})_{i,j=0}^{m} \geq 0\,,\ m = 0,1,2,...$$

The problem has an infinite number of solutions if and only if

$$\Delta_m = \det(\mu_{i+j})_{i,j=0}^{m} > 0\,,\ m = 0,1,2,...$$

The problem (7) is determinate if and only if

$$\Delta_0 > 0,...,\Delta_k > 0\,,\ \Delta_{k+1} = \Delta_{k+2} = ... = 0\,.$$

Claim 10. *The set of solutions of an indeterminate problem is in a one-to one correspondence with a certain subset of the class of Nevanlinna functions [18]; this correspondence is described by the Nevanlinna formula, see below.*

Claim 11. *A truncated Hamburger moment problem [18], i.e., a moment problem with a finite set of given numbers, i.e.,* $\{\mu_m\}_{m=0}^{2\nu}$, $\nu = 0,1,2$ *is solvable if the Hankel matrix* $(\mu_{m+n})_{m,n=0}^{\nu} > 0$*, [22], see also [23] and [24]. In the degenerate case of a singular Hankel matrix* $(\mu_{m+n})_{m,n=0}^{\nu}$ *the problem of moments (under some special conditions established in [25] and [23], [24]) has a unique solution described in [23], [24].*

Theorem 12 *[26, 21, 19] A sufficient condition that the Hamburger moment problem (6) be determinate is that (Carleman's criterion)*

$$\sum_{m=1}^{\infty} \mu_{2m}^{-1/2m} = \infty .$$

Example 13. *The p.d.f.*

$$f_\alpha(t;\gamma) = \frac{\alpha\gamma^{1/\alpha}}{2\Gamma\left(\frac{1}{\alpha}\right)} \exp\left(-\gamma|t|^\alpha\right), \alpha,\gamma > 0 \quad (8)$$

where $\Gamma(z)$ *is the Euler* Γ *function, has an infinite number of moments for any positive* α*:*

$$\mu_{2m}(\alpha;\gamma) = \int_{-\infty}^{\infty} t^{2m} f_\alpha(t)dt = \frac{\Gamma\left(\frac{2m+1}{\alpha}\right)}{\gamma^{2m/\alpha}\Gamma\left(\frac{1}{\alpha}\right)}, \quad (9)$$

$$\mu_{2m+1}(\alpha;\gamma) = 0\,, m = 0,1,2,...$$

but the Hamburger moment problem for the set of numbers

$$\left\{1, 0, \frac{\Gamma\left(\frac{3}{\alpha}\right)}{\gamma^{2/\alpha}\Gamma\left(\frac{1}{\alpha}\right)}, 0, \frac{\Gamma\left(\frac{5}{\alpha}\right)}{\gamma^{4/\alpha}\Gamma\left(\frac{1}{\alpha}\right)}, 0, ...\right\}, \quad (10)$$

has, as it stems from the Carleman criterion, a unique solution, which is the p.d.f. (8), if $\alpha > 1$*, in particular the Gaussian density* $f_2(t; \frac{1}{2a^2})$*,* $a > 0$*, and an infinite number of solutions if* $\alpha \le 1$*. In this latter case, all solutions of the moment problem are described by the Nevanlinna formula ([19]), see below.*

Other examples of sets $\{\mu_m\}_{m=0}^{\infty}$ which generate indeterminate moment problems are provided in [20].

In (solvable) problems where we already have at least one p.d.f. with a set of moments, like the problems we are interested in here, the only question which arises is the one of uniqueness of the solution of the problem of reconstruction of a (one-dimensional) p.d.f. by its power moments, $\{\mu_m\}_{m=0}^{\nu}$.

2.3 Orthogonal polynomials and the Nevanlinna formula

Theorem 14. *(Nevanlinna) There is a one-to-one correspondence between all solutions of the Hamburger problem (7), or all complex Nevanlinna functions*

$$\varphi(z) = \int_{-\infty}^{\infty} \frac{d\sigma(t)}{t-z}, \quad (11)$$

and all Nevanlinna functions $R(z) \in \mathfrak{R}_0$ *such that*

$$\varphi(z) = \int_{-\infty}^{\infty} \frac{d\sigma(t)}{t-z} = \frac{E_{n+1}(z) + R(z)E_n(z)}{D_{n+1}(z) + R(z)D_n(z)}. \quad (12)$$

This last formula is called the **Nevanlinna formula.**

Definition 15 *Here* $\{D_l(z)\}_{l=0}^{\infty}$ *are orthonormalized polynomials with respect to the measure* $d\sigma$ *[20]:*

$$\int_{-\infty}^{\infty} D_n(t)D_m(t)d\sigma(t) = \delta_{nm}\,, n,m = 0,1,..., \quad (13)$$

and $E_n(z)$ *are their conjugate polynomials:*

$$E_n(z) = \int_{-\infty}^{\infty} \frac{D_n(z) - D_n(t)}{z-t} d\sigma(t)\,. \quad (14)$$

Precisely

$$D_0(t) = \frac{1}{\sqrt{\mu_0}},\ \Delta_{-1} = 1,\ \Delta_0 = \mu_0\,,$$

$$D_l(t) = \frac{1}{\sqrt{\Delta_l\Delta_{l-1}}} \det\begin{bmatrix} \mu_0 & \cdots & \mu_{l-1} & 1 \\ \mu_1 & \cdots & \mu_l & t \\ \vdots & \vdots & \vdots & \vdots \\ \mu_l & \cdots & \mu_{2l-1} & t^l \end{bmatrix}, \quad (15)$$

$$\Delta_l = \det\begin{bmatrix} \mu_0 & \cdots & \mu_l \\ \vdots & \vdots & \vdots \\ \mu_l & \cdots & \mu_{2l} \end{bmatrix}, l = 1,2,... \quad (16)$$

Let us point out the properties of these orthonormalized polynomials:

Claim 16. *It can be easily seen that both sets of polynomials do not depend on the distribution we seek, they are determined by the moments only:*

$$D_0(z)=\frac{1}{\sqrt{\mu_0}},\ D_1(z)=\frac{1}{\sqrt{\mu_0}}\frac{z-a_0}{b_0},$$

$$D_2(z)=$$

$$=\frac{\left(\mu_0\mu_2-\mu_1^2\right)z^2+z\left(\mu_1\mu_2-\mu_3\mu_0\right)+\left(\mu_3\mu_1-\mu_2^2\right)}{\sqrt{\left(\mu_0\mu_2-\mu_1^2\right)\Delta_2}},$$

$$E_0(z)=0,\ E_1(z)=\frac{\sqrt{\mu_0}}{b_0},$$

$$E_2(z)=$$

$$=\frac{\mu_0\left(\mu_0\mu_2-\mu_1^2\right)z+\left(\mu_0\mu_2-\mu_1^2\right)\mu_1+\mu_0\left(\mu_1\mu_2-\mu_0\mu_3\right)}{\sqrt{\left(\mu_0\mu_2-\mu_1^2\right)\Delta_2}} \tag{17}$$

In addition:

1. The zeros of the polynomials $D_l(t)$ and $E_l(t)$, $l\in\mathbb{N}$, are all real;
2. The zeros of the polynomials $D_l(t)$ and $D_{l-1}(t)$, $l\in\mathbb{N}$, are all real and they alternate. The zeros of the polynomials $D_l(t)$ and $E_l(t)$, $l\in\mathbb{N}$, alternate;
3. The polynomials $D_l(t)$ and $E_l(t)$, $l\in\mathbb{N}$, can be expressed in terms of each other:

$$zD_l(z)=b_{l-1}D_{l-1}(z)+a_lD_l(z)+b_lD_{l+1}(z),\quad l=1,2,... \tag{18}$$

$$zE_l(z)=b_{l-1}E_{l-1}(z)+a_lE_l(z)+b_lE_{l+1}(z),\quad l=1,2,... \tag{19}$$

where

$$a_l=a_{l,l}=\int_{-\infty}^{\infty}tD_l(t)D_l(t)d\sigma(t),$$

$$b_l=a_{l,l+1}=\int_{-\infty}^{\infty}tD_l(t)D_{l+1}(t)d\sigma(t)=\frac{\sqrt{\Delta_{l-1}\Delta_{l+1}}}{\Delta_l},\quad l=1,2,...$$

4. They satisfy the Liouville-Ostrogradsky (or Schwarz-Christoffel) formula:

$$D_{l-1}(z)E_l(z)-D_l(z)E_{l-1}(z)=\frac{1}{b_{l-1}}=\frac{\Delta_{l-1}}{\sqrt{\Delta_{l-2}\Delta_l}},\quad l=2,3,... \tag{20}$$

Claim 17. *The latter relation permits to define these polynomials in the recurrent way. Indeed, since*

$$D_0(z)=\frac{1}{\sqrt{\mu_0}},\ D_1(z)=\frac{1}{\sqrt{\mu_0}}\frac{z-a_0}{b_0},$$

$$E_0(z)=0,\ E_1(z)=\frac{\sqrt{\mu_0}}{b_0},$$

we have that

$$D_2(z)=$$

$$=\frac{\left(\mu_0\mu_2-\mu_1^2\right)z^2+z\left(\mu_1\mu_2-\mu_3\mu_0\right)+\left(\mu_3\mu_1-\mu_2^2\right)}{\sqrt{\left(\mu_0\mu_2-\mu_1^2\right)\Delta_2}},$$

$$E_2(z)=$$

$$=\frac{\mu_0\left(\mu_0\mu_2-\mu_1^2\right)z+\left(\mu_0\mu_2-\mu_1^2\right)\mu_1+\mu_0\left(\mu_1\mu_2-\mu_0\mu_3\right)}{\sqrt{\left(\mu_0\mu_2-\mu_1^2\right)\Delta_2}}$$

and so on. This procedure can be easily programmed.

Claim 18. *It can be easily checked that the polynomials $D_\ell(z)$, ℓ = 0,1,2 are all normalized to unity and mutually orthogonal.*

Claim 19. *The set of orthogonal (but not normalized) polynomials $\{D_\ell(t)\}_{\ell=0}^{\infty}$ can be constructed from the canonical basis of the Hilbert vector space of polynomials,*

$$\left\{1,t,t^2,...\right\},$$

but with the scalar product and the norm defined as

$$\langle f, g\rangle = \int_{-\infty}^{\infty} f(t)\overline{g(t)}d\sigma(t),\ \|f\| = \sqrt{\langle f, f\rangle},$$

by means of the standard Gram-Schmidt procedure. Then,

$$D_0(t) = 1, D_1(t) = t - \frac{\mu_1}{\mu_0},$$

$$D_2(t) = t^2 - t\frac{\mu_1\mu_2 - \mu_0\mu_3}{\mu_1^2 - \mu_0\mu_2} + \frac{\mu_2^2 - \mu_3\mu_1}{\mu_1^2 - \mu_0\mu_2},$$

$$D_3(t) = t(t^2 + At + B),$$

$$E_0(t) = 0, E_1(t) = \mu_0 \qquad (21)$$

$$E_2(t) = \mu_0\left(t - \frac{\mu_1\mu_2 - \mu_0\mu_3}{\mu_1^2 - \mu_0\mu_2}\right) + \mu_1,$$

$$E_3(t) =$$

$$= \mu_0\left(t^2 + t\left(A + \frac{\mu_1}{\mu_0}\right) + \left(\frac{\mu_2}{\mu_0} + A\frac{\mu_1}{\mu_0} + B\right)\right)$$

where

$$A =$$

$$= \frac{\mu_1\left(\mu_3^2 + \mu_2\mu_4\right) - \mu_3\left(\mu_2^2 + \mu_0\mu_4\right) - \mu_5\left(\mu_1^2 - \mu_0\mu_2\right)}{\mu_2\left(\mu_2^2 - \mu_0\mu_4\right) + \mu_3\left(\mu_0\mu_3 - \mu_1\mu_2\right) + \mu_1\left(\mu_4\mu_1 - \mu_2\mu_3\right)}$$

$$B =$$

$$= \frac{\mu_5\left(\mu_1\mu_2 - \mu_0\mu_3\right) - \mu_3\left(\mu_1\mu_4 - \mu_2\mu_3\right) - \mu_4\left(\mu_2^2 - \mu_0\mu_4\right)}{\mu_2\left(\mu_2^2 - \mu_0\mu_4\right) + \mu_3\left(\mu_0\mu_3 - \mu_1\mu_2\right) + \mu_1\left(\mu_4\mu_1 - \mu_2\mu_3\right)}$$

An important observation can be deduced from the expressions (15) and (21): both sets of orthogonal polynomials do not depend on the distribution we seek, they are determined by the moments only. In other words, these polynomials are known as soon as the moments are.

2.4 Canonical and degenerate solutions of a solvable truncated Hamburger moment problem

Claim 20. *It is clear that, at least, due to numerical and measurement problems, we never know a large number of moments. Besides, as we will see, in certain physically important problems, this number is limited by physical phenomena.*

To satisfy the moment conditions

$$\mu_m = \int_{-\infty}^{\infty} t^m d\sigma(t) = \int_{-\infty}^{\infty} t^m f(t)dt, \qquad (22)$$
$$m = 0,1,2,...,2\nu, \nu = 0,1,2,...,$$

one can first consider a step-like distribution

$$d\sigma(t) = \sum_{j=0}^{2\nu} m_j \delta(t - t_j)dt \qquad (23)$$

with the density which actually consists of $2\nu + 1$ point masses located at some distinct points of the real axis $\{t_j\}_{j=0}^{2\nu}$. This is the so called *canonical solution* of the problem. Then the assumption (23) can be substituted into the conditions (22) and the masses $\{m_j\}_{j=0}^{2\nu}$ can be obtained directly from the system with the determinant which is the Van der Monde determinant of an arbitrary set of distinct numbers $\{t_j\}_{j=0}^{2\nu}$:

$$\begin{bmatrix} 1 & 1 & \cdots & 1 \\ t_0 & t_1 & \cdots & t_{2\nu} \\ \vdots & \vdots & \ddots & \vdots \\ t_0^{2\nu} & t_1^{2\nu} & \cdots & t_{2\nu}^{2\nu} \end{bmatrix}\begin{bmatrix} m_0 \\ m_1 \\ \vdots \\ m_{2\nu} \end{bmatrix} = \begin{bmatrix} \mu_0 \\ \mu_1 \\ \vdots \\ \mu_{2\nu} \end{bmatrix} \qquad (24)$$

In other words, we obtain an infinite number of canonical solutions parametrized by the latter set of points of the real axis.

Example 21. Gaussian distribution *exp(−t²). Consider a truncated problem generated by the moments*

$$\mu_m = \int_{-\infty}^{\infty} t^m \exp\left(-t^2\right)dt,\ m = 0,1,2,...,2\nu,$$

$$\mu_0 = \sqrt{\pi}, \mu_1 = 0, \mu_2 = \frac{\sqrt{\pi}}{2}.$$

Then the system (24) becomes:

$$\begin{bmatrix} 1 & 1 & 1 \\ t_0 & t_1 & t_2 \\ t_0^2 & t_1^2 & t_2^2 \end{bmatrix} \begin{bmatrix} m_0 \\ m_1 \\ m_2 \end{bmatrix} = \begin{bmatrix} \sqrt{\pi} \\ 0 \\ \sqrt{\pi}/2 \end{bmatrix}$$

Its solution is just:

$$\begin{pmatrix} m_0 \\ m_1 \\ m_2 \end{pmatrix} = \frac{\sqrt{\pi}}{2} \begin{pmatrix} \dfrac{(2x_1x_2+1)}{(x_2-x_0)(x_1-x_0)} \\ \dfrac{(2x_0x_2+1)}{(x_2-x_1)(x_0-x_1)} \\ \dfrac{(2x_0x_1+1)}{(x_1-x_2)(x_0-x_2)} \end{pmatrix}.$$

Claim 22. *Nevertheless, for the moment set* $\{\mu_0,0,\mu_2\}$*, there exists the following canonical solution of the moment problem where*

$$\int_{-\infty}^{\infty} t^m f(t)\,dt = \mu_m,\ m = 0,1,2,$$

$$f(t) = \frac{\mu_0}{2}\left[\delta(t-\xi) + \delta(t+\xi)\right],\ \ \xi^2 = \frac{\mu_2}{\mu_0}$$

Claim 23. *While, for the moment set* $\{\mu_0,0,\mu_2,0,\mu_4\}$*, there exists the following canonical solution of the moment problem*

$$\int_{-\infty}^{\infty} t^m f(t)\,dt = \mu_m,\ m = 0,1,2,3,4:,$$

$$f(t) =$$

$$= \mu_0 \left\{ \left(1 - \frac{\xi_1^2}{\xi_2^2}\right)\delta(t) + \frac{\xi_1^2}{2\xi_2^2}\left[\delta(t-\xi_2) + \delta(t+\xi_2)\right] \right\}$$

where

$$\xi_1^2 = \frac{\mu_2}{\mu_0},\ \ \xi_2^2 = \frac{\mu_4}{\mu_2}$$

This solution will be interpreted later, e.g., in Chapter 3.2 dedicated to the investigation of one-component plasmas. The positivity of the central feature intensity, $(1 - (\xi_1/\xi_2)^2)$ *follows from the Cauchy-Schwarz inequality.*

Example 24. ***Degenerate case.*** *Consider now a degenerate truncated problem generated by the moments*

$$\mu_0 = 1,\ \mu_1 = \sqrt{2},\ \mu_2 = 2 \qquad (25)$$

whose Hankel matrix

$$H_1 = \begin{bmatrix} 1 & \sqrt{2} \\ \sqrt{2} & 2 \end{bmatrix},$$

is obviously singular ($\det H_1 = 0$*). In this case the solution of the problem is unique, it can be found in the following way. Find the null-space basis of the matrix* H_1*, in our case it is a vector* $\begin{bmatrix} -\sqrt{2} \\ 1 \end{bmatrix} := \begin{bmatrix} \xi_0 \\ \xi_1 \end{bmatrix}$ *with* $\xi_1 \neq 0$*, construct the polynomial*

$$p(t) = \xi_1 t + \xi_0,$$

calculate its zeros (in our case we have only one zero $t_0 = \sqrt{2}$*), these are the locations* $\{t_i\}_{i=1}^{\nu}$ *of the masses in the degenerate solution*

$$d\sigma(t) = \sum_{i=0}^{2\nu} m_j \delta(t - t_i)dt$$

and determine the corresponding masses from the moment conditions (22). Particularly, for the moments (25) we have

$$d\sigma(t) = \delta\left(t - \sqrt{2}\right)dt$$

which automatically satisfies the conditions

$$\mu_0 = 1, \mu_1 = \sqrt{2}, \mu_2 = 2$$

Claim 25. *Certainly, in physical problems we are basically interested in noncanonical, continuous solutions Nevertheless, some physical interpretation*

of the canonical solutions will be discussed as well. To show how the moment method works in this case, let us consider dynamic properties of the intrinsically classical one – and two – component completely ionized hydrogen – like plasmas in thermal equilibrium.

2.5. Non-canonical solutions of a truncated Hamburger problem. Application of the Nevanlinna formula

In physical problems we deal with further, we are interested in continuous solutions of truncated Hamburger problems generated by **positive** sets of power moments

$$\{\mu_0, \mu_1, \mu_2, ..., \mu_{2\nu-1}, \mu_{2\nu}\}, \ \nu = 0,1,2,...,$$

basically, with $\nu = 2$ and with the so called immaterial elements $\mu_{2\nu+1}$ and $\mu_{2\nu+2}$. Let us see how the Nevanlinna formula in this case provides a continuous, non-canonical, solution of the problem: construct the p.d.f. $f(t)$ such that

$$\mu_l = \int_{-\infty}^{\infty} t^l f(t)dt, \ l = 0,1,2,...,2\nu, \quad \nu = 0,1,2,... \tag{26}$$

The Nevanlinna formula in this case takes the following form:

$$\varphi(z) = \int_{-\infty}^{\infty} \frac{f(t)}{t-z}dt = -\frac{E_{\nu+1}(z) + R_\nu(z)E_\nu(z)}{D_{\nu+1}(z) + R_\nu(z)D_\nu(z)}, \tag{27}$$

Claim 26. *Observe that the Nevanlinna parameter function $Q_\nu(z) \in \mathfrak{R}_0$ effectively depends on the number of moments involved. Nevertheless, the asymptotic expansion of the Cauchy transform of the density in question will satisfy the moment conditions (26) independently of our choice of this parameter function.*

Proof. Indeed, along any ray within the upper half-plane $Imz > 0$,

$$\varphi(z \to \infty) = -\frac{1}{z}\int_{-\infty}^{\infty} \frac{f(x)}{1-\frac{x}{z}}dx \underset{z\to\infty}{\square} -\frac{1}{z}\int_{-\infty}^{\infty} f(x)\left(\sum_{l=0}^{2\nu}\left(\frac{x}{z}\right)^l + O\left(\frac{1}{z}\right)^{2\nu+1}\right)dx = \tag{28}$$
$$= -\sum_{l=0}^{2\nu}\frac{1}{z^{l+1}}\int_{-\infty}^{\infty} x^l f(x)dx + O\left(\frac{1}{z}\right)^{2\nu+2} = -\sum_{l=0}^{2\nu}\frac{\mu_l}{z^{l+1}} + O\left(\frac{1}{z}\right)^{2\nu+2}$$

In other words, the contribution related to the Nevanlinna parameter function $Q_\nu(z)$, due to the additional property (4), will appear in the asymptotic expansion (28) only in the correction of excessive order $2\nu + 2$. Now, by definition, on the real axis $Imz = 0$,

$$\varphi(t) = \mathrm{Im}\left(\lim_{\eta\downarrow 0}\int_{-\infty}^{\infty}\frac{f(s)ds}{s-t-i\eta}\right) = \mathrm{Im}\left(P.V.\int_{-\infty}^{\infty}\frac{f(s)ds}{s-t} + \pi i f(t)\right) = ,$$
$$= \pi f(t) = -\mathrm{Im}\frac{E_{\nu+1}(t) + R_\nu(t)E_\nu(t)}{D_{\nu+1}(t) + R_\nu(t)D_\nu(t)}$$

P.V standing for the principal value of the integral. Let

$$R(t) = \mathrm{Re}\,R(t) + i\,\mathrm{Im}\,R(t),$$
$$\overline{R(t)} = \mathrm{Re}\,R(t) - i\,\mathrm{Im}\,R(t)$$

and observe that, also by definitions (15) and (16), we have:

$$D_{\nu+1}(t)=\frac{1}{\sqrt{\Delta_{\nu+1}\Delta_{\nu}}}\det\begin{bmatrix}\mu_0 & \cdots & \mu_{\nu-1} & \mu_{\nu} & 1\\ \mu_1 & \cdots & \mu_{\nu} & \mu_{\nu+1} & t\\ \vdots & \cdots & \vdots & \vdots & \vdots\\ \mu_{\nu-1} & \cdots & \mu_{2\nu-1} & \mu_{2\nu} & t^{\nu}\\ \mu_{\nu} & \cdots & \mu_{2\nu} & \mu_{2\nu+1} & t^{\nu+1}\end{bmatrix}$$

so that the algebraic minor, (subdeterminant) of the $D_{\nu+1}(t)$ polynomial leading term is just the Hankel determinant

$$\Delta_{\nu}=\det\begin{bmatrix}\mu_0 & \cdots & \mu_{\nu-1} & \mu_{\nu}\\ \mu_1 & \cdots & \mu_{\nu} & \mu_{\nu+1}\\ \vdots & \vdots & \vdots & \vdots\\ \mu_{\nu-1} & \cdots & \mu_{2\nu-1} & \mu_{2\nu}\end{bmatrix}, \qquad (29)$$

Hence,

$$P_{\nu+1}(t)=\sqrt{\frac{\Delta_{\nu}}{\Delta_{\nu+1}}}P_{\nu+1}(t),$$
$$P_{\nu}(t)=\sqrt{\frac{\Delta_{\nu-1}}{\Delta_{\nu}}}P_{\nu}(t) \qquad (30)$$

where $\{P_l(t)\}_{l=0}^{\nu+1}$ are orthogonal monic polynomials with respect to the measure density $f(t)$, see the Claim 19. Thus 1, due to the Liouville-Ostrogradsky equality (20), the "problem" is that the determinant $\Delta_{\nu+1}$ (see (29)) contains the "immaterial" moments $\mu_{2\nu+1}$ and $\mu_{2\nu+2}$, which we do not know. They might even diverge! This spurious contradiction is immediately resolved by taking into account the normalization of the orthonormalized polynomials $\{P_l(t)\}_{l=0}^{\nu+1}$: use instead the monic polynomials $\{P_l(t)\}_{l=0}^{2\nu}$:

$$f(t)=\frac{\Delta_{\nu}}{\pi\sqrt{\Delta_{\nu-1}\Delta_{\nu+1}}}\frac{\operatorname{Im}R_{\nu}(t)}{\left|P_{\nu+1}(t)+R_{\nu}(t)P_{\nu}(t)\right|^2}=$$
$$=\frac{\Delta_{\nu}}{\pi\sqrt{\Delta_{\nu-1}\Delta_{\nu+1}}}\frac{\operatorname{Im}R_{\nu}(t)}{\left|\sqrt{\frac{\Delta_{\nu}}{\Delta_{\nu+1}}}P_{\nu+1}(t)+R_{\nu}(t)\sqrt{\frac{\Delta_{\nu-1}}{\Delta_{\nu}}}P_{\nu}(t)\right|^2}= \qquad (31)$$
$$=\frac{\Delta_{\nu}}{\pi\Delta_{\nu-1}}\frac{\operatorname{Im}Q_{\nu}(t)}{\left|P_{\nu+1}(t)+Q_{\nu}(t)P_{\nu}(t)\right|^2}>0$$

where

$$Q_{\nu}(t)=R_{\nu}(t)\frac{\sqrt{\Delta_{\nu-1}\Delta_{\nu+1}}}{\Delta_{\nu}}$$

Notice that due to the positivity of the moment sequence (26), the Hankel determinants $\Delta_{\nu-1}$ and Δ_{ν} are all strictly positive.

Thus, the immaterial members of the moment sequence are eliminated due to the renormalization procedure. What matters for the physical applications is that the poles of the reconstructed density $f(z)$, $Imz < 0$ are the roots of the "polynomial" equation

$$P_{\nu+1}(z)+Q_{\nu}(z)P_{\nu}(z)=0 \qquad (32)$$

which "starts" from $z^{\nu+1}$, i.e., if, in accordance with the $\Re_0$-version of the Riesz-Herglotz formula (5), we approximate the Nevanlinna parameter function (NPF) $q_{\nu}(z)$ by its static value:

$$Q_{\nu}(z)=Q_{\nu}(z=0)=ih \qquad (33)$$

equation (32) acquires the form of the genuine polynomial equation of the order $\nu+1$, which can be easily solved at least numerically. Nevertheless, our aim here is to study the possibilities of employment of frequency-dependent NPFs.

3 Solution of physical problems by the method of moments.

Here we will study the dynamic properties of dense one – and two-component plasmas in the context of the truncated Hamburger problem. We

[1] Remember that for any $z \in C$, *Imz=(z-z*)/2i, where z* is the complex conjugate of z.*

start with the calculation of power moments on the basis of the Kramers-Kronig relations and the Kubo linear theory.

3.1 The moments.

The physical characteristics of the system interfere, within the method of moments, basically through the sum rules. If we presume the existence of the Coulomb or Coulomb-like system inverse (longitudinal) dielectric function, $\varepsilon^{-1}(k,\omega)$ (IDF), the sum rules are effectively the power frequency moments of the (positive) even loss function $L(k,\omega) = -\mathrm{Im}\,\varepsilon^{-1}(k,\omega)/\omega$:

$$C_\nu(k) = \frac{1}{\pi}\int_{-\infty}^{\infty} \omega^\nu L(k,\omega)d\omega, \quad \nu = 0,2,4. \tag{34}$$

Notice that the odd order moments vanish due to the symmetry of the loss function. Let us also introduce the characteristic frequencies

$$\omega_1^2(k) = \frac{C_2(k)}{C_0(k)}, \quad \omega_2^2(k) = \frac{C_4(k)}{C_2(k)} \tag{35}$$

In a classical plasma, due to the fluctuation-dissipation theorem (FDT), the dynamic structure factor (charge density-charge density)

$$S(q,\omega) = \frac{q^2 n_e}{3\pi\Gamma} B(\beta\hbar\omega)L(q,\omega), \tag{36}$$

where

$$B(w) = w(1-\exp(-w))^{-1} \underset{w\to 0}{\cong} 1 \tag{37}$$

is the Bose factor. Both dynamic functions, $L(q,\omega)$ and $S(q,\omega)$, behave at low frequencies and/or in classical systems in a similar way. Hence, the moments $\{C_0(q),0,C_2,0,C_4(q)\}$ are effectively proportional to the moments of the dynamic structure factor (DSF).

Since the IDF is a genuine response function [27] and thus satisfies, by virtue of the causality principle, the Kramers-Kronig relations,

$$\varepsilon^{-1}(k,z) = 1 + \frac{1}{\pi}\int_{-\infty}^{\infty} \frac{\mathrm{Im}\,\varepsilon^{-1}(k,\omega)}{\omega - z}d\omega, \quad \mathrm{Im}\,z > 0, \tag{38}$$

and since the imaginary part $\mathrm{Im}\epsilon^{-1}(q,\omega)$ is an odd function of frequency and thus vanishes at $\omega = 0$, we can write:

$$\varepsilon^{-1}(k,0) = 1 + \frac{1}{\pi}\int_{-\infty}^{\infty} \frac{\mathrm{Im}\,\varepsilon^{-1}(k,\omega)}{\omega}d\omega = 1 - C_0(q) \tag{39}$$

We conclude that

$$C_0(k) = 1 - \varepsilon^{-1}(k,0)$$

The above relations permit to study the asymptotic expansion of the IDF along any ray in the upper half-plane:

$$\varepsilon^{-1}(q,z) - \varepsilon^{-1}(q,0) = \frac{1}{\pi}\int_{-\infty}^{\infty} \frac{L(q,\omega)d\omega}{1-\frac{\omega}{z}} \underset{z\to\infty}{\cong}$$

$$\underset{z\to\infty}{\cong} \frac{1}{\pi}\int_{-\infty}^{\infty}\left(1 + \frac{\omega}{z} + \left(\frac{\omega}{z}\right)^2 + \left(\frac{\omega}{z}\right)^3 + \left(\frac{\omega}{z}\right)^4 + \ldots\right)L(q,\omega)d\omega = \tag{40}$$

$$= C_0(q) + \frac{C_2}{z^2} + \frac{C_4(q)}{z^4} + \ldots$$

Thus,

$$\varepsilon^{-1}(q, z\to\infty) \cong 1.$$

Similarly, for the dielectric function itself, inverting the last formula,

$$\varepsilon^{-1}(q,z) \underset{z\to\infty}{\cong} 1 - \frac{\omega_p^2}{z^2} - \frac{\omega_p^2\left(\omega_2^2(q) - \omega_p^2\right)}{z^4} + \ldots \tag{41}$$

It stems directly from the *f*-sum rule [27] that even if the interparticle interaction might be different from the bare Coulomb one and is described by an effective potential [15],

$$C_2 = \frac{1}{\pi}\int_{-\infty}^{\infty} \omega^2 L(k,\omega)d\omega \equiv \omega_p^2 \qquad (42)$$

where ω_p is the system plasma frequency.

It has been established [28,29] and further, within the Kubo linear-reaction theory and using the second-quantization technique [14], generalized for a multicomponent Coulomb system with the pairwise interaction energy Fourier transform,

$$W_{ab}(q) = \frac{4\pi e^2 a}{q^2}\zeta_{ab}(q), \quad \zeta_{ab}(q) = \zeta_{ba}(q), \quad a,b = e,i_1,i_2,..., \qquad (43)$$

that the fourth moment and, hence, the second characteristic frequency contains four contributions:

$$\omega_2^2(q) = \omega_p^2\left[\zeta_{ee}(q) + K(q) + U(q) + H\right], \qquad (44)$$

The kinetic contribution

$$K(q) = \frac{q^2}{\Gamma}\frac{F_{3/2}(\eta)}{D^{3/2}} + \frac{q^4}{12r_s} \qquad (45)$$

and the coupling contributions are:

$$U(q) = \frac{1}{12\pi}\int_0^{\infty} p^2(S_{ee}(p)-1)\left(Z_{ee}(p,q) - \frac{8\zeta_{ee}(p)}{3}\right)dp,$$

$$H = \frac{2\sqrt{Z}}{9\pi}\int_0^{\infty} p^2 S_{ei}(p)\zeta_{ei}(p)dp, \qquad (46)$$

$$Z_{ee}(p,q) = \int_{|p-q|}^{p+q} \zeta_{ee}(s)\left(p^2 - q^2 - s^2\right)^2 \frac{ds}{pq^3 s}$$

Here,

$$F_\mu(\eta) = \int_0^{\infty} \frac{t^\mu}{\exp(t-\eta)+1}dt$$

is the order-μ Fermi integral, and η is the dimensionless chemical potential of the electronic subsystem, which should be determined by the normalization condition

$$F_{1/2}(\eta) = \frac{2}{3}D^{3/2}.$$

Notice that the e–i contribution is q-independent. Terms of the order of the ratio m/M were neglected to obtain these simple expressions. To reiterate that we are able to evaluate the moments independently with a precision determined by the numerical scheme employed to compute the partial static structure factors, see the paper [17] for details. Notice also that in the hydrodynamic limiting case

$$\omega_2^2(q \to 0) \cong \omega_p^2\left(1 + H\right) \qquad (47)$$

while at short distances we recover the single-particle behavior:

$$\omega_2^2(q \to \infty) \cong \frac{\omega_p^2 q^4}{12r_s} \qquad (48)$$

It is obvious that in one-component plasmas, classical or not, the electron-ion contribution $H = 0$. In the same way, higher order moments can be calculated, e.g. in model Coulomb systems with the effective potential (43) different from the bare Coulomb one. But in purely Coulomb systems containing species of different masses, the sixth and higher-order moments diverge [30]. This takes place because the corresponding explicit expressions contain uncompensated contributions like

$$\sum_q \left\langle n_q^a n_{-q}^a \right\rangle = \infty$$

The divergence of higher-order moments $C_{2l}(k)$ with $l > 2$ is directly related to the slow decay of the loss function as $|\omega| \to \infty$. If we presume that for

$$L(k,|\omega| \to \infty) \cong A(k) / |\omega|^\gamma$$

then, due to the divergence of the sixth moment and the convergence of the fourth one (44), we conclude that $5 < \gamma \leq 7$.

In a completely ionized plasma for $\omega >> (\beta\hbar)^{-1}$ the microscopic acts of the electromagnetic field energy absorption become the processes inverse with respect to the bremsstrahlung during pair collisions of charged particles. As it was shown by L. Ginzburg ([31]) this circumstance permits to use the detailed equilibrium principle to express the imaginary part of the longitudinal dielectric function, $\mathrm{Im}\epsilon(k,\omega)$, of a completely ionized plasma, which is directly related to the plasma external dynamic conductivity $\sigma^{ext}(k,\omega)$ real part, in terms of the bremsstrahlung cross-section. A calculation similar to that of Ginzburg, but using the well-known expression for the bremsstrahlung differential cross-section for high values of energy transfer and $\omega \gg (\beta\hbar)^{-1}$ [32], lead to the following asymptotic form of $Im\epsilon(k,\omega)$ in a completely ionized (for simplicity, hydrogen-like) plasma [30]:

$$\mathrm{Im}\,\varepsilon\left(k,\omega >> \left(\beta\hbar\right)^{-1}\right) \cong \cong \frac{4\pi A_0}{\omega^{9/2}}\left(1-\frac{\omega_T}{\omega}+\ldots\right), \quad (49)$$

where

$$A_0 = \frac{2^{5/2}\pi}{3} n_e n_i \frac{Z^2 e^6}{\left(\hbar m\right)^{3/2}}, \quad \omega_T = \frac{3}{4\beta\hbar},$$

$n_i = Zn_e$. The main term of (49) was obtained by Perel' and Eliashberg [33]. One of our aims is to specify (49) taking into account the sum rules (34). Notice that even the main term of the plasma dielectric function asymptotic behavior (49) is still discussed in literature, producing sometimes even contradictory results [34].

3.2 Classical one-component plasmas.

The classical one-component plasma (OCP) might be considered a test-tube for the modelling of strongly interacting Coulomb systems [35], see also [36] and [37] for more recent reviews. OCP is often employed as a simplified version of real physical systems ranging from electrolytes and charged-stabilized colloids [38], laser-cooled ions in cryogenic traps [39] to dense astrophysical matter in white dwarfs and neutron stars [40]. Another modern and highly interesting pattern of the OCP is dusty plasmas with the pure Coulomb interparticle interaction potential substituted by the Yukawa effective potential [41].

The classical OCP is defined as a system of charged particles (ions) immersed in a uniform background of opposite charge. It is characterized by a unique dimensionless coupling parameter $\Gamma = \beta(Ze)^2/a$. Here, like before, β^{-1} stands for the temperature in energy units, Ze designates the ion charge, and $a = (3/4\pi n)^{1/3}$ is the Wigner-Seitz radius, n being the number density of charged particles. For $\Gamma > 1$ the interaction effects determine the physical properties of the OCP.

We successfully applied the method of moments complemented by some physical considerations in [17]. Precisely, the five-moment approximation $\{C_0(q), 0, C_2, 0, C_4(q)\}$ was applied to reconstruct the dynamic structure factor (36) and to study the properties of the collective modes in Coulomb and Yukawa model systems characterized by the diagonal form-factors in (43) equal to, respectively, $\zeta_C = 1$ and $\zeta_Y = q^2/(q^2+\kappa^2)$, where κ is the screening parameter of the Yukawa potential $(Z^2e^2/r)\exp(-\kappa r/a)$. With the simplification (33) and the symmetry of the loss function taken into account, the expression for the DSF can be written as

$$\frac{\pi S(q,\omega)}{nS(q)} = \frac{\omega_1^2(\omega_2^2-\omega_1^2)h}{\omega^2(\omega^2-\omega_2^2)^2+h^2(\omega^2-\omega_1^2)^2}, \quad (50)$$

Since the loss function, and in a classical system, the DSF are even function of frequency, the r.h.s. of the previous expression depends only on the frequency squared. It implies that the first derivative of the DSF at $\omega^2 = 0$ vanishes only if

$$h = h_0(q) = \frac{\omega_2^2(q)}{\omega_1(q)\sqrt{2}}a, \quad (51)$$

The presence of an extremum of the loss function and, in classical systems, of the DSF at $\omega = 0$ follows from the canonical solution (23) with the point masses located at the points $\omega = 0$, $\omega = \omega_1$, and $\omega = \omega_2$ [42]:

$$\frac{S_{\mathrm{can}}(q,\omega)}{nS(q)} = \left[1-\frac{\omega_1^2(q)}{\omega_2^2(q)}\right]\delta(\omega) + \frac{\omega_1^2(q)}{\omega_2^2(q)}\delta\left(\omega^2-\omega_2^2(q)\right),$$

The validity of this result was confirmed numerically in [10] and also in [17] by comparison with numerical data on the dynamic characteristics of OCP's. It implies that, at least in classical OCPs, we can calculate the DSF and the collective mode characteristics entirely in terms of the static structure factor (SSF), $S(q)$, it makes it self-consistent. Indeed, due to the classical version of the FDT,

$$\frac{\omega_1^2(q)}{\omega_p^2} = \frac{q^2\omega_p^2}{3\Gamma S(q)}, \tag{52}$$

and the coupling-related

$$\frac{\omega_2^2(q)}{\omega_p^2} = \zeta(q) + \frac{q^2}{\Gamma} + \\ + \frac{1}{12\pi}\int_0^\infty p^2(S(p)-1)\Psi(p)dp \tag{53}$$

where

$$\Psi(p) = \left(\int_{|p-q|}^{p+q} \frac{\zeta(s)\left(p^2-q^2-s^2\right)^2 ds}{pq^3 s} - \frac{8\zeta(p)}{3} \right)$$

,

is also determined by the SSF and the one-species form-factor, since in OCPS's H = 0. Numerical results obtained on the basis of the relations (50, 51, 52, 53) are presented in the following figures. The displayed quantitative agreement with the numerical simulation data the viability and robustness of the self-consistent moment approach.

3.2.1. The OCP numerical data.

As an example, I reproduce here our results published last year in [17]. To stress that here we employ no adjustment parameters whatsoever.

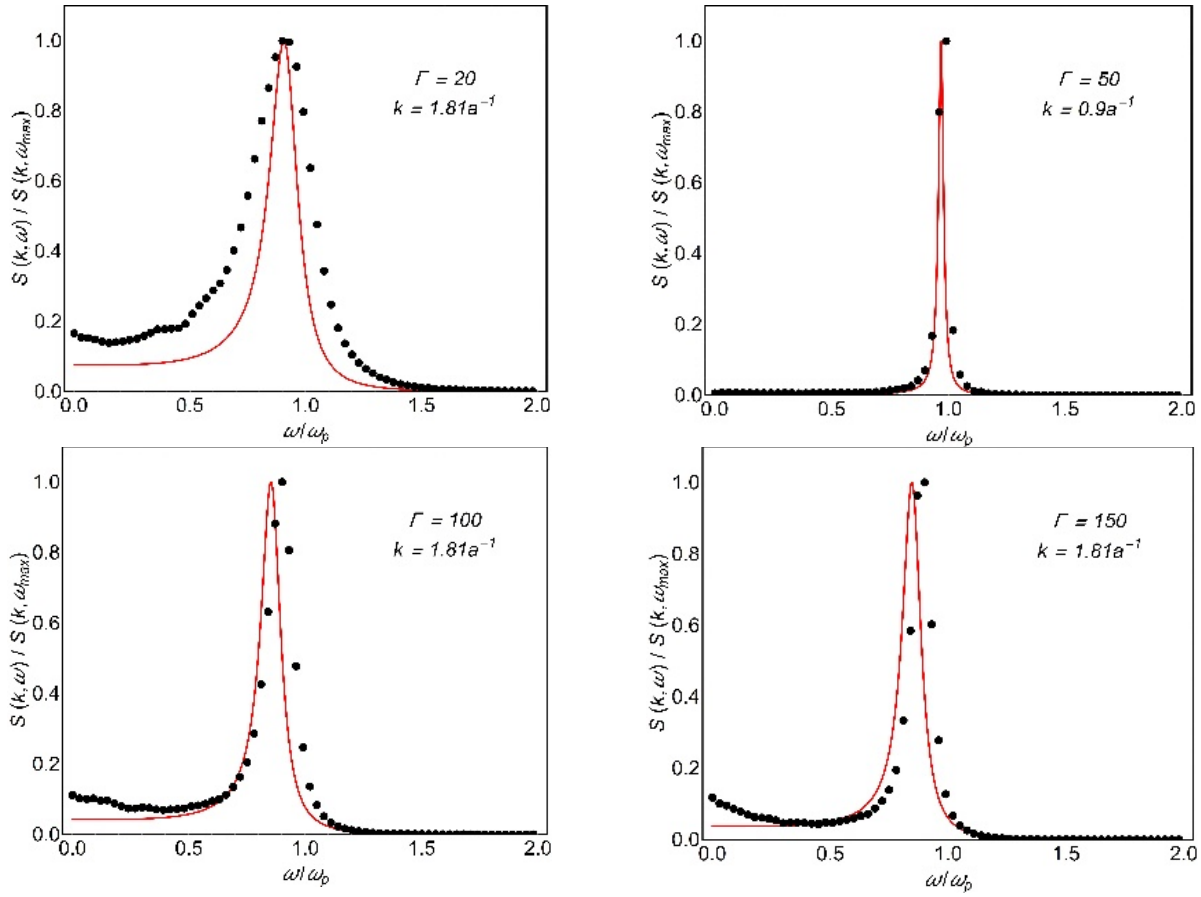

Figure 1 – Dynamic structure factor normalized to the shifted maxima values in strongly coupled COCPs, compared to the MD results [17], at various values of Γ and k

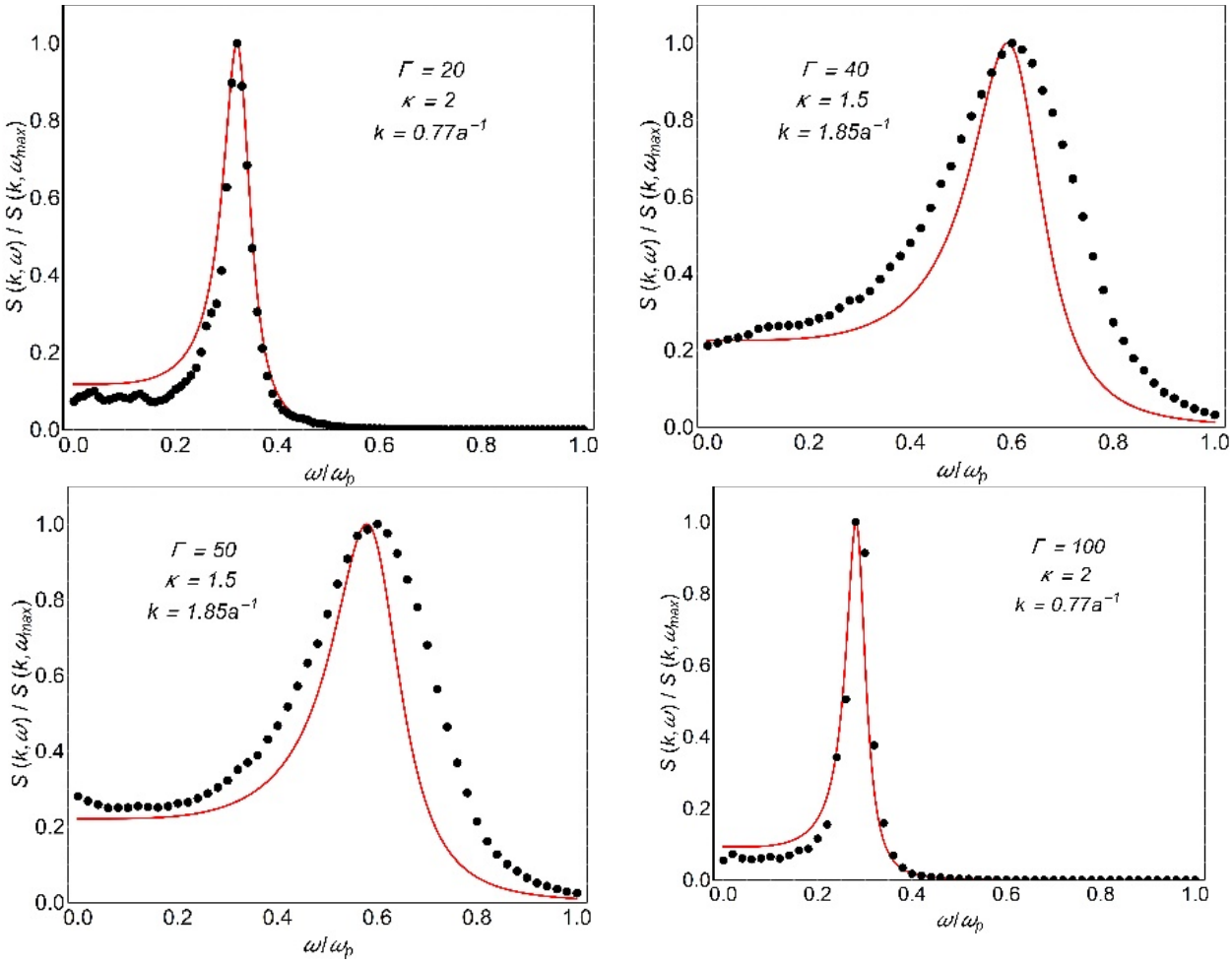

Figure 2 – As in Figure 1 but in strongly coupled YOCPs, compared to the MD results [17]

4 The search for the Nevanlinna parameter function

As we have seen in the previous Section, the self-consistent moment approach is quantitatively suitable for the description of dynamic properties of classical OCPs. It is shown in [43] how the method can be successfully extended to the partially or completely degenerate electron gases. Nevertheless, the simplification (33) effectively limits the applicability of the method in the low-coupling regime where the Landau collisionless damping is usually described within the RPA. In other words, we wish to choose a model expression for the NPF capable of incorporating the low-Γ RPA-like behavior into the moment scheme.

Here, we consider three different model expressions for the dynamic renormalized NPF $Q_2(\omega;q)$ both for classical and partially degenerate systems. Notice that in the physical context the variable t becomes frequency ω and we must take into account the spatial dispersion of the dynamic characteristics by introducing the (dimensionless) wavenumber variable q.

We start observing that the loss function effectively depends only on dimensionless variables

$$x = \frac{\omega^2}{\omega_p^2},\ x_j = \frac{\omega_j^2}{\omega_p^2},\quad j = 1,2\,. \tag{54}$$

This implies that the dimensionless NPF can be written as

$$\frac{Q_2(\omega;q)}{\omega_p} = \sqrt{\frac{x}{x_0}}X\left(\frac{x}{x_0}\right) + iY\left(\frac{x}{x_0}\right), \tag{55}$$

where x_0 is the characteristic value of the new variable equal to $k^2v_{th}^2 = 2q^2/3\Gamma$ or $k^2v_F^2 = q^2v_F^2/a^2$, respectively, in the classical and quantum-mechanical cases, v_{th} and v_F being, certainly, the thermal and Fermi velocities. Indeed, then the frequency-dependent part of the r.h.s. of (31) can be written as a function of $y = x/x_0$ and from the condition of the loss function extremum at the point $y = 0$ we obtain:

$$h = \frac{x_2}{\sqrt{x_1}} \frac{1}{\sqrt{W_1(2W_1 - W_2x_1)} - W_0\sqrt{x_1}} , \qquad (56)$$

Where we have introduced the following values of the functions X, Y and of the derivative Y' at $y = 0$:

$$X_0 = hW_0 , \; Y_0 = hW_1 , \; Y_0^{'} = hW_2 .$$

Observe that if $Y_0 = h$; and $X_0 = Y_0' = 0$ so that $W_1 = 1$, $W_0 = 0$, $W_2 = 0$, we return to the "static" approximation,

$$h = \frac{x_2}{\sqrt{2x_1}} = h_0 .$$

4.1. Classical Coulomb OCPs.

Presume first that the NPF is the plasma dispersion function [44], i.e., put

$$\frac{Q_2(\omega;q)}{\omega_p} = \sqrt{\frac{x}{x_0}} X\left(\frac{x}{x_0}\right) + iY\left(\frac{x}{x_0}\right) = , \qquad (57a)$$
$$= \frac{h}{\sqrt{\pi}} Z\left(\frac{\omega + i0^+}{q\sqrt{2/(3\Gamma)}}\right)$$

where

$$Z(\zeta = \xi + i0^+) = \mathrm{i}\sqrt{\pi}\exp(-\xi^2) - 2F(\xi) ,$$
$$\xi = \frac{\omega}{q\sqrt{2/(3\Gamma)}} = \sqrt{\frac{x}{x_0}} \in \mathbb{R}$$

with

$$F\left(\frac{x}{x_0}\right) = \sqrt{\frac{x}{x_0}} \exp\left(-\frac{x}{x_0}\right) \int_0^1 \exp\left(\frac{xs^2}{x_0}\right) ds \qquad (58)$$

being the Dawson integral

$$Z(\xi + i0^+) = i\sqrt{\pi}\exp(-\xi^2) - 2F(\xi) . \qquad (59)$$

A simple variable substitution leads to the alternative representation of (58),

$$X(x) = -\frac{2h}{\sqrt{\pi}} \exp\left(-\frac{x}{x_0}\right) \int_0^1 \exp\left(\frac{xs^2}{x_0}\right) ds ,$$
$$Y(x) = h\exp\left(-\frac{x}{x_0}\right)$$

so that

$$X_0 = -\frac{2h}{\sqrt{\pi}} , \; Y_0 = h , \; Y_0^{'} = -\frac{h}{x_0}$$

or

$$W_0 = -\frac{2}{\sqrt{\pi}} , W_1 = 1 , W_2 = -\frac{1}{x_0}$$

Then, it stems from (56) that in this case

$$h_{RPA} = \frac{x_2\sqrt{x_0}}{\sqrt{x_1}} \frac{\pi\sqrt{x_1 + 2x_0} - 2\sqrt{\pi x_1 x_0}}{2\pi x_0 + \pi x_1 - 4x_0x_1}$$

Alternatively, we might introduce an adjustable parameter and redefine:

$$\frac{Q_2(\omega;q)}{\omega_p} = \sqrt{\frac{x}{x_0}} X\left(\frac{x}{x_0}\right) + iY\left(\frac{x}{x_0}\right) = \qquad (57b)$$
$$= \frac{ih}{\alpha + \frac{i(\alpha - 1)}{\sqrt{\pi}} Z\left(\frac{\omega + i0^+}{q\sqrt{2/(3\Gamma)}}\right)} ,$$

Somewhat more cumbersome but straightforward calculations lead in this case to

$$h_{inv} = \frac{x_2}{\sqrt{x_1}} \frac{\sqrt{\pi x_0}}{\sqrt{2\pi x_0 - (1-\alpha)(\pi + 4(1-\alpha))x_1} - 2(1-\alpha)\sqrt{x_0 x_1}}$$

which tends to h_0 when $\alpha \to 1$. Notice that the parameter α, generally speaking, can be fixed by the Shannon-entropy maximization procedure [14].

4.2. Partly degenerate Coulomb OCPs.

There is a number of quantum-mechanical generalizations of the plasma dispersion function, see [45]. Consider, following D.B. Melrose and A. Mushtaq [46], the following generalization of (57a) (a misprint in the original paper is corrected)

$$Z(\zeta;\eta) = \frac{2}{\sqrt{\pi}} \int_0^\infty \frac{t \ln\left(\frac{t-\zeta}{t+\zeta}\right)}{\exp\left(t^2\right) + \exp(\eta)} dt = \tag{60}$$

$$= \frac{2}{\sqrt{\pi}} \int_{-\infty}^\infty \frac{t \ln(t-\zeta)}{\exp\left(t^2\right) + \exp(\eta)} dt = \tag{61}$$

$$= \frac{1}{\sqrt{\pi}} \int_{-\infty}^\infty \frac{\ln\left(1 + \exp(\eta - t^2)\right)}{\exp(\eta)} \frac{dt}{t-\zeta}$$

where $\xi = (\omega + i0^+)/(qv_{\text{eff}}/a)$ with, perhaps, $v_{\text{eff}} = v_F$. As usually, η is the dimensionless chemical potential. This function satisfies the following classical limiting property:

$$Z(\zeta;\eta \to -\infty) \cong Z(\zeta) \ ,$$

By definition, with x defined as in (54),

$$\operatorname{Im} Z(x;\eta) = \sqrt{\pi} \frac{\ln\left(1 + \exp\left(\eta - \frac{x}{x_0}\right)\right)}{\exp(\eta)} \underset{\eta\to-\infty}{\cong} \tag{62}$$

$$\underset{\eta\to-\infty}{\cong} \sqrt{\pi} \exp\left(-\frac{x}{x_0}\right)$$

and

$$\operatorname{Re} Z(x;\eta) = \frac{2}{\sqrt{\pi}} P.V. \int_0^\infty \frac{t \ln\left|\frac{t-\sqrt{x/x_0}}{t+\sqrt{x/x_0}}\right|}{\exp\left(t^2\right) + \exp(\eta)} dt$$

Observing that

$$\frac{t \ln\left|\frac{t-\sqrt{x/x_0}}{t+\sqrt{x/x_0}}\right|}{\exp\left(t^2\right) + \exp(\eta)} = -\frac{2}{e^\eta + e^{t^2}} \sqrt{x/x_0} + O\left(x^{3/2}\right)$$

one obtains that

$$\frac{\operatorname{Re} Z(x;\eta)}{\sqrt{\pi}} = \frac{2}{\pi} P.V. \int_0^\infty \frac{t \ln\left|\frac{t-\sqrt{x/x_0}}{t+\sqrt{x/x_0}}\right|}{\exp\left(t^2\right) + \exp(\eta)} dt \underset{x\downarrow 0}{\cong}$$

$$\underset{x\downarrow 0}{\cong} \sqrt{x/x_0}\,\Xi(x)$$

and that

$$\Xi(0) = \Xi_0 = -\frac{4}{\pi} \int_0^\infty \frac{dt}{\exp\left(t^2\right) + \exp(\eta)} =$$

$$= -\frac{2e^{-\eta}}{\pi} \int_0^\infty \frac{s^{-1/2} ds}{\exp(s-\eta) + 1} = -\frac{2e^{-\eta}}{\pi} F_{-1/2}(\eta) \, .$$

Now, from (62),

$$\Upsilon_0 = \frac{\operatorname{Im} Z(0;\eta)}{\sqrt{\pi}} = \frac{\ln\left(1 + \exp(\eta)\right)}{\exp(\eta)},$$

$$\Upsilon_0' = -\frac{1}{x_0(e^\eta + 1)} \ .$$

So, if one introduces the low-frequency NPF for partially degenerate plasmas as

$$\frac{Q_2(\omega;q)}{\omega_p} = h_{qm}\left(\sqrt{\frac{x}{x_0}}\Xi(x) + i\Upsilon(x)\right), \tag{63}$$

then,

$$w_0 = \Xi_0 = -\frac{2e^{-\eta}}{\pi}\int_0^\infty \frac{s^{-1/2}ds}{\exp(s-\eta)+1},$$

$$w_1 = \Upsilon_0 = \frac{\ln(1+\exp(\eta))}{\exp(\eta)},$$

$$w_2 = \Upsilon_0^{'} = -\frac{1}{x_0(e^{\eta}+1)},$$

$$h_{qm} = \frac{x_2}{\sqrt{x_1}}\frac{1}{\sqrt{w_1(2w_1 - w_2x_1)} - w_0\sqrt{x_1}}.$$

In other words, this new NPF equals

$$\frac{Q_2(\omega;q)}{\omega_p} = \frac{h_{qm}}{\sqrt{\pi}}\left(\mathrm{Re}\,Z(x;\eta) + i\,\mathrm{Im}\,Z(x;\eta)\right), \quad (64)$$

where the function $Z(x;\eta)$ is determined in (60) and (61). The formula for the DSF function is, as before,

$$\frac{\pi S(q,\omega)}{nS(q)} = B(\beta\hbar\omega)\frac{\omega_1^2(\omega_2^2-\omega_1^2)\,\mathrm{Im}\,Q_2(t)}{\left|D_3(t)+Q_2(t)D_2(t)\right|}, \quad (65)$$

The numerical data with respect to the above frequency-dependent NPFs is presented in the next Sect. The completely degenerate case is to be considered elsewhere.

4.3. Numerical data on the dynamic NPFs

4.3.1. Classical plasmas.

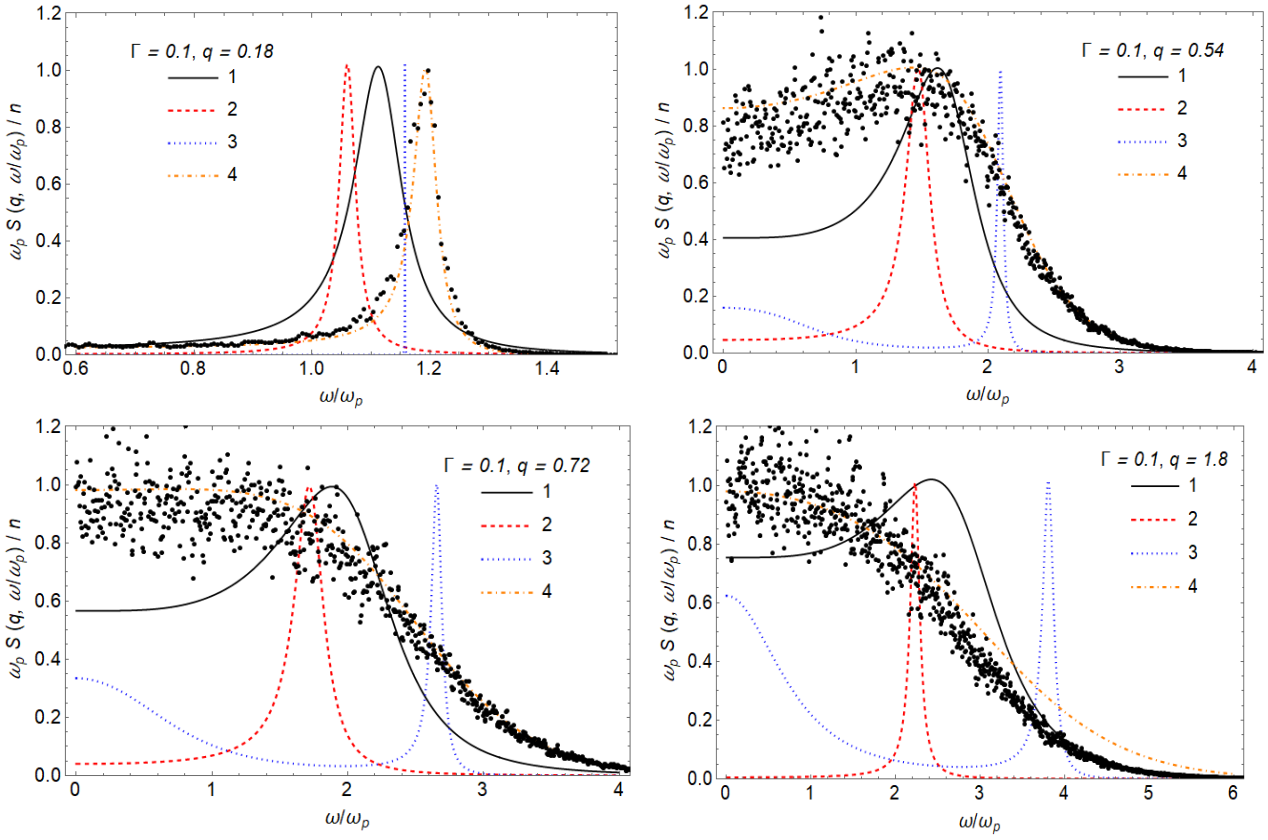

Figure 3 – Dynamic structure factor fot the COCP presenting the method of moments (MM) data vs. the MD data (dots). 1 – MM with $\frac{Q(q)}{\omega_p} = ih_0$, 2 – MM with $\frac{Q(q)}{\omega_p}$ from (57b), with $\alpha = 0.5$, 3 – MM with $\frac{Q(q)}{\omega_p}$ from (57a), 4 – RPA theory

4.3.2. Partly degenerate plasmas.

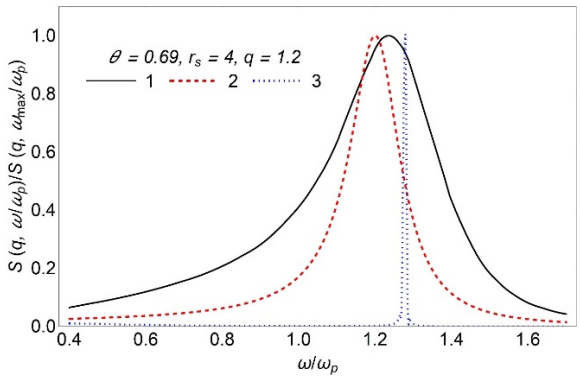

Figure 4 – Dynamic structure factor for partly degenerate OCPs (electron gas), MM data vs. data of [47].

1 – [47], 2 – MM with $\frac{Q(q)}{\omega_p} = ih_0$, 3 – MM with $\frac{Q_2(\omega;q)}{\omega_p}$ from (64)

5 Conclusions

A thorough review of the self-consistent method of moments is presented. Ways are discussed of qualitative improvement of the method consisting in the employment of different dynamic models of the Nevanlinna parameter function (NPF) analogous to the dynamic local-field correction function [12]. The latter is used to extend the realm of applicability of the random-phase approximation (RPA). Though the self-consistent method of moments with a static NPF (56) has proven to work very well in warm dense matter, our preliminary results demonstrate that the suggested model NPFs provide a satisfactory agreement with the simulation data in low-density Coulomb plasmas. Further steps along this path are planned to be taken, especially in the case of partly and completely degenerate systems. Finally, we stress that no adjustment parameters are used in our calculations.

Acknowledgments

The author is thankful to the al-Farabi Kazakh National University for its hospitality and to D. Dubovtsev for his aid with computations.

References

1. J.S. Ross et al. Transition from collisional to collisionless regimes in interpenetrating plasma flows on the National ignition facility // Phys. Rev. Lett. – 2017. – Vol. 118. – P. 185003.

2. J. Daligault. Crossover from classical to Fermi liquid behavior in dense plasmas // Phys. Rev. Lett. – 2017. – Vol. 119. – P. 045002.

3. M. S. Murillo. Strongly coupled plasma physics and high energy-density matter // Phys. Plasmas. – 2004. – Vol. 11. – P. 2964.

4. Mi Yan, B. J. DeSalvo, Ying Huang, P. Naidon, T. C. Killian. Rabi oscillations between atomic and molecular condensates driven with coherent one-color photoassociation // Phys. Rev. Lett. – 2013. – Vol. 111. – P. 150402.

5. J. Daligault, S. D. Baalrud, C. E. Starrett, D. Saumon, T. Sjostrom. Ionic transport coefficients of dense plasmas without molecular dynamics // Phys. Rev. Lett. – 2016. – Vol. 116. – P. 075002.

6. J. P. Mithen, J. Daligault, B. J. B. Crowley, G. Gregori. Density fluctuations in the Yukawa one-component plasma: An accurate model for the dynamical structure factor // Phys. Rev. E. – 2011. – Vol. 84. – P. 046401.

7. J.P. Mithen, J. Daligault, G. Gregori. Comparative merits of the memory function and dynamic local-field correction of the classical one-component plasma // Phys. Rev. E. – 2012. – Vol. 85. – P. 056407.

8. G. Kalman, K.I. Golden. Response function and plasmon dispersion for strongly coupled Coulomb liquids // Phys. Rev. A. – 1990. – Vol. 41. – P. 5516.

9. T. Meyer, I.M. Tkachenko. Highfrequency electrical conductivity and dielectric function of strongly coupled plasmas // Contrib. Plasma Phys. – 1985. – Vol. 25. – P. 437.

10. Yu. V. Arkhipov, A. B. Ashikbayeva, A. Askaruly, A. E. Davletov, I.M. Tkachenko. Dielectric function of dense plasmas, their stopping power, and sum rules // Phys. Rev. E. – 2014. – Vol. 90. – P. 053102; ibid. – 2015. – Vol. 91. – P. 019903.

11. J. Ortner, V.M. Rylyuk, and Tkachenko. Reflectivity of cold magnetized plasmas // Phys. Rev. E. – 1994. – Vol. 50. – P. 4937.

12. Yu.V. Arkhipov, A. Askaruly, D. Ballester, A.E. Davletov, I. M. Tkachenko, G. Zwicknagel. Dynamic properties of one-component strongly coupled plasmas: The sum-rule approach // Phys. Rev. E. – 2010. – Vol. 81. – P. 026402.

13. D. Ballester, I. M. Tkachenko. Fast-projectile stopping power of quantal multicomponent strongly coupled plasmas // Phys. Rev. Lett. – 2008. – Vol. 101. – P. 075002.

14. I. M. Tkachenko, Y. V. Arkhipov, and A. Askaruly. The method of moments and its applications in plasma physics. – Saarbrücken: Lambert, 2012.

15. M.G. Krein, A.A. Nudel'man. The Markov moment problem and extremal problems. – Moscow: Nauka, 1973 [in Russian].

16. N.I. Akhiezer. The classical moment problem. – Moscow: Nauka, 1961 [in Russian].

17. Yu. V. Arkhipov, A. Askaruly, L. Conde, A. E. Davletov, Z. Donkó, D. Yu. Dubovtsev, P. Hartmann, I. Korolov, I. M. Tkachenko. Direct determination of dynamic properties of Coulomb and Yukawa classical one-component plasmas // Phys. Rev. Lett. – 2017. – Vol. 119. – P. 045001.

18. V.M. Adamyan, I.M. Tkachenko. Solution of the truncated Hamburger moment problem according to M.G. Krein // Operator Theory: Advances and Applications. – 2000. – Vol. 118. – P. 33.

19. M.G. Krein, A.A. Nudel'man. The Markov moment problem and extremal problems. – New York: Providence, 1977.

20. D. Varentsov, I.M. Tkachenko, D.H.H. Hoffmann. Statistical approach to beam shaping // Phys. Rev. E. – 2005. – Vol. 71. – P. 066501.

21. V.M. Adamyan, I. M. Tkachenko. Truncated Hamburger moment problems with constraints // North-Holland Mathematical Studies. – 2001. – Vol. 189. – P. 321.

22. M. Urrea, I.M. Tkachenko, P. Fernández de Córdoba // J. Applied Analysis. – 2001. – Vol. 7. – P. 209.

23. R.E. Curto, L.A. Fialkow. Recursiveness, positivity, and truncated moment problems // Houston J. Math. – 1991. – Vol. 17. – P. 603-635.

24. T. Carleman. Sur les fonctions quasi-analytiques // Comptes rendus du Ve Congres des Mathematiciens Scandinaves, 1922.

25. T. Carleman. Les fonctions quasi analytiques. Paris: Gauthier-Vilars, 1926.

26. G.H. Hardy. Contributions to the theory of the Riemann zeta-function and the theory of the distribution of primes // Messenger of Mathematics. – 1917. – Vol. 47. – P. 175.

27. L.D. Landau, E.M. Lifshitz, L.P. Pitaevskii, Electrodynamics of Continuous Media. – Oxford: Butterworth-Heinemann, 1984.

28. A.A. Kugler. Collective modes, damping, and the scattering function in classical liquids // J. Stat. Phys. – 1973. – Vol. 8. – P. 107.

29. V.M. Adamyan, T. Meyer, I.M. Tkachenko. RF dielectric constant of a collisional plasma // Sov. J. Plasma Phys. – 1985. – Vol. 11. – P. 481.

30. V.M. Adamyan, I.M. Tkachenko. High-frequency electric conductivity of a collisional plasma // Teplofizika Vysokikh Temperatur. – 1983. – Vol. 21. – P. 417.

31. V.L. Ginzburg. Theory of propagation of radiowaves in the ionosphere. – Moscow: Gostekhizdat, 1949 [in Russian].

32. L.D. Landau, E.M. Lifshitz, Quantum Electrodynamics. – Moscow: Nauka, 1975 [in Russian].

33. V. I. Perel' and G. M. Eliashberg // Zh. Eksp. Teor. Fiz. – 1961. – Vol. 41. – P. 886.

34. A. Selchow, G. Röpke, A. Wierling. Dynamic structure factor for a two-component model plasma // Phys. Rev. E. – 2001. – Vol. 64. – P. 056410.

35. S. Ichimaru. Strongly coupled plasmas: high-density classical plasmas and degenerate electron liquids // Rev. Mod. Phys. – 1982. – Vol. 54. – P. 1017.

36. K.I. Golden, G.J. Kalman. Quasilocalized charge approximation in strongly coupled plasma physics // Phys. Plasmas. – 2000. – Vol. 7. – P. 14.

37. A. Wierling, T. Pschiwul, G. Zwicknagel. Dynamic response of a one-component plasma at moderate coupling // Phys. Plasmas. – 2002. – Vol. 9. – P. 4871.

38. S. Alexander, P.M. Chaikin, P. Grant, G.J. Morales, P. Pincus, and D. Hone. Charge renormalization, osmotic pressure, and bulk modulus of colloidal crystals: Theory // J. Chem. Phys. – 1984. – Vol. 80. – P. 5776..

39. S.L. Gilbert, J.J. Bollinger, and D.J. Wineland. Shell-structure phase of magnetically confined strongly coupled plasmas // Phys. Rev. Lett. – 1988. – Vol. 60. – P. 2022.

40. S. Ichimaru. Nuclear fusion in dense plasmas // Rev. Mod. Phys. – 1993. – Vol. 65. – P. 255.

41. H. Ohta, S. Hamaguchi. Wave Dispersion Relations in Yukawa Fluids // Phys. Rev. Lett. – 2000. – Vol. 84. – P. 6026.

42. I. M. Tkachenko. Book of abstracts of the international conference on operator theory and applications in mathematical physics, Będlewo, Poland. – 2004. – P. 20.

43. Yu.V. Arkhipov, A.B. Ashikbayeva, A. Askaruly, M. Bonitz, L. Conde, A.E. Davletov, T. Dornheim, D.Yu. Dubovtsev, S. Groth, Kh. Santybayev, S.A. Syzganbayeva, I.M. Tkachenko. Sum rules and exact inequalities for strongly coupled one-component plasmas // Contrib. Plasma Phys. – 2018. – Vol. 58. Accepted to publication: https://doi.org/10.1002/ctpp.201700136.

44. J.D. Huba. NRL plasma formulary, Washington DC: Naval Research Laboratory, 2007.

45. K.V. Starikov, C. Deutsch. Stopping of relativistic electrons in a partially degenerate electron fluid // Phys. Rev. E. – 2005. – Vol. 71. – P. 026407.

46. D.B. Melrose, A. Mushtaq. Dispersion in a thermal plasma including arbitrary degeneracy and quantum recoil // Phys. Plasmas. – 2010. – Vol. 17. – P. 122103.

47. N.-H. Kwong, M. Bonitz. Real-Time Kadanoff-Baym Approach to Plasma Oscillations in a Correlated Electron Gas // Phys. Rev. Lett. – 2000. – Vol. 84. – P. 1768.

IRSTI 29.19.17

Ionization equilibrium between electrons and holes in bilayers and adiabatic approximations

A.P. Chetverikov[1], W. Ebeling[2, *] and M.G. Velarde[3]

[1]*Faculty of Physics, Saratov State University, 83, Astrakhanskaya str., R-410012 Saratov, Russia*
[2]*Institute of Physics, Humboldt University of Berlin, 15, Newtonstr., D-12489 Berlin, Germany*
[3]*Multidisciplinary Institute, Complutense University of Madrid, Paseo Juan 23, 1, E-28040 Madrid, Spain*
**e-mail: ebeling@physik.hu-berlin.de*

We analyze the ionization equilibrium between the charges in nonlinear bilayers formed by triangular planar atomic lattices. We consider a system consisting of two separated buy a dielectric medium and independently gated layers 1 and 2 separated by a dielectric medium with ε with equal density of electrons in first layer 1 and holes in second layer 2. Assuming that the upper layer is doped with electrons and in the lower layer is doped with holes, we study of the formation, the dynamics and the thermodynamics of bound states. Beside electron – hole pairing we are including bound states with solitonic excitations. We investigate the ionization of electron – hole pairs and discuss the influence of solitons on bound electron-hole pairs; her we use the adiabatic approximation assuming at any time local equilibrium. So far we concentrated here on several thermodynamics and dynamic effects, as the Coulomb attraction between electrons and holes, the formation of electron – hole atoms and degeneration effect. Further we investigated the ionization equilibrium and the coupling to solitonic excitations.

Key words: ionization processes, electrons, holes, solitons, bose condensation.
PACS numbers: 05.60.-k, 05.45.Yv, 63.20.Ry, 71.38.-k, 73.63.-b.

1 Introduction

Ionization problems are a classical topic of plasma physics [1, 2]. In recent time new problems have appeared in connection with plasmas in low-dimensional nanosystems [3, 4, 5], in particular with plasmas in bilayers [3]. The coupling of electrons injected into one layer to holes injected into a second layer has been studied already long ago [6, 7, 8, 9] including the prediction of observing electron – hole pairs, which are rather stable bosons inluding possible high – temperature electron – hole superfluidity and other interesting effects [3, 6, 8, 10, 11]. We plan to study here related problems from the point of view of plasma physics including some problems related to the coupling of the charge dynamics to the lattice excitations in nonlinear lattices. An example is the interaction of acoustic lattice soliton excitations in 2d – lattices to imbedded electrons, and the effect of electron surfing [12, 13, 14] including transport [13, 14, 15], and control effects [15, 16]. The lattice excitations may have different origin such as thermal excitations or e.g. mechanical or electrical shocks generated by contacts of the tip of an electron field microscope with a suitable anharmonic crystal lattice layer. For example in simulations a few hundred atoms on a plane forming triangular [13] or hexagonal lattices [16] interacting with one or a few added, excess electrons were studied.

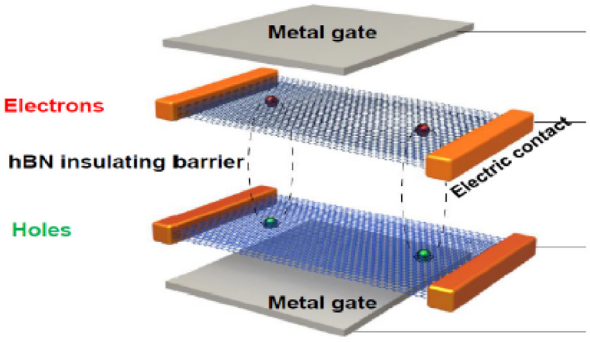

Figure 1 – Schema of a bilayer located between two metal gates and with an insulating layer in between adapted after [3]. The layers have electric contacts and may be doped with electrons in the upper layer and with holes in the lower one. The electrical attracting forces are demonstrated by dashed lines between electrons and holes [3]

Here we want to study similar effects in bilayers, consisting of two lattice layers in small distance. The recent fabrication of two very close, but electrically isolated, conducting bilayer graphene sheets, one doped with electrons and the other with holes with tunable densities, raises exciting new possibilities [17, 18, 19].

We will discuss the following problems:

1) electron and a hole are able to form a stable localized pair already in unperturbed bilayer lattices. The pairs are like a Hydrogen atoms, which are near to classical pairs. Collaps is prevented due to existence of a minimal length given by the distance of the layers.

2) The excitations of solitons in either of the lattices may carry not only individual charges but also pairs.

3) This leads to a variety of possibilities, among them new "vacuum cleaner" effects, a soliton will trap an already localized electron-hole pair and we may control this way the motion of pairs.

Let us consider now the forces and other physical effects in doped bilayers:

We consider a system consisting of two separated buy a dielectric medium and independently gated layers 1 and 2 separated by a dielectric medium with ε with equal density of electrons in first layer 1 and holes in second layer 2. Let us first discuss the physical effects to be expected. At large distances, the two layers are uncoupled and the state is expected to be similar to what we observed and described on one – layer systems [13, 14, 15, 16]. In the case that the two layers come closer together, the Coulombic forces between electrons and holes come into play and at small distances e-h pairing can occur due to Coulomb interaction. At lower densities we may neglect the Coulombic forces between the electrons in one layer and the holes in the other one. The forces are repulsive and try to keep the charges far from each other, therefore a close meeting of two equally charged particles is rather seldom.

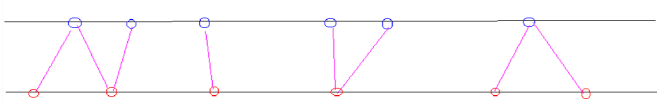

Figure 2 – State of a bilayer: The upper layer is doped with electrons and the lower one with holes. The attracting Coulomb forces between electrons and holes lead to pairing effects. Thermal effects tend to destroy the pairing at mediate and higher temperatures

We assume the following interaction between an electron in upper layer 1 and a hole in lower layer 2. For the electron – hole interaction we assume the true Coulomb potential

$$V_{eh}\left(x_i^1, y_i^2, x_j^2, y_j^2, d\right) =$$

$$= -\frac{e^2}{\varepsilon[(x_i^1 - x_j^2)^2 + (y_i^1 - y_j^2)^2 + d^2]^{1/2}}. \qquad (1)$$

where $\varepsilon \simeq 3$ is an effective dielectric constant, $d \simeq 1nm$ is the distance between the layers and $x_i^1, y_i^2, x_j^2, y_j^2$ are the respective coordinates in the upper layer 1 doped with electrons and the lower layer doped with holes 2. We mention that this potential has been used in earlier work [20] Note that Efimkin et al. [9] and Conti et al. [11] use different formulae in Fourier representation for the description of the forces, e.g. we find in [11] the "ansatz"

$$V_{eh}(k, k') = -2\pi \frac{e^2 \exp(-d|k-k'|)}{\varepsilon|k-k'|}. \qquad (2)$$

At low temperatures and small distances between the layers, bound states will be formed, due to the attracting Coulomb forces between electrons and holes. In particular we expect pairing effects which lead to a kind of excitons which are bosons [6]. Thermal effects will create ionization effects which destroy the pairing at mediate and higher temperatures.

In our simulations we used for modeling the electron dynamics the tight-binding approximation (TBA) (which is entirely different from the tools used by Conti et al. [11]) and for the lattice particles we use her as in earlier work a classical Hamiltonian albeit with the Morse interactions. As a result of this mixed anharmonic classical-quantum TBA dynamics we could show that the charges “like" to follow the trajectories of soliton-like excitations. In the 1d case we have predicted several interesting phenomena, in particular the “vacuum-cleaner" effect, i.e., the electron probability density is gathered by solitons which along their trajectory act as long range correlators.

2 Interactions and solitonic excitations in bilayers

We assume that effects connected with polarization and polaron effects are small. The atoms repel each other exponentially and attract each other with weak dispersion forces. The characteristic length determining equilibrium distance between the particles in the lattice is σ which is used as the length unit. Using the relative distance $r^s = |r_n^s - r_j^s|$ for two atoms in layer with number s we introduce the Morse potential: we set

$$V(r^s) = \\ = D\{\exp[-2b(r^s - \sigma)] - 2\exp[-b(r^s - \sigma)]\}. \quad (3)$$

By imposing the cutoff of the potential at 1.5σ, we exclude unphysical cumulative interaction effects arising from the influence of lattice units outside the first neighborhood of each atom [13]. The lattice solitons along crystallographic axes in 2 coupled two-dimensional anharmonic crystal lattices are rather independent.

For the electrons and holes we will use essentially the model described above. Just as an illustration we may show Figs. obtained earlier for one layer systems. In Figure 4 we show an unperturbed triangular lattice.

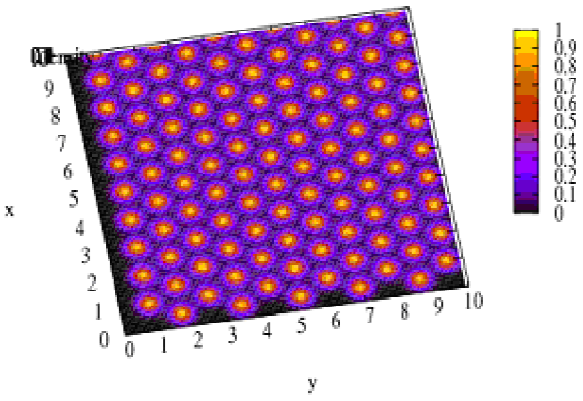

Figure 3 – Triangular Morse lattice. The lattice sites in one layer are represented by small Gaussian clouds

Solitons may be created for example by kicks at the border of the lattice. The soliton which is moving along a crystallographic axis can be excited by a strong pulse of velocity v_0 imposed at $t = 0$. The high-energetic soliton excited this way is quite long lasting in its motion along the chosen crystallographic axis. Transverse excitations and thermal collisions do not play a significant role in the interval of observation.

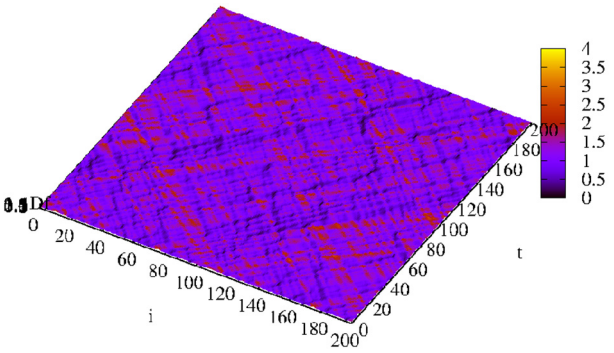

Figure 4 – Solitonlike excitation along a oedimensional crystallographic axis represented as a stripes showing position over time. We show only the lattice sites in one layer. by small Gaussian clouds

Solitonic excitations may also be created by thermal collisions [13, 14]. Since solitons are local compressions of the lattice these clusters of atoms generate a potential hole in which charges density might be concentrated. Any displacement of the atoms changes the polarization energy. The charge density will try to follow up these changes. This is the basic effect leading to the effect of solectron formation [13, 14]. For the following discussion we have to notice that any soliton created in the lattice by mechanical or thermal effects, acts as an attractor for the charge density.

Solitons and electrons may form solectrons, no doubt may be that the same may happen with holes leading to solitonic holes solholes. So far we do not know much about the masses. Small masses are of large interest for BEC-effects

The soliton as it travels disturbs the lattice. This is connected with the emission of phonons, this process occurs in the phonon band. Only after a finite time which is about 5 time units in our example the lattice returns to the ordered crystalline state. In the intermediate time the lattice is in a non-crystalline state and unable to allow solitons to cross the path. Any second soliton which will cross the trace of an soliton in the delay time will get stuck. We have shown how this effect may be used for control.

The potential for the electron – hole interaction may be represented as

$$V_{eh}\left(x_i^1, y_i^2, x_j^2, y_j^2, d\right) = -\frac{e^2}{\varepsilon d\sqrt{1+\frac{\rho^2}{d^2}}}, \quad (4)$$

$$\rho^2 = x^2 + y^2; \qquad x = \left(x_i^1 - x_j^2\right); \\ y = \left(y_i^1 - y_j^2\right) \quad (5)$$

Here is ρ the horizontal distance.

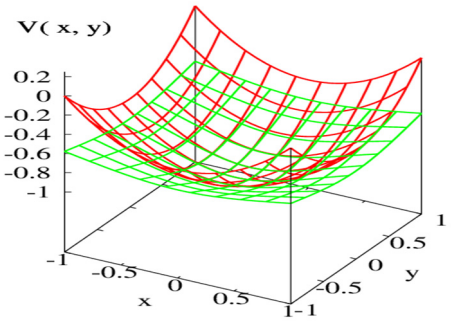

Figure 5 – The potential of the effective horizontal force between electron and hole, including also the parabolic approximation which is valid only for small $\hbar\omega$

3 Modeling charge pairing and bound states

For the quantum – mechanical treatment of electron – hole pairs, a parabolic approximation of the quite difficult interaction potential is useful. For small distances ρ follows in quadratic approximation

$$V_{eh}(\rho,d) = -\frac{e^2}{\varepsilon d\sqrt{1+(\rho^2/d^2)}} \simeq \frac{e^2}{\varepsilon d}[-1+\frac{\rho^2}{2d^2}]+\ldots$$

The parabolic approximation corresponds to a two-dimensional oscillator with frequency

$$m\omega^2 = \frac{e^2}{\varepsilon d^3} \qquad (7)$$

The classical value of the ground state energy of an electron – hole pair, which is a lower bound reads $e^2/\varepsilon d$, and the quantum-mechanical bound states in this potential are in first approximation the known oscillator states

$$E_{n_x,n_y} = -\frac{e^2}{\varepsilon d} + \hbar\omega[\frac{1}{2}+n_x+n_y] \qquad (8)$$

with the ground state

$$E_{0,0} = -\frac{e^2}{\varepsilon d} + \frac{1}{2}\hbar\omega \qquad (9)$$

The condition for the existence of discrete bound states is

$$\hbar\omega < 2\frac{e^2}{\varepsilon d} \qquad (10)$$

or expressed in other parameters

$$\frac{\varepsilon}{d} > 4\frac{e^2}{\hbar^2}. \qquad (11)$$

As we see, the condition for the existence of discrete bound states, which we need, is that the distance between the layers is sufficiently small. In order to give an example we assume $\varepsilon\sim3$ and $d\sim1$ nm, then we arrive at Bohr radii of about a few nm and ground state energies with an order of magnitude around 0.1 eV or maybe more generally binding energies in the range $10^{-2}-1\,0^{-1}$ eV. A rule of thumb known from plasma physics is that interesting ionization phenomena are to be expected at temperatures in the region of $T\sim0.1|E_0/k_B|$ and this estimate leads in our case to temperatures around 100 K (or maybe more generally in the range 10 K – 200 K. To be more precise, we need the exact data of the sample. Her we consider only the order of magnitude.

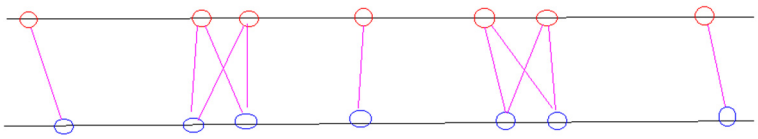

Figure 6 – Model of a bilayer at low temperatures with examples of pairing ("atoms","molecules"). The electrons in the upper layer and the holes in the lower layer are mostly paired and behave like excitons or $H-$ atoms which are bosons. Further we showed also two less stable molecules (double pairs) consisting of two electrons and two holes which appear to be similar to H_2-molecules and are also bosons

The potential of the horizontal forces between electrons and holes is represented in Figure 5 including the parabolic approximation.

What we can say about the possibility to form a kind of molecules e-h-e-h. A classical estimate of the energy of two pairs in a line in distance x is

$$E_0^{(2)}(x) = -2\frac{e^2}{\varepsilon d} + [2\frac{e^2}{\varepsilon x} - 2\frac{e^2}{2\varepsilon[x^2+d^2]^{1/2}}] \quad (12)$$

As far as we can see, the additional term is for any x – value positive, i.e. the formation of double pairs as shown in Figure 6 is of no energetic advantage. The only possibility to get negative additional contributions is to introduce between the two layers materials with still lower dielectric constant or a vacuum. We will therefore ignore here the formation of molecules, since quantum effects can only increase the ground state energy. We mention also the early finding of Lozovik and Yudson [6] that excitons in $2d$ repel each other what ensures the stability of an exciton gas against coalescence into biexcitons, droplets etc.. Lozovik and Yudson pointed out that this property, which is characteristic for the 2d case, makes transitions to a superfluid state possible. New in comparison to earlier studies is that we include the excitation of the quasiparticles solitons, being nonlinear compressions in the lattice (see Figure 7)

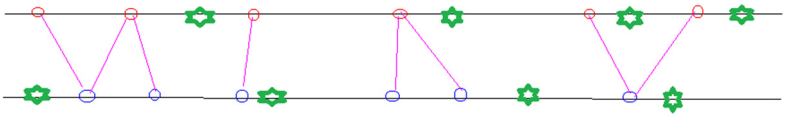

Figure 7 – Bilayer with electrons and holes including the excitation of solitons (here symbolized by green stars). These quasi-particles which are typical excitations in nonlinear lattices attract charges and may form bound states with them, being in upper layer the "solectrons" and in lower layer the "solholes"

4 Adiabatic Schrödinger equation in the presence of solitons

Let us assume that a soliton is passing an electron – hole pair and takes it with it. We may image that the e – h – pair is surfing on the top of the solitonic excitation This is a process of high complexity which may however be simplified and reduced in adiabatic approximation to a tractable model. The idea of adiabatic approximation for solectron systems has been developed in [12]. Let us assume that the soliton generates just a moving potential in which the electron and the hole are moving. Following the model developed earlier [15]. This model is based on a continuous description which consists of two equations, one for the effective Schrödinger equation for the wave function ϕ of the charges and the other one for the deformation density of the lattice. The effective Schrödinger equation for the charges $\rho(x,t)$ reads in the one – dimensional case [15]

$$i\hbar\phi_t(x,t) + \frac{\hbar^2}{2m}[\phi_{xx}] + g\rho(x,t)\phi(x,t) = 0, \quad (13)$$

The nonlinearities in the electron-lattice coupling appear in quite symmetrical way in the coupling constant

$$g = \chi + \alpha V_0$$

The term $(-g\rho)$ plays the role of an external potential in the Schrödinger equation. The compression density ρ is to be found from the Boussinesq equation [15]

$$\rho_{tt} - k_0\rho_{xx} + \gamma_0(\rho^2)_{xx} - \\ -\frac{1}{12}\rho_{xxxx} + g(\phi)_{xx} = 0 \quad (14)$$

In our case we have two dimensions x, y and two charges interacting by by a potential V. Further the Boussinesq equation is to be replaced by the Kadomzev – Petviashvili equation or generalizations as given in [21]. A generalization is the following modified Boussinesq equation for solectrons which differs from the original one only by shifted coefficients

$$\frac{\partial^2\rho(x,y,t)}{\partial t^2} - v_0^2\frac{\partial^2}{\partial x^2} - \frac{a^2}{12}\frac{\partial^4}{\partial x^4}\rho(x,y,t) \quad (15)$$

$$= \frac{v_0}{2}\frac{\partial^2}{\partial y^2}\rho(x,y,t) - (v_0^2\gamma_0\frac{\partial^2}{\partial x^2}\rho^2(x,y,t) - \\ -g\frac{\partial^2}{\partial x^2}\frac{\rho^2(x,y,t)}{\int dx'dy'\rho^2(x',y',t)}) \quad (16)$$

We generalize also the Schrodinger equation for this case and assume

$$i\hbar\phi_t(x^1,x^2,y^1.y^2)+\frac{\hbar^2}{2m}\Delta\phi(x^1,x^2,y^1.y^2)-$$

$$-[V_{eh}(x,y)-g\rho(x,y)]\phi(x^1,x^2,y^1.y^2)=0, \quad (17)$$

The adiabatic approximation is based on the following assumptions:

(i) The center of the exciton (e – h – pair) and the center of the soliton are located at the same place.

(ii) the exciton follows the moving soliton without delay.

similar as known from standard quantum mechanics we may go now to traveling center of mass coordinated and relative coordinates x, y and get finally the Schrodinger equation

$$i\hbar\phi_t(x,y,t)+\frac{\hbar^2}{2m}[\phi_{xx}+\phi_{yy}]+$$

$$+[g\rho(x,y,t)-V(x,y)]\phi(x,y,t)=0, \quad (18)$$

The wave function amplitude $\phi(x,y,t)$ may be considered as the limit of the amplitude of the coefficients $c_n(t)$ in the discrete description [15] . Note that the validity of the continuous approximation is restricted to small nonlinearities (small α,χ,γ_0). In spite of these known limitations we will use here the continuous theory for analytical estimates, as far as other analytical estimates are not available. Solutions of special interest to us are the so – called lump solitons, they are like moving hills. A special solution for the envelope of a lump-type soliton reads [21]:

$$\rho(x,y,t)=\rho_0\frac{[v_s y^2+3/v_s-(x-v_s t)^2]}{[v_s y^2+3/v_s+(x-v_s t)^2]^2} \quad (19)$$

Note that this special solution depends only on one parameter, the soliton velocity v_s . The compression density $\rho(x,v,t)$ is always positive around the center of the moving lump but has also negative parts at larger distance from the maximum. This is related to the property that the integral is zero

$$\int dxdy\rho(x,y,t)=0;\rho_0=\frac{v_s}{3}. \quad (20)$$

In figure 7 we represented the envelope of a lump soliton at two subsequent time instants. Such lump solutions we have found also numerically for Morse lattices [15, 21]

In parabolic approximation the density of a lump soliton may be represented as:

$$\rho(x,y,t)=\rho_0-\tfrac{1}{2}r_x x^2-\tfrac{1}{2}r_y y^2 \quad (21)$$

This way we get for the total effective potential acting on a n electron – hole pair moving in the field of a soliton:

$$V_{eh}^{eff}=V_{eh}(x,y)-g\rho(x,y)\phi(x^1,x^2,y^1.y^2)\simeq$$

$$\simeq V_{eh}(x,y)+\tfrac{1}{2}gr_x x^2+\tfrac{1}{2}gr_y y^2 \quad (22)$$

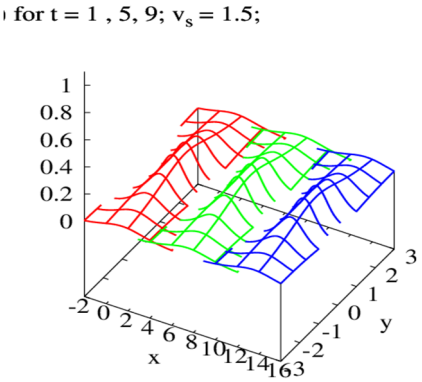

Figure 8 – Solution of the KP equation showing a traveling lump soliton at three successive time instants

5 Ionization equilibrium in bilayer plasmas and BEC condition

In our bilayer system, due to the existing attractive and repulsive forces, we may find different species and quasi-species as e.g.: electron, holes, solitone, solectrons, solholes, excitons, biexcitons, quasimolecules, etc.

At low densities the concentrations between different species are in chemical equilibrium. In the thermodynamic equilibrium we may describe the relations between the "elementary" particles / quasiparticles, the electrons, holes and solitons by mass action laws. Let us first describe the most important chemical equilibrium between electrons and holes. We will give a short derivation of the so-called Saha equation formalism for a binary Coulomb system with n_h positive charges (holes) and n_e negative charges (electrons) per cubic centimeter. The density of free e-h-atoms is denoted by n_0. The total density of charges is $n=n_e+n_h$. In the following we will use the plasma notations, i.e. we call the negative charges "electrons" and the positive charges simply "holes". We assume in he spirit of the ideas of Planck and Nernst a chemical

equilibrium between electrons, holes and atoms [2, 23].

$$e^- + h^+ \rightarrow a_0; \qquad \mu_e + \mu_h = \mu_0 \tag{23}$$

Here the $\mu_k = \partial F / \partial N_k$ (F – free energy) are the chemical potentials for the corresponding species, for the e-h-atoms we assume for non-degenerated "atoms" in ground state which is most probably assumed:

$$\mu_0 = k_B T \ln n_0 + k_B T \ln \lambda_0^3 - E_{0,0} \tag{24}$$

and for the charges including an ideal Boltymann contribution and an excess part stemming from degeneration effects and the charge-charge interactions:

$$\mu_e = \mu_e^{id} + \mu_e^{ex} + k_B T \ln n_e;$$

$$\mu_h = \mu_h^{id} + \mu_h^{ex} + k_B T \ln n_h. \tag{25}$$

The ideal Boltzmann terms contain the chemical constants which were fiorst expressed by Planck's constant in the pioneering work of Sackur and Tetrode:

$$\mu_e^{id} = +k_B T \ln \Lambda_e^3; \quad \mu_e^{id} = +k_B T \ln \Lambda_e^3;$$

$$\Lambda_k = h / \sqrt{2\pi m_k k_B T}. \tag{26}$$

From the condition of chemical equilibrium for the chemical potentials follows neglecting nonideality and nondegeneracy the so-called Saha formula:

$$\frac{n_a}{n_e n_h} = K(T) = \Lambda^3 \exp\left[\frac{-E_{0,0}}{k_B T}\right]; \qquad \Lambda = \frac{\Lambda_e \Lambda_h}{\Lambda_a}. \tag{27}$$

The length Λ_e, Λ_h is the de Broglie- wave length of electrons/holes having thermal momentum, n_e, n_h are the densities of free electrons and free holes. Free electrons are formed in chemical equilibrium with bound electrons and Planck's theory is applicable. The theory depends crucially on the ground state energy $E_{0,0}$. In the general case, the excited states have to be taken into account through the Planck-Brillouin-Larkin partition function and degeneracy and cahrge interaction throug standard approximations [2, 23]. Assuming as previously $d \sim 1$ nm and $\varepsilon \sim 2 - 10$, we arrive at bound state energies with an order of magnitude around 0.1 eV and find that the densities of the valley are located at $n \simeq 10^{12} cm^{-3}$ corresponding to weak doping and $n \simeq 10^{18} cm^{-3}$ corresponding to strong doping . We show the estimates for different temperatures in the region between $0.3 \cdot 200$ K and $0.8 \cdot 200$ K . In the region of low densities we observe temperature ionization and in the region of high densities we observe density ionization which is mainly due to the lack of space for exciton formation. Taking into account that an exciton, which is in principle like an hydrogen atom needs a space of at least a_B^{*3} to form bound state wave functions. Remember that the Bohr radius in a dielectric medium ($m*$ – effective relative mass of e-h pairs)

$$a_B^* = \varepsilon \frac{\hbar^2}{m^* e^2} \tag{28}$$

($m*$ – effective relative mass of e-h pairs). This may leaad to typical Bohr radii around $10^{-6} - 10^{-7}$ cm and therefore to maximal densities for the existence of excitons around $10^{18} - 10^{20} cm^{-3}$. It follows, that certain limit densities, which are typically around a doping of $10^{18} - 10^{20} cm^{-3}$ electrons and holes in the layers cannot be exceeded.

The interesting result is, that bosonic effects connected with excitons are to be expected only in a valley of intermediate densities and the bosonic region is rather narrow at higher temperatures.

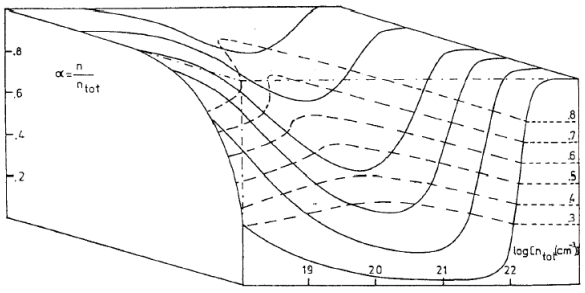

Figure 9 – Ionization equilibrium in bilayers in the region around 160 K (curve above) and 60 K (curve below) showing the region of electron-hole pairing. The electrons in the upper layer and the holes in the lower layer are within the valley mostly paired and behave like excitons. The valley of densities where the excitons are formed is shown which is located usually between $n \simeq 10^{12} cm^{-3}$ and $n \simeq 10^{18} cm^{-3}$ is shown in our example for a temperature region between 60 K and 160 K.

In principle we may expect also the formation of pairing of solectrons and solholes leading to molecule – like structures (biexcitons), however this is energetically not of any advantage [6]. For the region of lower temperatures where the particles may

be degenerated, the situation is more complicated and may be in some respect similar to electron – hole systems in semiconductors [6, 8, 22, 23] and in plasmas [2]

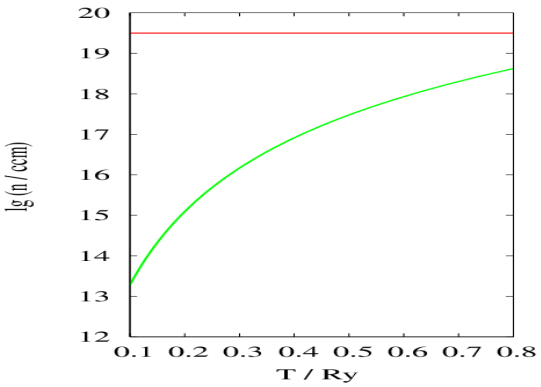

Figure 10 – The region of electron – hole pairs in the density – temperature plane. Formation of pairs (excitons) is expected inside the area formed by the green line, denoting temperatures where temperature ionization begins and the red line giving the high densities where the excitons are destroyed due to lack of space for forming bound state wave functions. The temperature is measured in units of the e-h- ground state energy $T{\sim}k_BT/E_{00}$.

Including Coulomb interactions and all degeneracy effects, the generalization of the Saha equation reads [2]

$$\frac{n_a}{n_e n_h} = \Lambda^3 \sigma_0(T) \exp[-\beta[\mu_e^{ex} + \mu_h^{ex} - \mu_0^{ex}]]. \quad (29)$$

where $\sigma_0(T)$ denotes the excitonic partition function to be calculated using the exciton bound state energies

$$\sigma_0 = \sum_{n_x,n_y} \exp[\beta E_{n_x,n_y}]. \quad (30)$$

The excess chemical potentials describe the Coulomb interaction and degeneracy effects The most important open question is in this connection, whether the densities of excitons provided by the chemical equilibrium are high enough to allow degeneration and BEC effects. The problem has been studied among others by Mahler and Kilimann for the exciton formation in semiconductors (see e.e [22, 23]). As well known, in the region of BEC holds for the Bose gas

$$\mu_0^{gas} = 0 \quad (31)$$

In combination with the condition of ionization equilibrium

$$\mu_e + \mu_h = \mu_0 and \mu_0 \simeq \mu_0^{gas} + E_{0,0} \quad (32)$$

We find as a first estimate for the existence of BEC effects similar as for semiconductors [22, 23] the condition

$$\mu_e + \mu_h \simeq E_{0,0} = 0 \quad (33)$$

6 Adiabatic approximations for solitonic excitations

So far we studied mostly systems in thermodynamic equilibrium assuming a continuous background. In some earlier works we studied the interaction of acoustic lattice soliton excitations in 2d – lattices to imbedded electrons, and found a form of electron *surfing* [12, 13, 14] including transport effects [15]. In particular we discussed applications to control effects [16]. Briefly speaking, the charges may be transported by lattice excitations. Since the dynamics of electrons and holes is much faster that the lattice dynamics, adiabatic approximations may be quite useful assuming that the charges follow instantaneously the mesoscopic changes in the lattice, as soliton excitations, breathers etc.

The adiabatic approximations which we developed in our work since 2009 [12] is a very simple tool to estimate the effects of thermal motion including the compression effects on polaron- and solectron – formation. The idea is quite simple. In the first approximation which is correct for fast electron dynamics in comparison to lattice dynamics, the local charge occupation of a lattice point n is given by a Boltzmann, Fermi- or Bose distribution based on the adiabatic quantum states. At small densities we may use the Boltzmann distribution

$$p_n = const \exp[-\beta \varepsilon_n] \quad (34)$$

Here the $epsilon_n$ are the local eigenvalues of the Hamilton matrix, which in adiabatic approximations are assumed to be a function of all coordinates of sites in the lattice. Following Gershgorins theorem, as shown in [12] what matters are only the the elements in some circle (the Gershgorin circle). In our case we need the positions inside some physical distance, say $1.5 sigma$ from given lattice point n. In a reasonable approximation the local eigenvalue is given by the mean

compression near to the lattice site n. Still easier is the description in the continuous approximation described above, at least restricting the studies to the parabolic approximation. In the continuous approximation the distribution in space is given by the adiabatic wave functions

$$n_0(x,z,t) = const \sum_n \exp[-\beta\varepsilon_n]|\psi_n(x,y)|^2 \quad (35)$$

However the levels and the wave functions are fully known only in the parabolic approximation, which howver gives at least a qualitative picture. What we need at the end are only the local compression which have to be calculated appropriately. An preliminary example calculated earlier for a one layer system is shown in figure 11. More precise calculations of the running compressions and the corresponding charge densities in two – layer systems are still to be done.

We studied here bilayers, consisting of two lattice layers in small distance. The coupling of electrons injected into one layer to holes injected into a second layer leads to the formation of electron-hole pairs which are bosons. Since the dynamics of electrons and holes is much faster that the lattice dynamics, we used adiabatic approximations. The idea is to assume that the charges follow instantaneously the mesoscopic changes in the lattice, as soliton excitations, breathers etc. The tool of adiabatic approximations has been developed in several of our works [12]. It is the appropriate and sufficiently simple tool to estimate the effects of thermal motion including the compression effects on polaron- and solectron – formation. This first approximation is correct if the electron dynamics is fast in comparison to lattice dynamics. Then the local charge occupation of a lattice point is given approximately by a Boltzmann, Fermi- or Bose distribution based on the adiabatic quantum states.

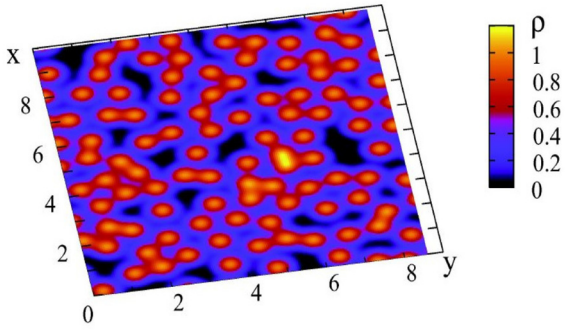

Figure 11 – Adiabatic approximation for the charge distribution in a heated system at $T = 0.2D$ taken from a preliminary calculation given in [12], with several locally percolating regions of high charge density.

7 Conclusions

So far we concentrated here on several thermodynamics and dynamic effects, as the Coulomb attraction between electrons and holes, the formation of electron – hole atoms and degeneration effect. Further we investigated the ionization equilibrium and the coupling to solitonic excitations.

Still to be studied are details on the control of the dynamics of pairs extending [16], transport phenomena extending [15], formation of bosonic electron – hole atoms at higher densities and, possible BE-condensation of e-h-atoms at very low temperatures/high densities [11, 3] .

Acknowledgement

The authors profited from contributions to SCCS-2017 in Kiel [3] and from further advice provided by M. Bonitz (Kiel), G. Röpke (Rostock) and V. Filinov (Moscow).

References

1. W. Ebeling. Max Planck and Albrecht Unsöld on plasma partition functions and lowering of ionization energy // Contribution to SCCS-2017 Kiel, Contr. Plasma Phys. – 2017 –Vol. 57.P.441 – 451.

2. W. Ebeling, V.E. Fortov, V. Filinov. Quantum statistics of dense gases and nonideal plasmas. Springer Berlin – Heidelberg – 2017– , Russ. transl. in preparation.

3. A. Perali, S. Conti, F. M. Peeters, N. Neilson. Multicomponent electron-hole superfluidity and the BCS-BEC crossover in double bilayer graphene // Contribution to SCCS-2017, Kiel, August 2017, Contr. Plasma Phys.– 2017– Vol.57. –P 1.

4. P. Ludwig, A.V. Filinov, M. Bonitz, Yu.E. Lozovik. Strongly correlated indirect excitons in quantum wells in high electric fields // Contr. Plasma Phys. – 2003. – Vol.43. – P.285 – 289.

5. J. Schleede, A. Filinov, M. Bonitz, H. Fehske. Phase diagram of bilayer electron-hole plasmas // Contr. Plasma Phys. – 2012 – Vol.52.– P.10.

6. Y. E. Lozovik, V. I. Yudson. A new mechanism for superconductivity: pairing between spatially separated electrons and holes // JETP Lett. – 1975 – Vol.22. – P. 274.

7. S. Shevchenko, J. Sov. Theory of superconductivity of systems with pairing of spatially separated electrons and holes // Low Temp. Phys .– 1976 – Vol.2. –P.1.

8. Yu. E. Lozovik, O.L. Berman. Superfluidity of indirect magnetoexcitons in coupled quantum wells // JETP – 1996.– Vol.64. – P.526.

9. D. K. Efimkin, V. A. Kulbachinskii, Yu. E. Lozovik, Influence of disorder on electron-hole pairing in graphene bilayer// JETP Letters– 2011**.** – Vol. 93.– P. 219 – 222.

10. A. Perali, D. Neilson, A. R. Hamilton. High-Temperature superfluidity in double-bilayer graphene // Phys. Rev. Lett. – 2013. – Vol. 110**.** –P**.**146803.

11. S. Conti, A. Perali, F.M. Peeters, D. Neilson. Multicomponent electron-hole superfluidity and the BCS-BEC crossover in double bilayer graphene.// arXiv: 1706.076.07672.

12. W. Ebeling, M.G. Velarde, A.P. Chetverikov, Bound states of electrons with soliton-like excitations in thermal systems – adiabatic approximations // Cond. Mat. Phys. – 2009**.** – Vol. 12. – P.633 – 645.

13. A.P. Chetverikov, W. Ebeling, M.G. Velarde. Thermal solitons and solectrons in 1d anharmonic lattices up to physiological temperatures // Eur. Phys. J. B – 2009. – Vol.70.– P.117.

14. A.P. Chetverikov, W. Ebeling, G. Röpke, M.G. Velarde. Hopping transport and stochastic dynamics of electrons in plasma layers // Contr. Plasma Phys.– 2011 – Vol. 51.– P**.**814–829.

15. A.P. Chetverikov, W. Ebeling, G. Röpke, M.G. Velarde. Electron transport mediated by nonlinear excitations in atomic layers // Eur. Phys. J. B – 2012. – Vol.70.- P.117.

16. A.P. Chetverikov, W. Ebeling, E. Schöll, M.G. Velarde. Excitation of solitons in hexagonal lattices and ways of controlling electron transport // Int. J. of Dynamics and Control. – 2018. –Vol. 6. –P. 1376.

17. A.K. Geim,, I.V. Grigorievna. Van der Waals heterostructures // Nature. -2013. –Vol. 499.– P.419.

18. K. Lee, J. Xue, D. C. Dillen, K. Watanabe, T. Taniguchi, E. Tutuc. Giant frictional drag in double bilayer graphene heterostructures // Phys. Rev. Lett. –2016. – Vol.117. P.046803.

19. J. Li, T. Taguchi, K. Watanabe, J. Hone, A. Levchenko, C. Dean. Transport properties of an electron-hole bilayer/superconductor hybrid junction // PRL. – 2016. –Vol.117.– P.046802.

20. A. Chetverikov, W. Ebeling, G. Röpke, M.G. Velarde. Anharmonic excitations, time correlations and electric conductivity // Contrib. Plasma Phys. – 2007. –Vol.47.– P.465 .

21. A. Chetverikov, W. Ebeling, M.G. Velarde. High electrical conductivity in nonlinear model lattice crystals mediated by thermal excitation of solectrons // Nonlinear Wave Motion. – 2014. – Vol. 87. – P.153.

22. G. Mahler. Theory of the phase diagram of highly excited semiconductorsc // Phys. Rev. B. – 1975. – Vol.11. – P.4050

23. W. Ebeling, W'D. Kraeft, D. Kremp, K. Kilimann. Hopping conductivity in ordered and disordered solids (I) // Phys. stat. sol. B. – 1976. –Vol. 78. – P. 241.

IRSTI 44.41.35; 59.71.35

Automated system of smart-windows using solar cells

A.G. Yakunin

Polzunov Altai State Technical University, 46 Lenina avenue, 656038, Barnaul, Russian Federation
e-mail: yakunin@agtu.secna.ru

The smart window management system uses the Arduino controller to automate the device working on renewable energy sources. Possibility of using the obtained solutions for the design of wall-mounted power plants using solar energy is presented. Solar panels can be used not only for their direct purpose (generation of electricity), but also as a household appliance with a set of various consumer functions. Mounting of such device on the facade of residential and office buildings modernizes the architectural view and contributes to the improvement of the cities environment. Using the Arduino controller and its accompanying circuit boards will help to solve the problem of digitalization of the building windows and connect solar cell based devices to the Internet via a standard Wi-Fi router. Such actions will ensure the broad demand for such devices among residents of cities, which will result in a high degree of commercialization of the resulted work.

Key words: renewable energy sources, arduino, automation, solar cells, sustainable development/
PACS numbers: 88.05.Lg, 88.05.Sv

1 Introduction

The two most important obstacles to the development of renewable energy in Kazakhstan are low profitability of renewable energy sources (RES) and developed traditional energy with redundant provision with natural resources. Perhaps, the only stimulus to develop renewable energy is a large-scale environmental problem, which is still perceived only at the national and international level and is not perceived by the average person. At the same time, due to of automobile emissions, traditional power plant emissions and dust threatening the health of residents, so the ecological situation in cities, in particular Almaty, is getting worse. [1-4] This determines the needs to carry out the active cleaning of the air and thereby improving the comfort and quality of life. Part of this time-consuming work can take on the elements and components of renewable energy sources. With regard to the first thing, the government introduced several important measures to reduce the operating costs of renewable energy producers, including favorable access to the grid, priority in providing land and customs privileges for the supply of materials and equipment [5-10]. Among the renewable energy sources of Kazakhstan, solar power plants occupy a special place, since most areas like in Iran or Chine, have a large solar exposition [11-16]. However, the low profitability of solar panels, high cost of mounting and related equipment, in addition to the need to delve into the physics and technological nuances of operating solar panels, reduce their appeal to consumers. One way to make solar cells more cost-effective is to use their non-target properties with the ability to perform additional consumer functions like an air conditioner, a dust collector or a heater, with mandatory automation of the management of these functions To automate the device on renewable energy sources, one can actively use ARDUINO units [17-20].

2 Results and Discussion

The most acceptable way to automate the device as an element of a smart window is to use the Arduino controller and its associated framing applications. In addition to the automation of processes, the capabilities of this device allow to connect an automated design to the Internet via a standard Wi-Fi router or application on the mobile phone. Relevance of the work is increasing, if we take into account that production of solar batteries from local raw materials is started in Kazakhstan and in the next five years there will be a problem of cost-effective use of the products of factories located in Astana, Ushtobe and Ust-Kamenogorsk. Manufacturing of construction,

the general scheme of which is presented in Figure 1, will mainly be of an assembling – like and can be carried out at a variety of enterprises and workshops in Kazakhstan with available power tools.

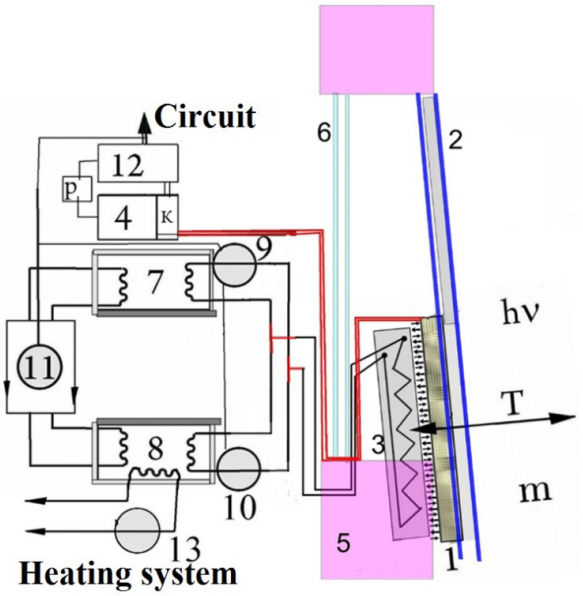

1 – solar cell; 2 – frame with a film; 3 – heat exchanger; 4 – electric accumulator; 5 – window sill; 6 – window; 7 – cold accumulator – radiator; 8 – heat accumulator-radiator; 9 – circulating pump of the cold coolant circuit; 10 – circulation pump of the hot coolant circuit; 11 – compressor of the heat pump; 12 – inverter and power supply of lighting devices.

Figure 1 – Functional diagram of an automated smart window system with solar cells

Winter air conditioner variant allows combining thermal energy from solar radiation and atmosphere and heat the room. In other words, we can combine central heating with air conditioning system of the room and the accumulation of heat and cold. The solar panel will play a role of additional outdoor radiator of heat exchange with atmosphere for a heating and cooling system (room air conditioner). The variant of the summer air conditioner allows accumulating the cold at night and cooling the room in the afternoon.

In situations where it is not necessary to perform the listed functions, the device allows accumulating electricity, heat and cold for emergencies in the room. Such accumulated electricity could be used for evening lighting of other rooms, thereby smoothing peak overloads in the city network.

Figure 2 shows a functional diagram of such type of the device. When the sun illuminates the solar panel 1, it generates electricity, which is stored in the battery 7.

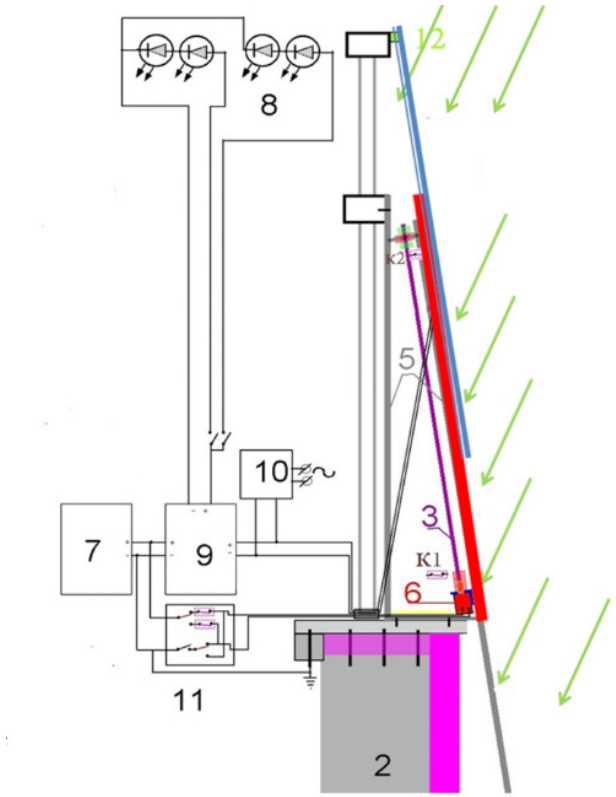

1 – solar panel with reflective film; 2 – wall of the house; 3 – moveable pin; 4 – plate with a protective film; 5 – corners; 6 – motor-reducer, 7 – battery; 8 – LED emitters; 9 – battery charge controller; 10 – battery charger; 11 – commutator power supply of the motor-reducer; 12 – heat insulating and soundproofing layers

Figure 2 – Functional diagram of an automated smart-window system in the mode of room lighting regulation and sound insulation

Two-folded window is equipped with two panels. The panels are mounted moveable to the corners, which are screwed to the wall, the windowsill and the window frame. All installation is carried out from the room, which makes the device usable and easy to use. The solar stream penetrating into the room through the window can be adjusted or overlapped with the solar panel [2].

The radiation flux and sound waves *hv*, dust *m*, atmospheric heat and cold flows *T* are periodically present in the external environment in front of the window. With these elements, the home appliance can operate to perform programmed consumer functions. If solar radiation flux *hv*, is presented, the device can accumulate photovoltaic energy directly in the accumulator 4 and we can use this energy at any time to power electric appliances, preferably with illumination. However, if the radiation flux into the room needs to be reduced, it can be covered with an improvised curtain, the role of which is performed by

the solar panel 1, which is opaque to radiation and absorbs it. Reversible motor reducer raise or lower the solar panel by using a 1.5-meter pin with metric thread M10. The motor reducer connects to the electric battery and consumes its energy. At night, the consumer may want to reduce the radiation flow *hv* from illumination of the street, in which case the solar panel should cover the maximum window area. If, the film frame with the film itself is extended at the same time with a screening sound, then the level of sound waves penetrating into the room from the street will decrease significantly. This helps to improve the insulation and sound insulation of the room with windows, but also it increases the insulation of the room. Electrically charged dielectric film could help to forcibly remove dust and fumes *m* from the atmosphere of the ambient air of the street and therefore dust and fumes *m* don't penetrates into the room. Periodically, the film is washed from the dust by moving towards the stationary moistened sweeper. Dust can be collected in the dust collector.

Arduino is used to create electronic devices with the ability to receive signals from various digital and analog sensors that can be connected to the plate, and used to control various actuators as well. The environment of the developed program with all sceneries is available for download and free of charge [3]. Controller, sensors, actuators, expansion plates, programs for all kinds of combinations are very cheap and available anywhere in the world. Thus, almost any smart system can be assembled as a Lego children's designer from ready-made and accessible blocks.

There are also recoverable fuses that used to protect the USB port of the computer from short circuits and overloads in the Arduino plate, which alas, occur not so rarely as desired. Despite the fact that most computers have their own protection (the so-called UPS), such fuses provide an additional level of protection for the microprocessor. If a current of more than 500 mA is consumed from the USB port, this fuse will automatically break the connection until the cause of the short circuit or overload is eliminated.

For this reason, a cheap and affordable Arduino controller is selected for automatic control of solar panels that hung out of the window and perform many non-core consumer functions. The logic of controlling the smart device, which can be located on the window or outside the window, including the movable front panels is very complicated. The obtained results will have a significant impact on the development of science and technology in the field of solar energy and ecology in Kazakhstan, so the results of many scientific works in this and related fields will be applied. Application of the results into production will ensure the sales market of the plants in Kazakhstan and create new jobs.

3 Conclusion

The solar panels mounted on the facades of buildings makes it possible to use the consumer functions that is non-core for them, which increase the profitability of renewable energy devices. The mounting the devices with solar cell on the facades of buildings will improve the esthetic view of buildings and contribute to the improvement of the ecological situation in the city. Automation management and usage of several consumer demands in the simultaneously smart and simple designed household appliance will increase the demand for it in a broad consumer market and could be sold to individuals at retail as a household device. Combination of several consumer properties in a photoelectric generator of energy for urban conditions is justified.

Acknowledgements

This work was carried out with financial support of Ministry of Education and Science with grant AP05131673.

References

1. T.E. Khakimzhanov, A.S. Begimbetova Influence of motor transport emissions on the ecological state // Bulletin of KazNITI.-2010. -Vol.80, №. 4. P. 1-5
2. Banzi M. and Shiloh M. Maker Getting Started with Arduino. Sebastopol, CA, USA: – Maker Media, Inc, 2015, P. 262
3. Al-Tameemi M.A., Chukin V.V. Global water cycle and solar activity variations // J Atmos Sol Terr Phys, – 2016 –Vol. 142 № 55 – P. 9-19.
4. E. Kabira, P. Kumarb, S. Kumarc, A. A. Adelodund, K. Kim Solar energy: Potential and future prospects // Renewable and Sustainable Energy Reviews.- 2018. – Vol. 82, – P. 894 – 900.

5. E. Bellini Kazakhstan's government announces 12 MW large-scale solar project https://www.pv-magazine.com/2017/05/31/kazakhstans-government-announces-12-mw-large-scale-solar-project/ May 31, 2017

6. L. Mikhailov, S. Mikhailova, G.Ismailova, G. Yar-Muhamedova, S. Sokolov, Development of energy devices based on photovoltaic panels with extra consumer properties // Mediterranean Green Buildings and Renewable Energy: Selected Papers from the World Renewable Energy Network's Med Green Forum, Springer, Cham. 2017. – P 609-617

7. A.V. Moskvin A new handbook of chemist and technologist. General joints. Structure of the substance // Saint-Petersburg.:Professional. – 2006. – P. 1464.

8. S.M. Besarati, R.V. Padilla, D.Y. Goswami, E. Stefanakos The potential of harnessing solar radiation in Iran: generating solar maps and viability study of PV power plants // Renew Energy -2013;- Vol. 53 № 193 – P. 9-19

9. Q. Hang, Z. Jun, Y. Xiao, C. Junkui Prospect of concentrating solar power in China-the sustainable future // Renew Sustain Energy Rev. – 2007, -Vol. 12, № 9, –P. 2505–2514.

10. S. Seddegh, X. Wang, A.D. Henderson, Z. Xing Solar domestic hot water systems // Renewable and Sustainable Energy Reviews. – 2018- Vol. 82, – P. 894–900.

11. M.R. Islam, K. Sumathy, S.U. Khan Solar thermal systems and their market trends // Renew Sustain Energy Rev. – 2013, -Vol.17, – P.1-25.

12. U. Sommer Programming of microcontroller boards Arduino / Freeduino, St. Petersburg: – BHV-Petersburg 2012, C – 236.

13. F. Perea, Arduino Essentials, Boston:-Packt Publishing,- 2015, P – 376

14. Sun D., Wang L. Research on heat transfer performance of passive solar collector storage wall system with phase change materials // Energy Build – 2016, -Vol 119, -P. 183-201.

15. L. V. Mikhailov, S. L. Mikhailov, G. A. Ismayilov, M.Zh. Kuatov, A.A. Appasova, A.B. Otarov, D.R. Mamishev "The problem of using photoelectrical panels on the fasad of urban buildings"// PEOS Journal, – 2016. – Vol. 2. P. 116-121

16. L. V. Mikhailov, M.Zh. Kuatov, A.B. Otarov, D.R. Mamishov, S.L. Lee "The development of a renewable source of energy with additional subsidiary functions // Multicore processes, parallel programming, flex, signal processing systems, – 2016, №6. – P. 226-229

17. E.A. Kats Solnechnaya eneggetika: yspexi, expectations, challenges / Energiya: Ekonomika. Technika: Ecology. -2013. –Vol.5. – P. 2-9.

18. B.V. Lukutin Reinforcing sources of electricity // Bulliten of Tomsp potitech univer sity, – 2008. 366 p.

19. D.A. Tsygankov Analysis of the temp and the development of the development of the solar photoregeneracy // The monthly naychny zhurnal "Innovative Nayka", – 2015, №8 -P.38-41.

20. A. Luke. Development of the electro-optic solar power system is inoperable // Ecology and life. – 2012 – Vol. 133, №. 12 – P. 18-19.

IRSTI 44.09.29

Self-regulated hydrogen generation with the use of nano-powders: application for portable fuel cells

A. Pastushenko[1,#], S. Litvinenko[1], V. Lysenko[2,*] and V. Skryshevsky[1]

[1]*Institute of High Technologies, National Taras Shevchenko University of Kyiv, Volodymyrs'ka 64, Kyiv 01601, Ukraine*
[2]*Lyon Institute of Nanotechnologies (INL), CNRS UMR-5270, INSA de Lyon, 7 av. Jean Capelle, Bat. Blaise Pascal, Villeurbanne, F-69621, France*
[#]*Current affiliation: Apollon Solar SAS, 66 Course Charlemagne, 69002 Lyon, France*
[*]*e-mail: vladimir.lysenko@insa-lyon.fr*

Self-regulated hydrogen production at room temperature and atmosphere pressure is described in details. Basic idea of our approach is based on a precise auto-tuning of the oxidizing aqueous solution arrival onto hydrogenated silicon or aluminum nano-powders. The used self-regulation principle is completely passive e.g. neither electrical power sources, no regulating electronics are required. The system functioning was simulated numerically and checked experimentally. The numerical simulation allowed definition of the main optimal parameters of the working system (pressure, capillary tube diameter, tank volumes) and an experimental prototype based on the simulated results was built and used for hydrogen supplying to a portable PaxiTech® fuel cell.

Key words: hydrogen generation, nano-powders, fuel cells.
PACS numbers: 81.05.Rm, 81.07.Wx, 88.30.-k.

1 Introduction

Hydrogen energy field is rapidly developing, presenting hydrogen as a new friendly-environmental energy carrier. However, to ensure wide usage of hydrogen, energy density of new hydrogen-based energy sources have to exceed the value of 180-200 W·h/kg which is the maximal level for traditional power sources such based on lithium-ion batteries. Thus, elaboration of new efficient ways for hydrogen production and storage is of the highest importance.

Traditional hydrogen storage in high pressure vessels is not applicable for small portable devices due to safety reasons. One of the alternative ways is storing hydrogen in capillary arrays [1, 2]. However, leakage of H_2 through thin capillary walls is the main disadvantage of this technological approach. Another solution to store hydrogen is the use of zeolites [3] with hydrogen mass content 1-2 % at 77 K and 1.6 MPa. Metal hydrides [4] seem to be also perspective candidates for portable and reversible hydrogen storage with relatively high mass content up to 7.6%. However, quite high temperatures are required for hydrogen desorption. In addition, desorption kinetics should be faster and there should be more number of cycles. Hydrolysis of metal hydrides overcomes some of these problems, but it is not reversible. Application of the hydrolysis for large automotive devices have been reported [5]. Hydrogen generation by solid Co-P catalyst from water solution of NH_3BH_3 have been also discribed [6]. The solid catalyst is quite attractive because of its constant H_2 production rate.

Hydrogen generation based on corrosion of light metals in water solutions is an interesting alternative for hydrogen sources. In particular, Al is probably the most adequate metal due to its high electron density and oxidation potential. However, the problem related to passivation of Al due to formation of $Al(OH)_3$ inhibiting H_2 formation remains unsolved. Thus, for generation of H_2 from water, using of Al powder and alkaline solutions are rather needed [7].

Porous silicon (PS) nanostructures can be conceived as solid-state hydrogen reservoir since its specific surface is almost totally covered by $Si\text{-}H_X$ bonds [8-18]. Theoretical maximum of the hydrogen content is 3.44 mass% for SiH, 6.66 mass% for SiH_2 and 9.67 mass% for SiH_3 species [13]. Maximal

quantity of hydrogen extracted from this kind of nanomaterials due to thermal annealing is about 60 mmol(H) per gram of PS (~6 mass%). This corresponds to about 1.8 of the H/Si ratio [9]. H_2 can be also produced from the PS at room temperature due to its oxidation in aqueous solutions. Thus, practical H_2 output resulted from the reaction with water is 2-3 times larger because water dissociation also provides two additional molecules of hydrogen [8].

A bottleneck in practical applications of portable fuel cells is perfectly controllable extraction of hydrogen from a tanker. While a portable device is switched on and consumes electrical power from a fuel cell, hydrogen must be generated in a reactor chamber. The evolution of hydrogen must be automatically stopped after the electrical consumer switching off. For example, a self-regulating hydrogen generator for micro fuel cells was earlier conceived [20]. The device consists of a hydride reactor and a water reservoir separated by a regulating valve. The latter is connected to the water reservoir and contains a movable membrane with holes. Water diffuses toward the hydride reactor due to capillary forces in the pores of the membrane. After reduction of hydrogen consumption, the gas pressure builds up inside the hydride reactor and provokes deflection of the membrane closing the water regulator valve. Maximum electrical power delivered by this device was measured to be 2.4 mW/cm^2 (8 mA/cm^2 at 0.3 V). However, the maximum limit power of a PEM fuel cell is about 210 mW/cm^2 (700 mA/cm^2 at 0.3 V). Comparing the systames described in Refs. [20] and [5], one can see a huge difference in power values. In Ref. [5], the authors work with water flows and control it electronically. In Ref. [20], the water vapors generate small power and any electrical control would dramatically decrease the total efficiency of the hydrogen generator.

In this paper, to control hydrogen production with the use of Al or PS nanopowders, a drop-by-drop approach based on an original double-tank hydrogen cartridge is described. For this approach, no active electrical control is necessary due to a self-regulating mechanism. Our cartridge can automatically stop production of hydrogen when it is not consumed by a fuel cell. The first tank of the cartridge contains a liquid oxidizer and the second one – PS or Al nanopowder. The tanks are connected via a capillary tube. The self-regulation mechanism is realized due to the dynamical variation of pressure difference between the tanks. If the pressure difference exceeds capillary pressure, a drop of the liquid oxidizing reagent falls down from the first to the second tank and reacts with the nanopowder. It leads to increase of the hydrogen pressure in the second chamber and, thus, decreasing the pressure difference. If the pressure difference is less than the capillary pressure, no oxidizer falls down and the system is in a stand-by state and waits for the hydrogen consumption by a fuel cell to decrease the hydrogen pressure in the second tank and, consequently, to increase the pressure difference. Numerical analysis of the cartridge functioning was performed and optimal parameters have been found. A working prototype of the cartridge was constructed and tested with a PaxiTech® fuel cell.

2 Double-tank cartridge for hydrogen supply

To ensure a self-regulating hydrogen production, a principle of on-demand supplying of reactants can be applied. A scheme of our hydrogen cartridge is shown in Figure 1. The cartridge consists of two tanks interconnected with a capillary tube. An upper tank contains pressurized air chamber at pressure p_1 slightly higher then the atmospheric pressure. The reaction between an oxidizer and PS or Al nanopowders takes place in the lower tank in which the generated hydrogen ensures a pressure value p_2. Diameter of the capillary tube should be small enough to ensure capillary phenomena as well as to maintain an equilibrium when pressure difference ($p_1 - p_2$) between the both tanks is less than the capillary pressure. Thus, it is possible to stop dropping when the final pressure difference due to the hydrogen generation becomes less than the capillary pressure and this is achieved without using of any valve. This is the first major advantage of our cartridge. Using of the capillary forces allows establishing of much more precise hydrogen generation rates compared to the use of valves and continuous water flows.

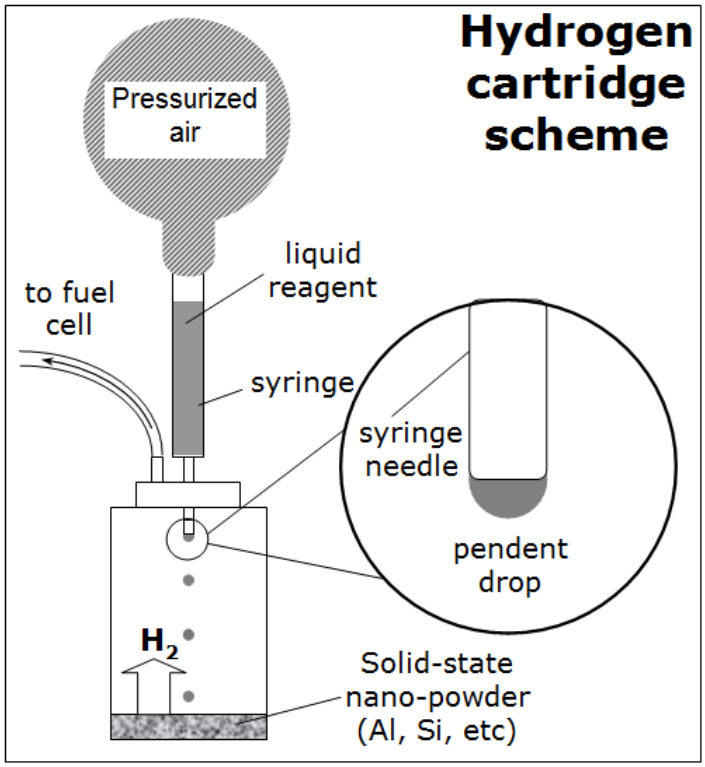

Figure 1 - Scheme of the double-tank cartridge for hydrogen generation with the use of Al or PS nanopowders

The first oxidizing reactant (water/catalyst or liquid alkaline solution) is spatially separated from another reactant (solid-state PS or Al nanopowder). Reaction chamber (lower tank with powder) has hydrogen outlet which is connected to a fuel cell. The corresponding chemical reactions between the water-based oxidizers and nanopowders are the follows:

in the case of PS: $$SiH_X + Y \cdot H_2O \xrightarrow{catalyst} SiO_Y + \left(Y + X/2\right) \cdot H_2\uparrow \quad (1)$$

in the case of Al powder: $$Al + NaOH + 3H_2O \longrightarrow Na\left[Al(OH)_4\right] + 3/2\, H_2\uparrow \quad (2)$$

Let's calculate the maximum possible gravimetric energy density for the reactions (1) and (2). In the reaction (1), we assume X=2, Y=2, which correspond to the case of fresh and completely hydrogenated nano-porous silicon. The product of the reaction (1) is silica gel keeping physically absorbed water. Let's assume that 1 mol of SiO_2 keeps 1.5 mol of water. Thus, 1 mol of SiH_2 (30 g) needs 3.5 mol of water (63 g), and it gives 3 mol of hydrogen. Mass of the used catalyst (NH_3, for example) comes in trace quantities which can be neglected [8]. Assuming that efficiency of a standard PEM fuel cell is about 50 % [21], electrical energy value which can be obtained from such reaction is 99 W·h. Thus, the corresponding gravimetric energy density is 99 W·h/(30g+63g) = 1054 W·h/kg, which is motre than 5 times larger than the energy density provided by traditional Li-ion batteries.

For the reaction with aluminum powder (2), we obtain: 1 mol of Al (27 g) reacts with 3 mol of water (54 g) and 1 mol of NaOH (40 g), and it gives 1.5 mol of hydrogen. Thus, corresponding electrical energy value is 49 W·h, and the maximum energy density is: 49 W·h/(27g+54g+40g) = 405 W·h/kg.

3 Theoretical description

Now, functional behavior of our hydrogen cartridge will be theoretically described. First of all, let the pressure difference p_1-p_2 between the two tanks be larger than the capillary pressure. Due to the pressure difference, the volume of the drop at the capillary edge starts to increase. The oxidizer flows through a constant circular cross-section of the capillary with a length, which is substantially longer than the capillary diameter. Kinetics of the drop growth can be described by Poiseuille formula [22] which is valid for the laminar, viscous and incompressible flows:

$$\frac{dV_d}{dt} = \frac{\pi r^4}{8\eta l}\left(p_1 - \frac{2\alpha}{r} Cos\theta - p_2 \right), \qquad (3)$$

where: V_d is the drop volume, η is the viscosity of the liquid, l is the capillary length, θ is the wetting angle (see Figure 2).

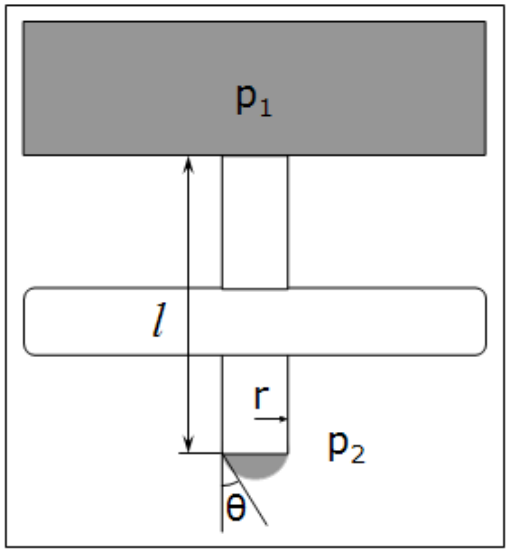

Figure 2 – Characteristical parameters of the cartridge system

The drop falls down when the capillary tension can not compensate the weight of the drop and the pressure difference. The volume of the fallen drop $V_d^{\max}$ can be calculated from the following expression:

$$g\rho V_d^{\max} = \alpha 2\pi r \qquad (4)$$

where: g is the gravitation constant, ρ is the density of the liquid, α is the coefficient of capillary tension and r is the capillary radius.

The total volume of the water in the reaction chamber V_w relates to the number N of hydrogen molecules produced per unit of time:

$$\frac{dN}{dt} = k_r V_w \qquad (5)$$

where k_r is the reaction velocity defined as the number of hydrogen molecules produced per unit of time and per unit of water volume. This expression can be applied if the water volume is significantly less than volume of another reactant (nanopowder, in our case). Reaction velocity depends on the temperature, concentration of the catalyst or alkali, and size of powder particles.

Due to the oxidizer consumption, decrease of its volume corresponds directly to the increase of the hydrogen molecules according t the following relation:

$$dV_w = \frac{\mu}{nN_A\rho} dN \qquad (6)$$

where: N_A is the Avogadro constant, μ is the oxidizer's molar mass, n is the stoichiometric relation between the oxidizer and hydrogen.

The equations written above can be solved numerically. Thus, pressure of hydrogen in the reaction chamber can be calculated as a function of time. Optimal capillary radius and reaction chamber volume were determined from the numerical calculations.

4 Simulation results

Functioning behavior of the cartridge system has been simulated with the use of the theoretical considerations described above. Two working modes can be defined: (i) steady state mode (Figure 3a) and (ii) dynamic mode (Figure 3b). The steady state mode can be realized with certain cartridge parameters and in absence of hydrogen consumption. In this functioning mode (when the output valve is closed), hydrogen pressure in the reaction chamber increases up to a saturation level which can be kept for a long time. It means that reaction is fully completed and there is no water

supplying into the reaction chamber. As for the dynamic mode, it is realized when the hydrogen output is opened. It is characterized by periodic drop fallings. In this case, the reaction is supported by new falling drops and hydrogen is generated continuously.

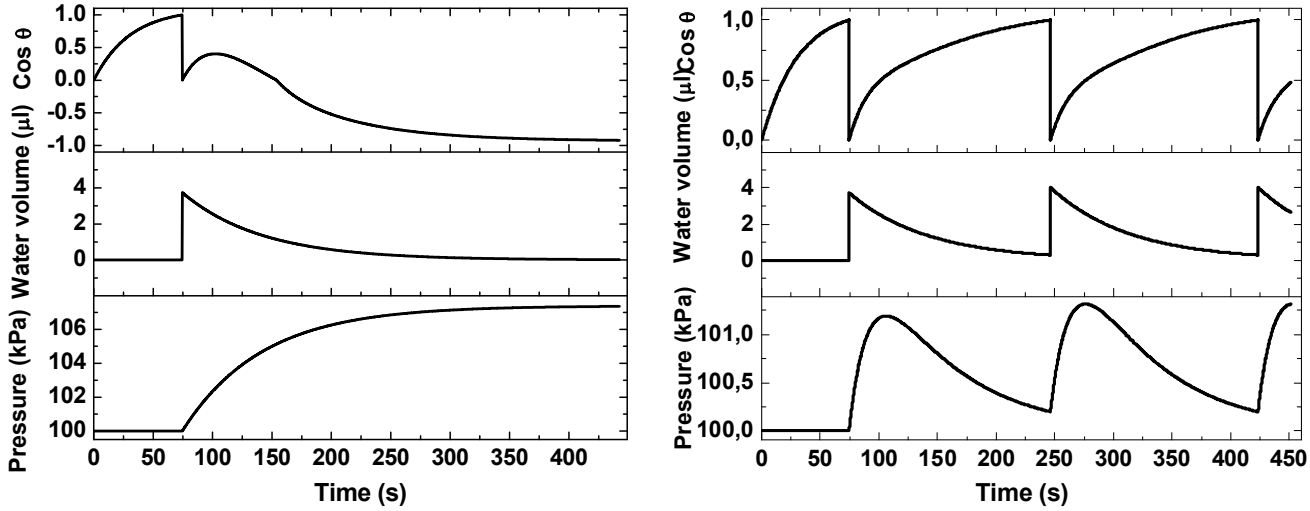

(a) (b)

Figure 3 - (a) Steady state and (b) dynamic modes of hydrogen generation in the cartridge system

The simulation was carried out at p_1=*104 kPa*. At the beginning, p_2 was assumed to be equal to 100 kPa. The difference of 4 kPa is slightly larger than the capillary pressure (3600 Pa):

$$\frac{2\alpha}{r} = \frac{2 \cdot 72\,{}^{mN}/_{m}}{40\mu m} = 3600Pa \qquad (7)$$

At these initial conditions the first drop can fall. For this simulation, the capillary tension of water and the capillary radius were used to be 72 mN/m and 40 μm, respectively. After the first drop falling, the pressure difference p_1-p_2 decreases due to the production of hydrogen. It should be smaller than capillary pressure to achieve a steady-state mode. Taking into account that the drop volume increases according to the evolved hydrogen pressure, and the hydrogen evolution has exponential character, this problem can not be solved analytically due to the transcendental equation. Thus, a numerical solution has been found. The cosine of the wetting angle was calculated as:

$$Cos\theta = \frac{V_d}{V_d^{\max}} \qquad (8)$$

As one can see in figure 3a, the cosine of wetting angle increases until falling of the first drop. After, the cosine becomes equal to zero and continues to increase. The water volume kinetics in the reaction chamber is also shown in Figure 3a. Before the drop falling, the water volume in the second chamber is equal to zero. Right after the drop falling, the water volume is equal to the drop volume. Due to the water consumption during the chemical reaction of the nanopowder oxidation, the water volume in the reaction chamber progressively decreases to zero. The water vapor is neglected in this simulation. Generation of hydrogen leads to the increase of pressure in the reaction chamber. In our case, the pressure in the reaction chamber increases up to a level which is larger than the pressure in the chamber with pressurized air (104 kPa). As a result, the drop is pushed back in the needle and a bubble is formed. This is represented by the negative value of the cosine of wetting angle. Since the produced hydrogen is not consumed, the steady-state regime is established.

A different behavior can be observed when the hydrogen output is opened (see Figure 3b). The hydrogen output was simulated as release of the gas in atmosphere through a specially designed outlet.

Hence, hydrogen flow is proportional to a difference of the pressures in the reaction chamber and atmosphere. Variation of cosine of the wetting angle from 1 to 0 corresponds to the subsequent drop fallings. The water amount in the second chamber decreases due to the chemical reaction and increases when the subsequent drop falls. Hydrogen pressure increases when the fallen drop provoke reaction of the nanopowder oxidation and decreases when the output hydrogen flow is larger than the hydrogen generation velocity. Thus, the pressure oscillations are observed. Oscillations of the hydrogen flow rate are present as well. In general, the hydrogen flow rate can be smoothed by choice of appropriate system parameters.

As follows from figure 3, the cartridge can be switched from a steady state mode to hydrogen release mode and vice versa by opening/locking the hydrogen outlet. It ensures a self-regulating reaction determined by hydrogen consumption by a fuel cell.

5 Experimental measurements

All the experiments described below have been carried out on a working cartridge prototype using the chemical reaction (2) between aluminum nanopowder and alkaline solution. Rubber balloon (100 ml in volume) was used as the first chamber with pressurized air. A glass container (150 ml in volume) with a hard rubber cover was used as the reaction chamber. Small needle was used as an input needle for the liquid oxidizing reagent, and 75 μm needle radius was found to be suitable for production of necessary hydrogen flow. The output needle has a larger diameter to ensure quick hydrogen delivery to a fuel cell. Before starting the experiments with a fuel cell, the reactor chamber, connecting pipes and fuel cell have been cleaned with nitrogen or argon.

Kinetics of the drop fallings with free release of generated hydrogen in atmosphere is shown in Figure 4. The pressure in the reaction chamber was by 1050 Pa above the atmospheric pressure during the experiment. Every point in Figure 4 correlates the total number of the fallen drops and time of each drop falling. A perfect linear fit of the obtained plot can be performed. If the solid reagent (nanopowder) runs out, the frequency of the drop fallings increases in order maintain hydrogen pressure at a constant level: larger amount of water is thus required. The experiment was carried out only for 700 s, but at a larger amount of the reaction compounds, or lower hydrogen consumption, the working time can be extended.

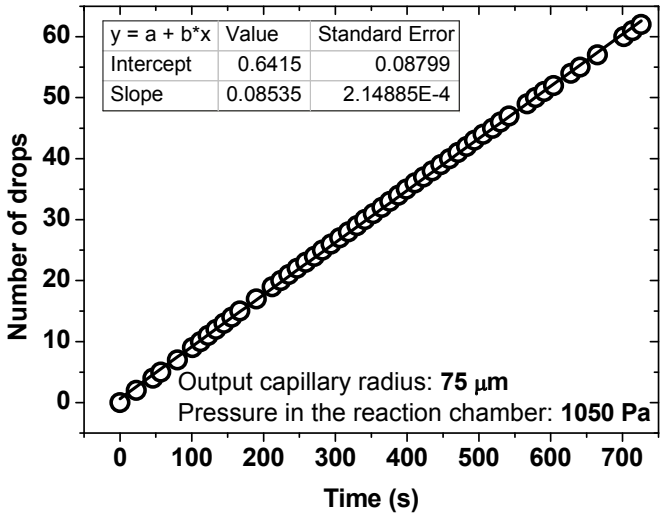

Figure 4 – Number of the fallen drops of the liquid reagent as function of time

Electrical characteristics of the used fuel cell are presented in Figure 5. Measurements of the fuel cell characteristics were carried out with a commercial high-purity hydrogen generator. Different load resistances were used. Electrical current in the circuit and voltage on the load resistance were measured directly. The fuel cell voltage was calculated taking into account its own internal resistance. Fuel cell voltage decreases with increasing current, that is typical for such kind of

devices [21] at low currents (less than an optimal current). The optimal current (when maximum electrical power can be achieved) for the tested fuel cell was about 3A. During the next experiments with the fuel cell, the current did not exceed 400 mA.

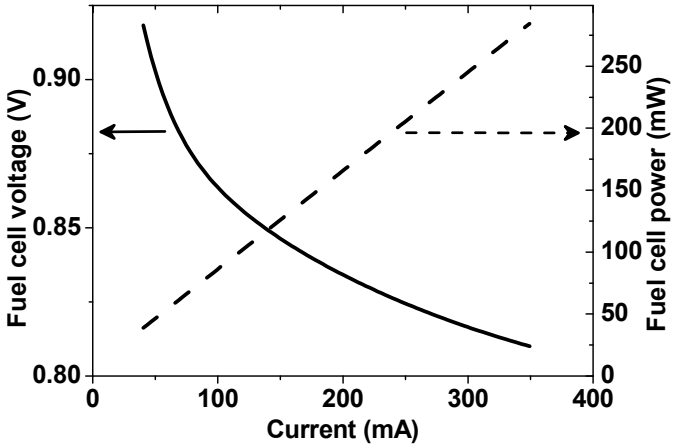

Figure 5 – Electrical characteristics of the used fuel cell

Functioning of the fuel cell supplied by hydrogen produced in our cartridge as function of the load resistance is shown on Figure 6. In this case, in order to ensure a quick delivering of hydrogen to the fuel cell, a thick output needle (250 μm in radius) has been used. The load resistance values were chosen to be: 100, 10, and 1 Ohms. During the measurements, falling of the drops was also observed. The lower the load resistance is, the higher the current is and the more frequent the drop falling is. It means that the fuel cell consumes the hydrogen produced by the chemical reaction in the cartridge. Current and voltage on the load resistance are shown in Figure 6 for different pressures in the chamber with pressurized air: dashed lines correspond to lower pressure, solid lines – to higher pressure. The higher pressure in the first chamber corresponds to higher electric power. By switching load resistance down to 1 Ohm, the higher power of fuel cell is achieved. As a result, higher hydrogen consumption takes place, and more frequent drop falling is observed.

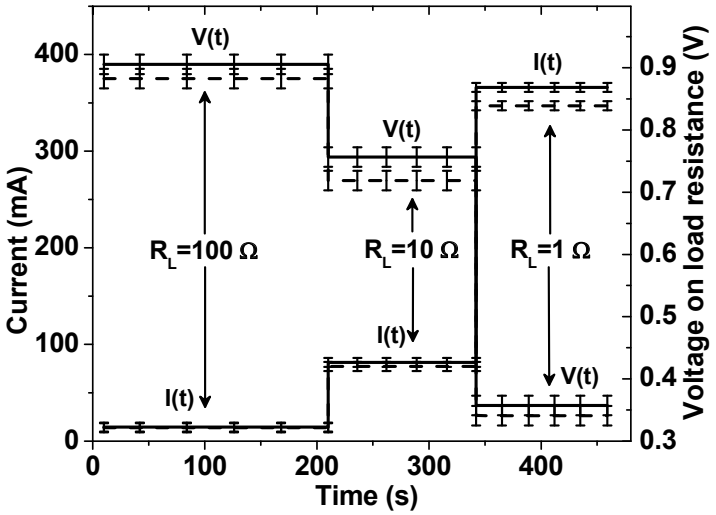

Figure 6 –Variation of the current in the circuit and voltage on the load resistance as function of the resistance value

Kinetics of the drop fallings was measured at different load resistances as shown in Figure 7. For each load resistance, the obtained data can be linearly fitted. The fitting line slopes are 0.024, 0.040, and 0.433 s^{-1}, respectively. The relative errors of the fitting do not exceed 10 %. The slope of the curve is proportional to the electric power consumed by the load resistances. By switching from 100 to 50 Ohm the electric power increases about 2 times. In contrast, by switching from 100 Ohm to 1 Ohm the power increases approximately only by 20 times, which corresponds to the I-V characteristic (see Figure 5) of the used fuel cell.

Due to the heat production during the reaction (2), the temperature of the reaction mixture increases. Established temperature depends on the heat exchange with air. Process of the temperature evolution for the chemical reaction with aluminum powder is shown in Figure 8 for the different load resistance. The load resistances were: 100, 10, 5, and 2 Ohms. One can see a strong correlation between the established temperature and the load resistance: the less the load resistance is, the higher the established temperature is and, at the same time, the higher the thermal power is produced.

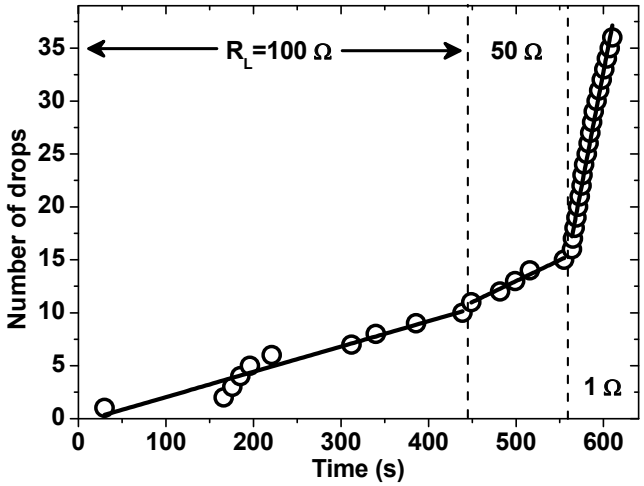

Figure 7 - Number of the fallen drops of the liquid reagent as function of time for different load resistance values

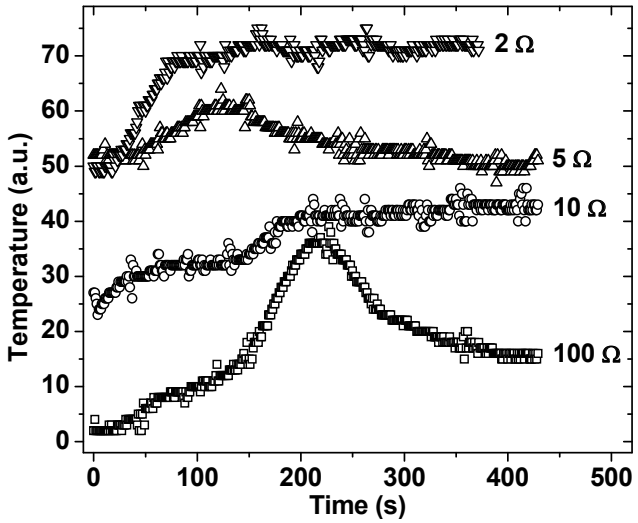

Figure 8 -Time dependent evolution of temperature in the reaction chamber as function of the load resistance

6. Conclusions

In the present work, a device for self-regulated hydrogen production was theoretically designed and experimentally characterized. The device consists of two chambers: the first chamber with pressurized air and liquid reagent, and the second chamber contains solid nanopowder reagent. Porous silicon or aluminum nanopowders can be used as solid reagents. The water with catalyst for porous silicon or alkali for aluminum were used as liquid reagent. The control mechanism was realized by means of a capillary tube connecting the first chamber with the second one. If the pressure difference between the chambers became higher than the capillary pressure (due to consumption of the generated hydrogen), the drop falls from the first chamber and hydrogen evolution leads to a decrease of the pressure difference. If the pressure difference is less than the capillary pressure and hydrogen is not consumed, the system achieve a steady state mode. Experimental results of the performed testing of the device prototype are in excellent agreement with the numerical simulation. The major advantages of the device described in the present article are:

i) working in a drop mode allows delivering of the electrical power for portable electronic devices;

ii) the involved regulation mechanism consumes no electrical power, so that the higher total efficiency can be achieved.

References

1. N.K. Zhevago, E.I. Denisov, V.I. Glebov. Experimental investigation of hydrogen storage in capillary arrays //Int. J. Hydrogen Energy. -2010. –Vol. 35. – P. 169-175.

2. N. Zhevago, E. Denisov. Apparatus for storage and liberation of compressed hydrogen gas in microcylindrical arrays and systems for filling the microcylindrical arrays // US Patent 7,870,878. - 2011.

3. J. Dong, X. Wang, H. Xu, Q. Zhao, J. Li. Hydrogen storage in several microporous zeolites // Int. J. Hydrogen Energy. – 2007. –Vol. 32. –P. 4998-5004.

4. B. Sakintuna, F. Lamari-Darkrim, M. Hirscher. Metal hydride materials for solid hydrogen storage: A review // Int. J. Hydrogen Energy. – 2007. –Vol. 32. –P. 1121-1140.

5. P. Kerrebrock, S. Wayne. Hydrogen generation by hydrolysis of hydrides for undersea vehicle fuel cell energy systems // U.S. Patent 5,372,617. - 1994.

6. K.S. Eom, K.W. Cho, H.S. Kwon. Hydrogen generation from hydrolysis of NH_3BH_3 by an electroplated Co–P catalyst // Int. J. Hydrogen Energy. -2010. –Vol. 35. – P. 181-186.

7. J. Macanás, L. Soler, A.M. Candela, M. Muñoz, J. Casado. Hydrogen generation by aluminum corrosion in aqueous alkaline solutions of inorganic promoters: The Al hydrox process // Energy. -2011. –Vol. 35. – P. 2493-2501.

8. S. Litvinenko, S. Alekseev, V. Lysenko, A. Venturello, F. Geobaldo, L. Gulina, G. Kuznetsov, V. Tolstoy, V. Skryshevsky, E. Garrone, D. Barbier. Hydrogen production from nano-porous Si powder formed by stain etching // Int. J. Hydrogen Energy. -2010. –Vol. 35. –P. 6773-6778.

9. V. Lysenko, F. Bidault, S. Alekseev, V. Zaitsev, D. Barbier, Ch. Turpin, F. Geobaldo, P. Rivolo, E. Garrone. Study of porous silicon nanostructures as hydrogen reservoirs // J. Phys. Chem. B. -2005. –Vol. 109. – P. 19711.

10. Ch. Zhan, P.K. Chu, D. Ren, Y. Xin, K. Huo, Y. Zou, N.K. Huang. Release of hydrogen during transformation from porous silicon to silicon oxide at normal temperature // Int. J. Hydrogen Energy. -2011. –Vol. 36. –P. 4513.

11. A.I. Manilov, S.A. Alekseev, V.A. Skryshevsky, S.V. Litvinenko, G.V. Kuznetsov, V. Lysenko. Influence of palladium particles impregnation on hydrogen behavior in meso-porous silicon // J. Alloys Compd. -2010. –Vol. 492. – P. 466.

12. A.I. Manilov, S.V. Litvinenko, S.A. Alekseev, G.V. Kuznetsov, V.A. Skryshevsky. Use of powders and composites based on porous and crystalline silicon in the hydrogen power industry // Ukr. J. Phys. – 2010. –Vol. 55. – P. 928.

13. D. Buttard, G. Dolino, C. Faivre. Porous silicon strain during in situ ultrahigh vacuum thermal annealing // J. Appl. Phys. – 1999. –Vol.85. –P. 7105.

14. E. Vázquez and J. Tagüeña-Martínez, Surface relaxation effects on the properties of porous silicon, J. Appl. Phys. -2002. –Vol. 91. – P. 3085.

15. D. Kovalev, V. Yu. Timoshenko, N. Künzner, E. Gross, F. Koch. Strong explosive interaction of hydrogenated porous silicon with oxygen at cryogenic temperatures // Phys. Rev. Lett. – 2001. – Vol. 87. –P. 068301.

16. F. V. Miculec, J.D. Kirtland, M.J. Sailor. Explosive nanocrystalline porous silicon and its use in atomic emission spectroscopy // Adv. Mater. -2002. –Vol.14. – P. 38.

17. P. Rivolo, F. Geobaldo, M. Rocchia, G. Amato, A. M. Rossi, E. Garrone. Joint FTIR and TPD study of hydrogen desorption from p+□type porous silicon // Phys. Stat. Sol. A. -2003. –Vol. 197. –P. 217.

18. T. Nychyporuk, V. Lysenko, D.Barbier. Fractal nature of porous silicon nanocrystallites // Phys. Rev. B. -2005. –Vol. 71. –P. 115402.

19. P. Kale, A.C. Gangal, R. Edla, P. Sharma. Investigation of hydrogen storage behavior of silicon nanoparticles // Int. J. Hydrogen Energy. -2012. –Vol. 37. –P. 3741.

20. S. Moghaddam, E. Pengwang, R.I. Masel, M.A. Shannon. A self-regulating hydrogen generator for micro fuel cells // J. Power Sources. -2008.-Vol. 185. –P. 445-450.

21. B. Tazi, O. Savadogo. Parameters of PEM fuel-cells based on new membranes fabricated from Nafion®, silicotungstic acid and thiophene // Electrochim. Acta. -2000. –Vol. 45. –P. 4329-4339.

22. B.J. Kirby. Micro- and nanoscale fluid mechanics: transport in microfluidic devices, Cambridge U.P., New York, 2010.

IRSTI 29.35.29

Positron annihilation spectroscopy of clumpy structures 1. Type II young Supernova remnants

D.N. Doikov[1*], S.M. Andrievsky[2] and A.V.Yushchenko[3]

[1]*Department of Mathematics, Physics and Astronomy, Odesa National Maritime University, 34 Mechnikov St., Odesa, UA-65029, Ukraine*
[2]*Department of Astronomy and Astronomical Observatory, Odesa National University, 1v Marazliyvska St., Odesa, UA-65014, Ukraine*
[3]*Astrocamp Contents Research Institute, Goyang, 10329, Republic of Korea*
[*]*e-mail address: doikov@mail.bg*

The clumpy structure of the SN 1987A ejecta revealed by numerous IR observations has been described. The simulation of the clump formation in the progenitor star's explosion was performed. The Sedov self-similar solutions of the problem of a strong explosion were used to construct the model spectra of the initial clumps formed due to the Rayleigh-Taylor (RT) instabilities arisen during the metal core collapse prior the supernova explosion. After short time main part of the clumps accumulates mainly the heavy elements, including radioactive isotopes. In this paper, we investigated the properties of the element mixture with radioactive isotopes, especially $^{44}_{22}Ti$. Mapping of the ejecta clumps was performed through the obtained spectra of their radiation field depending on time, initial spatial distribution and composition. Numerical simulation of positron trapping across nebular envelope supported the new possibilities for positron γ-spectroscopy and chemical diagnostics. The exact results of the quantum annihilation processes with inner K–electrons produce one γ–quant process are tested for SN 1987A envelope clamps. Aspherical clumps distribution presented and used how to test the elements separation after explosion. We presented the accompanied nonthermal emission after positrons energetic losses in cool explosion of the envelope and the distribution of Auger electron nebular plasma with small dust fraction. This secondary emission of atomic quants and fast electrons is connected with aroused diffuse nebular emissions. We found that only one γ–quant annihilation line for chemical elements from the middle part of periodic table of chemical elements should be usable for future positron spectroscopy activity. For exact solution of this problem we selected clamps without graphite dust, which contain the radioactive isotope $^{44}_{22}Ti$, and show the production of standard positron current in the case of standard chemical composition.

Key words: gas-dust space medium, auger – electrons, supernovae remnants, positron spectroscopy.
PACS numbers: 98.58. – w. 98.58. Mj, 95.30. Dr.

1 Introduction

Infrared observations have been an important source of information about supernova remnants over the last 30 years. In general, they provided an insight into the chemical composition of the dust grains consisting of astronomical silicates and amorphous carbon. Observations of SN 1987A have been the most informative. The distance to the SN 1987 (50 kpc) and its current age (31 years) allowed establishing the onset of dust formation in the debris, its physical properties, as well as to follow further evolution of the remnant. The total mass of dust in the remnant of SN 1987A reaches 0.8 $M_{\odot}$.

However, the most important output of the space IR observations in recent years, including those obtained by the Spitzer Space Telescope, is the detection of the fragmentary (clumpy) structure of the ejecta at early stages in its evolution. The time scale of such clumpiness coincides with the time scale of complete hydrogen recombination in the ejecta. The remnant geometry at the current epoch is being reconstructed from the structure of the shock fronts visible in different spectral ranges. As of today, the lower theoretical limit on the number of clumps N_C in the ejecta is determined to be 100. Varosi & Dwek [6] have proposed a technique of the geometry-based simulation of the supernova

clumped ejecta with dust grains being the only factored in component. The N_C values may change with increasing sensitivity of the instruments used. The upper limit on the N_C values can be estimated directly from the computations of the supernova explosion model, in particular, in the last pre-explosion stages when the gas is infalling from the envelope onto the dense stellar core. The RT instabilities, being initiated at this stage, induce formation of clumps, and the core matter is driven toward the overlying zones Müller *et al*., [9], Woosley [8]. Such outer zones are present in all simulations of the Type II supernova explosions. Therefore, the N_C values describe the number of such survived clumps derived from the observations of the young remnant of SN 1987A.

One may distinguish among three main phases which the supernova remnant passes as it expands. Being placed in chronological order, these are non-adiabatic, adiabatic and non-adiabatic phases. The first phase occurs on relatively small time scales when material from the envelope falls in and then rebounds off the core ultimately triggering the explosion and explosive ejecting of the matter. By that time (within the first 100 seconds after the outburst) the ejecta clumps have been already formed due to the RT instabilities. At the current epoch, we have been observing the adiabatic phase of the remnant evolution when the energy of all examined processes is by 16-18 orders of magnitude lower than the total kinetic energy of the ejecta (10^{51} erg). In mechanics, changes in the thermodynamic and kinematic parameters of the remnant are described by the similarity method – the Sedov method, which was applied by Zeldovich and Raizer [14] to solve the problem of strong explosion in a relatively rarefied medium.

Taking into account some constraints on the use of a self-similar solution (for the first and third stages of the remnant evolution), the description of the clump structure when switching from small scales to large scales and vice versa in the adiabatic phase appears to be plausible and convenient. Therefore, when solving the inverse problem on the explosion structure reconstruction from the known parameters of the ejecta clumps at the current epoch of observations, the requirement for compliance with the self-similar approximation places a constraint on its application on the considered time and geometric scales of the explosively ejected matter. When the clumps are expanding, they overlap each other with respect to the line of sight. However, according to modern observations, the factor of such overlapping is rather small. Let us express it in terms of ξ. Thus, the ejecta clumpiness makes it possible to perform model mapping of such clumps with further definition of the observation objectives.

The International Gamma-Ray Astrophysics Laboratory (INTEGRAL) observations have revealed a large amount of radioactive isotope of titanium $^{44}_{22}Ti$ Grebenev et al [16] in SN 1987A. The presence of this isotope has two important implications. First, even at low mean thermodynamic temperatures, the average energy in the clumps, which is emitted in the non-thermal part of the spectrum, is considerable due to radioactive decays. With regard to SN 1987A, we observe permanent hard radiation with a half-life of 85 years. Currently, the amount of energy $\boldsymbol{E}$ deposited in the debris by the radioactive decay of titanium isotope is 10^{36} erg. Hard primary radiation, which includes emission of fast positrons, is responsible for the distribution of the radiation field that differs significantly from the thermal one. Secondly, the local electron energy distribution function is formed due emission of the high-energy Auger electrons associated with the ionisation loss of fast positrons. The electron constituent of such ionised gas is responsible for the increased IR fluxes from dust and is involved in the ionisation-recombination balance of the gas, in particular, in excitation of atomic outer shells, which define the composition of the ejecta. Considerable experience in diagnostics of interstellar dust by means of the IR spectroscopy has been gained, making it possible to use the deduced quantitative parameters to distinguish between properties of the condensed swept-up interstellar matter and those of the ejecta's own condensate. It also becomes possible to perform diagnostics of the current state of the ejecta atomic constituent under conditions of varying composition of its clumps due to various radioactive decays, in particular, due to a series of β-transformations $^{44}_{22}\mathrm{Ti} \xrightarrow{85\,\mathrm{y}} {}^{44}_{21}\mathrm{Sc} \xrightarrow{6\,\mathrm{h}} {}^{44}_{20}\mathrm{Ca}$ in the matter inside the clumps [17, 18]. Therefore, it is apparent that spectroscopic manifestations of actual changes of the chemical composition should be observed in the supernova remnant at the current epoch of observations.

This paper discusses modelling of mechanical and thermodynamic properties of the ejecta clumps from the space-based observations, as well as reconstruction of the initial state of these clumps prior to the supernova explosion. The results of the model spectra imaging within the constraints of the

observed spatial pattern of the geometry of the remnant of SN 1987A will be presented in our further studies.

2 The clumpy structure of the ejecta of SN 1987A in the infrared spectra

The study of the chemical composition of the ejecta of SN 1987A requires observations at a rather high angular resolution. The preliminary mapping of the debris suggests that it can be shaped like either a prolate spheroid or a cylinder. The observations have shown that the shock breakout occurred through the poles along the rotation axis of the progenitor and in the equatorial plane. At present, the blast wave fronts have travelled far from the debris and can be clearly observed across all wavelengths covered by modern space telescopes. The velocity of the blast wave propagation is multi-fold higher than the expansion velocity of the ejected matter. Today, more than 31 years after the explosion, the largest telescopes can finally perform mapping of the debris. On the other hand, calculation of Type II supernova explosion models necessitates factoring in asymmetric elemental distribution within the volume of the ejecta. According to recent IR observations of the remnant of SN 1987A, the ejecta clumpiness becomes apparent.

The emission from silicate and carbon-containing dust grains, which is sufficient to resolve geometric sizes in the adiabatic phase of the remnant expansion, serves as a marker of such clumpy structure. Until recently the clumps were illuminated by hard X-ray and ultraviolet output from three blast-wave fronts, which have already travelled quite far, as well as due to the energy deposited by the radioactive decay of titanium isotope -$^{44}_{22}Ti$ in the innermost regions of the ejecta (Jerkstrand et al [1]). Simultaneously, the dust temperature increased, and the dust grains themselves started emitting infrared radiation. Numerous observations of the dust grains in the ejecta and their interpretation by Dwek & Arendt [10] enable us to reconstruct the morphology of the clumps reproducing the IR spectra and define their quantitative characteristics. To solve this problem, let us perform the preliminary analysis of the clump characteristics. To this end, as in Varosi & Dwek [6], we introduce the volume filling factor of the clumps in the ejecta – f_V and the cross section of individual clumps – x. Let ξ be a factor of order unity that compensates for the overlapping of clumps along a given line of sight. We also assume that clumps are of the same size ($r_C = x$). Then, from the constraint $N_C r_C^2 = \xi R^2$ for a given spherical clump with radius r_C we obtain its optical depth – τ_C:

$$\tau_C = \frac{3}{4}\frac{M_d/N_c}{\pi r_C^2}, \quad (1)$$

where M_d is the total dust mass in the ejecta. Determination of detailed elemental abundances throughout the volume of the ejecta requires that within the investigated spectral range of observations the relevant optical depth is subject to the condition $\tau_C \leq 1$. Combined space-based observations in recent years have shown that the total energy fluxes in the X-ray, UV and IR spectra of SN 1987A tend to decrease; this is due to decreased luminosity at the shock fronts and destruction of interstellar dust concentrated in the vicinity of these leading shock edges. In this case, the energy flux is dominated by the emission from the debris of this supernova. The clumps themselves being expanded become optically thinner, making it easier to observe their inner regions. Under given conditions, the mean free path of a photon through the ejecta l can be derived as follows:

$$l = \frac{1}{N_C \pi r_C^2} \quad (2)$$

The growth rate of the clumps in the inertial reference frame relative to an arbitrary point in the expanding debris is many orders of magnitude lower than the expansion velocity of the ejecta. It should also be noted that in this case the clump overlapping factor ξ is negligible and does not exceed 0.1. Given a uniform distribution of the clumps throughout the ejecta volume, we can estimate the overlapping factor ξ by formulae (3) and (4) presented in the next section.

2.1 Boundary conditions for the problem and imaging of the debris.

The bolometric luminosity of the supernova debris together with the emission at blast-wave surface in across all spectral bands makes up 300 $L_\odot$, of which 63 $L_\odot$ contributed by the X-ray emission at the shock fronts. The main energy input for the remaining luminosity of the remnant of SN 1987A is provided by the radioactive decay of $^{44}_{22}Ti$ nuclei leading to the non-thermal fluorescence of

gas in the ejecta, and by the emission from the dust grains. Taking into account the modern data on the remnant geometry, its actual size is R=10^{15} m at the expansion velocity of the ejecta layers within the range of 800-1200 km/sec. We have inferred from the hydrodynamics of the supernova explosion that the remnant mass is concentrated in the zone of 0.1**r* where ***r*** is the current position of the outermost part of the remnant relative to the explosion site (Shklovsky, [13]). Factoring in the clumpiness and non-sphericity of the ejecta zones enables us to estimate the density $\boldsymbol{\rho}$ in an ejecta zone. The estimated values are about $\rho = 10^{-17}$-10^{-18} kg/m^3 or 10^9-10^{10} atoms/m^3 (Jerkstrand, [1]). Under given conditions, the translational kinetic energy of the ejecta zone is 13 orders of magnitude higher than the energy deposited by the radioactive decays occurring in this zone.

However, even with such radioactive decay energy input, there is an efficient mechanism of conversion of the radioactive decay energy into the emitted radiation. Thus, there may be preconditions for the ejecta luminosity to become sufficiently high that it can be mapped or spectroscopically studied. Physical conditions at the ejecta surface are similar to those observed at the shocks. Hence, the atomic spectroscopy of the supernova debris should take into account the interaction between the ejecta and circumstellar gas. Eventually, with such a source of conversion of the energy of the debris translatory motion into thermal chaotic motions, the spectrum of multi-charged ions typical at the shocks appears being overlapped by the emission spectrum produced within the volume of the ejecta (inner diffuse ejecta spectrum). This problem is to be discussed in the next paper though.

3 Reconstruction of the original picture of the SN 1987A explosion

The analysis of observations of this supernova is based on the application of the similarity method which is used to define the relationship between the temperature $\boldsymbol{T(M_r t)}$, density $\boldsymbol{\rho(M_r, t)}$ of the ejecta, the distance from the explosion site ***r*** and time scale of the process. In many cases, this approach is the most efficient among others due to its physical simplicity, availability and small number of free physical parameters. Being adhered to the similarity method, we are to consider the results of IR observations at the current epoch and parameterize the structure of the clumps in the debris in the same manner as in the previous section. The state of the clumps can be defined by:

$$\rho(M_r, t) = \rho(M_0, t_0)\left(\frac{t}{t_0}\right)^{-3}, \qquad (3)$$

$$T(M_r, t) = T(M_0, t_0)\left(\frac{t}{t_0}\right)^{-3(1-\gamma)}. \qquad (4)$$

where $M_0 = 20M_\odot;\ \gamma = 1{,}25 - 1{,}30$. Each clump has its distinct size defined by its own initial conditions. The similarity relations for these clumps are linearly dependent on ***r*** and ***t/t₀***. The growth of a clump depends on the time and difference between the pressure inside the clump and in the inter-clump medium. The growth of clumps is proportional to the time elapsed since the explosion and it occurs simultaneously with the overall expansion of the remnant. In the simplest case, the size distribution of clumps may be set taking into account that we know their observed root-mean-square size ***w(x)dx***, i.e. the probability that within a given range of sizes ***dx*** the following is true:

$$w(x)dx = \frac{1}{\sqrt{2\pi\sigma}}\exp\left(-\frac{x^2}{2\sigma}\right)dx \qquad (5).$$

The dispersion coefficient $\boldsymbol{\sigma}$ and mean size of a clump $\boldsymbol{\bar{x}}$ in the above formula should be estimated and compared with the observed values. As of today, we assume without loss of generality that the upper limit on the dispersion $\boldsymbol{\sigma}$ is $\sigma = 10^{13} - 10^{14}$m. To get a complete picture of the explosion, it is needed to perform similarity transformations with respect to density, temperature and geometric size. It means that equations (3) and (4) will be solved for the gas that surrounds the clumps and consists mainly of light elements. Further, we will examine the clump evolution at a given evolutionary interval.

In order to perform spectral diagnostics of the supernova clumped debris for a given clump structure, it is convenient to consider the probability ***P(z)dz*** that a photon will survive in the clumped layer ***z,z+dz*** where z is the axis along the projected area of the ejecta with the number density of clumps $\boldsymbol{n_C}$, which is given by:

$$P(z)dz = e^{-\frac{z}{l}}\frac{dz}{l} \qquad (6)$$

where l is the mean free path of a photon through the ejecta,

$$l = \frac{1}{n_c \pi r_c^2} \quad (7)$$

According to Varosi & Dwek [6]

$$P(b)db = \int_0^{2R\sqrt{1-(\frac{b}{R})^2}} e^{-\frac{z}{l}} \frac{dz}{l} \quad (8)$$

Then, the fraction f_A of the projected area of the ejecta filled by clumps is given by the integral:

$$f_A = \frac{1}{\pi R^2} \int_0^R P(b) 2\pi b db \quad (9)$$

Thus, having known the fraction f_A and size distribution of the ejecta clumps, we can proceed to the reconstruction of the original picture of the supernova explosion. We consider that temperature and density obey to the similarity transformations; so does the linear size. Along with the time scale of the process, the cross section of individual clumps – ***x*** is also an independent dimensional variable involved in the similarity transformations. When solving this problem, we need to reduce the time scale and ***r***. The iteration process is to be terminated at the instant of time when the conditions of adiabatic compression are no longer met. This approach would be acceptable when the radiation does not influence the ejecta dynamics, i.e. when quanta are not confined in the matter. At the indicated instant of time, any of 100 clumps is noticeably affected by the shocks passed through the ejecta as these clumps are many orders of magnitude denser than the surrounding medium and remain intact being compressed by the blast waves produced in the supernova explosion. According to Varosi & Dwek [6], the fraction $f_A = 0.6 - 0.94$ with the total number of the ejecta clumps N_C=100 and N_C=1000 whereas the volume filling factor of the clumps in the ejecta $f_V = 0.1 - 0.8; 0.003 - 0.25$ with N_C=100 and N_C=1000, respectively. Further observations will enable us to improve the values f_A, f_V and N_C, although it appears that the defined problem can be solved using the above estimates, and the number of clumps can be determined even now.

4 Instability and clumps during the supernova explosion

One of the most meaningful conclusions drawn from the research of the supernova explosion is that hydrodynamic events when the iron core is being compressed by the infalling matter are of crucial importance (Popov *et al*., [7]). It is a surprising fact that despite hundreds of different scenarios of the Type II supernova explosions suggested, the supernova energy eventually varies around the value of $E_0 \sim 10^{51}$ erg whereas the mass of the ejecta differ. The peculiarity of the SN 1987A explosion is the absence of the relativistic remnant that allows assuming the mass of the ejecta to be equal to $20\ M_\odot$. The Rayleigh-Taylor (RT) instability, arisen when the progenitor's envelope matter falls onto the dense core prior to the explosion, plays a crucial role in the elemental and spatial distribution of the debris. A detailed analysis of this RT instability based on the hydrodynamic and thermodynamic specific features of the physical processes at different times after the iron core collapse (Müller *et al*., [9]) allowed determination of important relations for the kinematic properties of the initial clumps. First of all, we compare the criteria for such RT instability to grow for an incompressible gas,

$$\frac{\partial \ln \rho}{\partial r} / \frac{\partial \ln p}{\partial r} < 0 \quad (10)$$

as well as for a compressible gas under the same conditions and with the same adiabatic index:

$$\frac{\partial \ln \rho}{\partial r} / \frac{\partial \ln p}{\partial r} < \frac{1}{\gamma} \quad (11).$$

The growth rate of such an instability in the incompressible case is given by

$$\sigma = \sqrt{-\frac{p \frac{\partial \ln \rho}{\partial r} / \frac{\partial \ln p}{\partial r}}{\rho}} \quad (12)$$

For the compressible case it is given by

$$\sigma = \frac{c}{\gamma} \sqrt{\left(\frac{\partial \ln p}{\partial r}\right)^2 - \gamma \frac{\partial \ln p}{\partial r} \frac{\partial \ln \rho}{\partial r}} \quad (13)$$

where ***c*** is the adiabatic sound speed. Then, we introduce two amplitudes of the RT instability growing from the initial perturbation with amplitude ξ_0 at time t=0 to amplitude ξ at a given time ***t***.

In fact, the time scale of a RT instability active growth up to the final formation of an RT finger is 100 seconds. The main causes of the ejecta fragmentation into clumps are the presence of the RT instabilities and kinematic viscosity of the medium that result in the inhomogeneous density and elemental distribution of the ejecta. The values of the logarithmic derivatives in formulae (10)-(13)

are directly proportional to the dimensionless rates of the relevant thermodynamic values and sensitive to the non-linearity of the process.

Let us assume that all heavy elements comprising the core have been transferred to 100 fragments. From this distribution of elements the chemical composition of the clumps can be derived. Let us split the surface of the core into 100 fragments. Each fragment is formed as a clump due to the RT instabilities. Thermodynamic parameters inside such a clump formed due to the RT instability change in two stages. At the first stage, which is non-adiabatic, the clumps grow in size according to formulae (11) and (12) during 100 seconds. Then, on the time scales longer than 100 sec, the mean temperature $\boldsymbol{T(M_r, t)}$ and mean density of a clump $\boldsymbol{\rho(M_r, t)}$ can be calculated by formula (3) over a period till the current epoch. At the current epoch of observations, the clumps are clearly seen in the Spitzer infrared spectra. In the inter-clump medium, there are hydrogen, helium and other light elements comprising a substantial fraction of the ejecta. The observed structure of this population of fragments of debris formed in the explosion fits in a cylinder whose axis coincides with the pre-explosion rotational axis of the progenitor. Therefore, to perform mapping of the debris through its images, we are to detect its spectral manifestations according to the following scheme:

- all the fragments are distributed within a cylinder with the dimensions observed at the current epoch in the gamma-ray, X-ray, UV and IR bands;
- the fragment composition depends on the after-explosion elemental distribution (as shown in Figure 1, and Table 1 in Popov et al [7]);;
- individual fluorescence spectra of all fragments are defined by the non-thermal radiation field powered by the ionization loss of positrons emitted in a series of β-transformations $^{44}_{22}\mathrm{Ti} \xrightarrow{85\ \mathrm{y}} {}^{44}_{21}\mathrm{Sc} \xrightarrow{6\ \mathrm{h}} {}^{44}_{20}\mathrm{Ca}$, as well as by the chemical composition of each fragment [2].

To make further calculations, we need to compute the radiation field of several standard clumps with a given composition that contain a condensed phase consisting of a mix of astronomical silicates and graphite. Thus, in this section we have determined the spectroscopic manifestations of asymmetricity of the Type II SN 1987A explosion which resulted in inhomogeneous distribution of elements in the debris. The fragments in the polar and equatorial regions of the remnant are expected to exhibit the abundance of heavy elements and products of their nuclear fission, including $^{44}_{20}Ca$, which will be sufficient for their detection. Imaging of the ejecta in the form of clumps depending on their initial spatial and elemental distribution is illustrated in Figure 1.

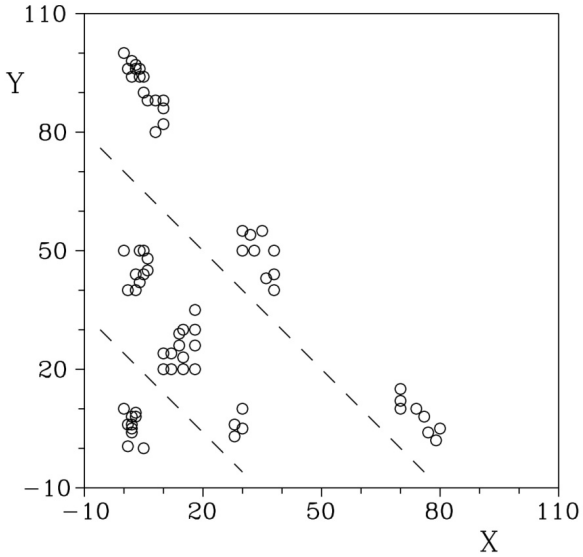

Figure 1 – The spatial model of the ejecta at three different epochs, namely near the zero time, after 15 years, and after 31 years. The groups are divided by dashed lines. The units of the axes are 10^{13} meters. The horizontal axe is the direction to equator, the vertical – to the pole. The points mark the places where $^{44}_{22}Ti$ molecules are concentrated

5 Mapping of the images of the SN 1987A ejecta clumps

As is shown in the previous sections, both imaging of the remnant at the current epoch and its future mapping at different wavelengths are defined by its geometry, physical structure and chemical composition. As of today, high-quality images of two polar and one equatorial shock surfaces have been obtained. The data from the shock fronts at the nearest epoch will be used to study the circumstellar gas morphology, as well as the debris of the cocoon from which SN 1987A was formed. Modelling the remnant image at different time scales is mandatory for the determination of the spatial distribution of elements in the ejecta. Unlike the supernova remnants with a compact source, the expanding clumped ejecta of SN 1987A demonstrate their own emission throughout the volume. In these clumps, the main contribution to the radiation is made by two dust species (graphite and astronomical silicates) and atoms excited by fast positrons. As reported in Jerkstrad [1] and Doikov *et al*., [17-19], the spectral composition of the radiation emitted by a clump depends on its composition without regard to the dust. Modern observational data obtained by the Spitzer Space Telescope are sufficient to spatially resolve images of the ejecta clumps while the properties of these clumps are defined by their dust content. The predominance of astronomical silicates results in decreased absorption of visible and UV radiation. Graphite does not let either optical nor UV radiation through. However, γ and X quanta generated in the annihilation of fast positrons are poorly absorbed. In the progenitor, the abundance of oxygen outweighed that of hydrogen. Hence, as in Dwek & Arendt [10], Osterbrok [11], Lucy [12] the estimated composition of the dust grains favors the prevalence of astronomical silicates. The calculations of the Type II supernova explosions yielded the mean chemical composition of the remnants presented in section V. After the passage of positrons, each of the reduced atoms undergoes cascade transitions and emits the Auger electrons. Let us add dust grains with steady-state IR emission to these atoms; hence, we assume that $\boldsymbol{\tau_\iota}$ is the optical depth of $\boldsymbol{l}$ absorbers and emitters. Taking into account the results of the study of the optical spectra of SN 1987A, the recorded evidence of the presence of clumps, as well as physical conditions inside the clumps, indicates that the graphiteous dust emission is present at the distant shock fronts while astronomical silicates are concentrated inside the ejecta clumps. These silicates have been formed in the expanding ejecta under conditions described in the study by Kozasa [15], and their emission has been recorded by the Spitzer Space Telescope. The data on the radiation emitted by the dust show an excess in their IR emission due to additional heating by the Auger electrons and secondary short-wave quanta. Silicates add to the mean optical depth of the indicated $\boldsymbol{l}$ absorbers. Taking into account the absence of a central source of emission, we are to use the Osterbrock-Lucy formula [11], [12] for the emitters and absorbers uniformly distributed in the emitting volume:

$$\mathcal{P}_{esc}^{unif}(\tau,\omega) \equiv \frac{P_e(\tau)}{1-\omega[1-P_e(\tau)]} \quad (18)$$

$$P_e(\tau) = \frac{3}{4\pi}\left[1 - \frac{1}{2\tau^3} + \left(\frac{1}{\tau} + \frac{1}{2\tau^2}\right)e^{-2\tau}\right] \quad (19)$$

where $\tau_{ext} = \tau_{abs} + \tau_{scat}$ and $\omega = {}^{\tau_{scat}}/_{\tau_{ext}}$.

Assuming that $\boldsymbol{\varepsilon}$ is the emission per unit volume of a clump and using formulae (18) and (19), Dwek & Arendt [10] have obtained formulae of the intensity $\boldsymbol{I_{out}(\tau,\theta)}$ and total emerging flux $\boldsymbol{F_{out}(\tau)}$, which will be convenient for further calculations:

$$I_{out}(\tau,\theta) = \frac{\varepsilon}{\rho\kappa}(1 - e^{-2\tau\cos(\theta)}) \quad (20)$$

$$F_{out}(\tau) = \frac{\pi\varepsilon}{\rho\kappa}\left(1 - \frac{1}{2\tau^3} + \left(\frac{1}{\tau} + \frac{1}{2\tau^2}\right)e^{-2\tau}\right) \quad (21)$$

For the ejecta clumps with different composition the total emerging flux $F_{out}(\tau)$ depends on the ratio between the scattering, absorption and emission coefficients. The structure of the radiation field of clumps containing no dust has been described in Doikov (2017), including the definition of the source function S (E,r). The presence of a substantial amount of the graphite dust in the debris should have noticeably suppressed the short-wave part of S (E,r) that could have made the formation of the remnant atomic spectra impossible; though, in fact, those spectra were observed in 1995. The graphite dust contributes to the emission at the shock fronts of SN 1987A whereas the silicate dust emission fits better to explain the spectroscopic features of the ejecta. The particle-size distribution function $\mathrm{n(a)} \approx a^{-3,5};\ 10^{-9}m < a < 0.25 \cdot 10^{-6}m$ is typical for the silicate dust.

When interpreting the spectroscopic data for the interstellar medium and supernova remnants, we consider the so-called astronomical silicates. Apart from their own emission, these particles scatter the short-wave component of S (E,r) and let the optical and IR emission through. When calculating monochromatic optical depth of a clump for a given S (E,r), we can add the formula for the emerging flux produced by astronomical silicates of a given type to formula (21) for the total emerging flux $F_{out}(\tau)$:

$$F_{\lambda}^{sil}(\lambda) = 4\pi m_d k(\lambda) B_{\lambda}(T_d) \qquad (22)$$

In this formula, $\boldsymbol{m_d}$ is the mass of silicate dust in the ejecta clump; $\boldsymbol{k(\lambda)}$ is the absorption coefficient for a given type of astronomical silicates; $\boldsymbol{B_{\lambda}(T_d)}$ is the Planck function for particles with temperature $\boldsymbol{T_d}$. Spectroscopic images of the ejecta clumps depending on S(E,r) by the values of the emerging fluxes $F_{out}(\tau)$ and $F_{\lambda}^{sil}(\lambda)$.

6 Formation of spectral lines in the clumpy structures of the supernova remnants

The specific physical feature of the ejecta clumps is their emission throughout the entire volume, i.e. the uniform distribution of the emitters and absorbers in the ejecta. At the same time, there is no reversing (a relatively cold) layer in the ejecta. Media with such a layer include, for instance, stellar chromospheres that have relatively low gas density. In this case, the transitions induced by the collisions of atoms with molecules in the ejecta are unlikely to occur. These collision-induced transitions, as mentioned in the previous sections, are caused only by positrons due to their considerable mobility. According to Jerkstand [1], the excitation of the optical transitions of atoms is only due to radiation. To make a spectral line prominent, the radiative excitation rate should be consistent with the optical cascade rates. This problem can be solved if S (E,r) has been preliminary defined. The rate of excitation quanta formation is defined by the number of collisions of positrons with atoms per unit of time z per unit volume $z = < v > / < \lambda >$, as well as by the composition and geometric characteristics of the clumps. In this case, we assume that the debris is shaped as a prolate spheroid. Detailed positional radio-astronomical observations of the remnant of SN 1987A, along with the data obtained by the Hubble and Spitzer Space Telescopes, INTEGRAL, etc., allowed of determination of the three-dimensional structure of the ejecta and shock surfaces. As a result, the cosines of the angle between the projected plane and normal to the line of sight have been determined: $i_x = 41^0, i_y = -8^0$, $i_z = -8^0$. The eccentricity of the spheroid is 1.18.

In the review by Potter *et al*. [4], the quantitative parameters of the remnant were calculated from the radio-astronomical data; that allowed obtaining the gradients of the main thermodynamic parameters defined over the width between the inner and outer regions of the ejecta:

$$\nabla \mathrm{n} = \frac{(10^8 - 10^5)(m^{-3})}{\Delta r\ (m)};$$

$$\nabla \mathrm{P} = \frac{(10^{-15} - 10^{-2})Pa}{\Delta r(m)}; \qquad (23),$$

$$\nabla \mathrm{T} = \frac{(10^{-2} - 10^{6})K}{\Delta r(m)}$$

where ∇n, ∇P and ∇T are the number density, pressure and temperature gradients, respectively, defined over the width between the inner and outer regions of the ejecta. For the entire remnant the Δr value is $\Delta r \approx 0.5 \cdot 10^{16} m$. If the observed fragmentation into clumps occurs, then value Δr makes $\Delta r \approx 0.5 \cdot 10^{16} m/N_c$. In this case, the given gradients in N_c clumps affect the dynamic evolution of the clumps in the proper reference frame. As time progresses, the clumps expand with consequent decrease in the number density, temperature and pressure. Factoring in the radioactive decays in a series of β-transformations ${}^{44}_{22}\mathrm{Ti} \xrightarrow{85\,\mathrm{y}} {}^{44}_{21}\mathrm{Sc} \xrightarrow{6\,\mathrm{h}} {}^{44}_{20}\mathrm{Ca}$ results in additional ionisation of the matter and in increased mean thermodynamic temperature Sigmund [3]. According to the INTEGRAL observations (Grebenev, [16]), the total mass of the radioactive isotope of titanium ${}^{44}_{22}Ti$ was about 10^{27} – 10^{28} kg during the period of observations. Then, the mass of ${}^{44}_{22}Ti$ confined in the clumps should account for their size distribution within the volume of the spheroid debris.

We have taken into consideration the results of numerous calculations using the explosion models of the progenitor of SN 1987A which prove that an essential fraction of the clumps, and hence heavy elements in these clumps – the nucleosynthesis products, is concentrated in two near-polar and narrow equatorial regions. The bulk of the progenitor's matter after its explosion is

concentrated in the form of light elements in the inter-clump medium and outer regions of the debris. The clumps due to their significant inertness are concentrated in the inner part of the ejecta. To construct a model of the bolometric luminosity of the remnant, it is necessary to estimate the emission from each clump and then integrate it with respect to all geometric and physical specific features. All spectral line profiles also depend on the results of this mapping. In all clumps containing the major fraction of heavy elements the abundance of $^{44}_{20}Ca$ has increased by 30% over last 31 years, and it has been taken into account when calculating the optical characteristics of the clumps in the debris.

The integrated source functions and electron velocity distribution functions for the indicated main clumps in the ejecta are presented in Figs. 1-3 in Doikov et al [19] illustrate how the chemical composition of the clumps and the presence of dust influence the H and K $^{44}_{20}Ca$ II line profiles.

The presence of rather intense fluxes of positrons and electrons with the kinetic energies 10^3 times higher than the excitation energies for the H and K CaII, as well as neutral Ca I lines, leads to the formation of the lines of these elements. The second source of excitation is the hard radiation field from the iron-peak atoms formed in the cascade transitions after the passage of fast positrons. All these processes are important after the hydrogen recombination. A rather high degree of vacuum in the nebular remnant is offset by intense emission of the secondary Auger electrons and photons. The values of the resolved radiation function S (E,r) and electron velocity distribution function F (E,r) are given for the clumps with a defined spherical shape and composition. With the defined functions S (E,r) and F (E,r) the radiative energy balance for the H, K CaII and Ca I lines can be calculated. Given that the clumps were formed at one and the same instant of time, the model Ca line profile can be determined for each clump.

7 Conclusions

In the present paper, all the results have been obtained with an assumption that the young remnant of SN 1987A contains an important energy source, namely radioactive isotope of titanium $^{44}_{22}Ti$. Generating substantial fluxes of fast positrons, the remnant emits radiation throughout the entire volume of the ejecta clumps and inter-clump matter [5]. We have shown that all the clumps can be split into two groups. These groups are related primarily to the asymmetry of the supernova explosions. The majority of the ejecta wq clumps (among those 100 clumps which have been already detected) contain practically all iron-peak elements whereas the remaining clumps consist of C-N-O elements. Hydrogen and helium are concentrated in the frontal regions of the remnant, as well as in the interclump medium in the ejecta.

We suppose, according to formulae (14)-(17), that the equatorial part of the debris consists predominantly of the heavy iron-peak elements, including radioactive ones, whereas the clumps containing C-N-O elements are located in the polar regions of the ejecta. The silicate dust was formed mainly in the clumps in the equatorial region of the debris, and its fluorescence is caused by the local radiation field and fast positrons. Here we also expect the conditions for the formation of the $^{44}_{20}Ca$II emission lines and excitation of rotational transitions of the H_2 molecule in the inter-clump region.

The radiation field energy is sufficient for detection of the titanium molecules. However, their detection and identification requires additional observations and calculations which are to be the subject of our future papers. Intense formation of the graphite dust occurred in the polar regions of the ejecta. Its presence in the clumps and around them results in blocking out the short-wave UV and optical radiation. The fact that SN 1987A produces optical spectra indicates that the graphite dust is concentrated in certain regions of the ejecta or that it can be observed due to its heating at the shock fronts. Figure 1 illustrates the evolution of the emerging flux due to the growth of the ejecta clumps.

Radio-, IR and X-ray observations of the remnant of SN1987A have shown a decrease in the IR and UV fluxes and an increase in the radio flux. This evidence suggests that the fluxes emerging at the shock fronts have been decreasing, hence one can learn about the remnant only by examining its own energy sources.

Acknowledgments

We thank Prof. Valery M. Chechetkin for providing us with the explosion model and useful discussions.

References

1. A. Jerkstand, C. Fransson C., Kozma C. The $^{44}_{22}Ti$ – powered spectrum of SN 1987A // A&A – 2011. – Vol. 530. – Vol. A45. – P. 1-23.

2. A.I. Mihailov, I.A. Mihailov. Excitation of autoionization states of helium-like ions in the scattering of high-energy particles // JETP. – 1998. – Vol. 113, – P. 786-804.

3. P. Sigmund. Particle penetration and radiation effects. – Springer. – Berlin–Heidelberg: New York, 2006. – 500 p.

4. T.M. Potter et al. Multi-dimensional simulations of the expanding supernova remnant of SN 1987A // The Astrophysical Journal – 2014. – Vol. 794. – P. 174 (26pp).

5. J.S. Kaastra, R. Mewe. X-ray emission from thin plasmas. I-Multiple Auger ionisation and fluorescence processes for Be to Zn // Astronomy & Astrophysics Supl. Ser. – 1993. – Vol 97. – P. 443.

6. F. Varosi, E. Dwek. Analytical approximations for calculating the escape and absorption of radiation in clumpy dusty environment // The Astrophysical Journal. – 1999. – Vol. 523. – P. 265 (50pp).

7. M.V. Popov, A.A. Filina, A.A. Baranov, P. Chardonet, V.M. Chechetkin. Aspherical nucleosynthesis in a core-collapse supernova with $25M_{\odot}$ standard progenitor // The Astrophysical Journal. – 2014. – Vol. 783. – P. 43.

8. S. E. Woosley. SN 1987A-After the peak // The Astrophysical Journal. –1988. – Vol. 330. – P. 218.

9. E. Müller, B. Fryxell, D. Arnett. Instability and clumping in SN 1987A // Astronomy & Astrophysics – 1991. – Vol. 251. – P. 505-514.

10. E. Dwek, R.G. Arendt. Dust-gas interactions and the infrared emission from hot astrophysical plasmas // Ann Rev. Astron. Astrophys. – 1992. – Vol. 39. – P. 11-50.

11. D.E. Osterbrok. Astrophysics of gaseous nebulae and active galactic nuclei – Mill Valley: Univ. Sci.- 1989.

12. L.B. Lucy, I.J. Danziger, C. Guiffes, D. Bouchet. Dust condensation in the ejecta of SN 1987A, II. In Supernovae. ed. S.E.Woosley – New York, Springer. 1991. –P. 82-94.

13. I.S. Shklovskii. Supernovae stars and problems associated with them. – Moscow: Nauka, 1976. – 439 p. (in Russian)

14. Ya.B. Zeldovich, Yu. P. Raizer. The physics of shock waves and high temperature hydrodynamics phenomena. – Moscow: Nauka, – 1966. (in Russian).

15. T. Kazasa, H. Yasegava, K. Nomoto. Fjrmation of dust grains in the ejecta of SN 1987A // The Astrophysical Journal. – 1989. – Vol. 344. – P. 325-331.

16. S.A. Grebenev, A.A. Lutovinov, S.S. Tsygankov. Hard-X-ray emission lines from the decay of 44Ti in the remnant of supernova 1987A // Nature – 2012. – Vol. 490. – P. 373.

17. D.N. Doikov, S.M. Anrievsky. Ionisation loss and shock excitation of $^{44}_{20}$Ca i and $^{44}_{20}$Ca II atoms in cold remnants of type II Supernovae // Odessa Astron. Publ. – 2017. – Vol. 30. – P. 63.

18. D.N. Doikov, N.V. Savchuk, A.V. Yushchenko. Radioactive molecules in SN1987A remnant // Odessa Astron. Publ. – 2017. – Vol. 30. – P. 69.

19. D.N. Doikov, S.M. Anrievsky., A.V. Yushchenko. Gas and dust emission in cold environments with enhanced content of radioactive $^{44}_{22}Ti$ isotope // Journal of Physical Studies – 2018. – Vol. 22. – P. 2091 (8p).

20. M. Longeir. Higher Energy Astrophysics. Moscow: Mir. – 1983. – (in Russian).

IRSTI 47.17.25

The abundances of heavy elements in BL138 – red giant of local group fornax dwarf spheroidal galaxy

V.F. Gopka[1], A.V. Yushchenko[2*], V.A. Yushchenko[1], A.V. Shavrina[3], S.M. Andrievsky[1,4], Y. Jeong[5] and E.P. Shereta[1]

[1]*Department of Astronomy and Astronomical Observatory, Odessa National University, 1, Marazliyvskaya St., Odessa, UA-65014, Ukraine*
[2]*Astrocamp Contents Research Institute, Goyang, 10329, Republic of Korea*
[3]*Main Astronomical Observatory, National Academy of Sciences of Ukraine, Kyiv, 03143 Ukraine*
[4]*GEPI, Observatoire de Paris-Meudon, CNRS, Universite Paris Diderot, F-92125, Meudon Cedex, France*
[5] *Daeyang College, Sejong University, Seoul 05006, Republic of Korea*
**e-email address: avyushchenko@gmail.com*

Using the spectrum obtained with FLAMES/GIRAFFE multi-object spectrograph installed at ESO Very Large Telescope we investigated the absorption lines of heavy elements in the spectrum of BL138. This red giant star belongs to one of the Local Group members – Fornax dwarf spheroidal galaxy. The abundances of 12 stable chemical elements, namely Y, Zr, Nb, Mo, Ru, La, Ce, Pr, Nd, Eu, Dy, Er, Lu, and Hf. The abundance of radioactive elements Ac and Th are also investigated. The analysis of these abundances and also previously published investigation of BL138 allowed claiming that the distribution of abundances is different from that in the solar photosphere. The signs of r-process in the abundance pattern of BL138 are not important. The production of elements from barium to hafnium can be explained by s-process. The abundances of elements from yttrium to ruthenium are lower than it can be expected in the case of s-process synthesis. That is why it can be expected that several nuclear processes took place in the synthesis of these elements. The possibility of detection the actinium absorption line in the spectrum of BL138 clearly indicate the possibility of physical process which results in continuous production of actinium in the atmosphere of BL138. The actinium abundance can be close to logN(Ac)=1.9. It can be the result of hydrogen accretion from interstellar medium on stellar photosphere. The trends of abundances with second ionization potentials of corresponding chemical elements, and also by the emissions in the profiles of hydrogen H α line confirm this identification.

Key words: fornax dwarf galaxy, late-type stars, BL138, nuclear reactions, nucleosynthesis, abundances of chemical elements, actinium.
PACS numbers: 97.10.Tk, 97.20.Li, 98.56.Wm, 98.80.Ft.

1 Introduction

Our understanding of the structure, evolution and chemical composition of the Universe is based on the stellar abundance patterns as on one of the most important keystones. The modern theory of stellar evolution was created by Burbidge et al. [1, here after B2FH]. Later Fowler [2] doubted the cosmological production of helium. It was found that the energy density of cosmic microwave background radiation, namely $\sim 4.5\times10^{-13}$ erg cm^{-3}, is equal to the energy output of helium production in stars and the hot phase of the Universe evolution is not necessary. Cosmic microwave background in this case can be explained as a reemission of stellar radiation by interstellar and intergalactic dust [3]. Burbidge [4] summarized the series of their papers on stellar evolution in the frames of cyclic Universe with typical time scale not less than 10^{11}-10^{12} years or even longer. The modern epoch is the phase of expansion.

In accordance to B2FH [1] all chemical elements heavier than Cu (Z=29) were created mainly in r- and s-processes. s-process takes place mainly in stars, more specifically in red giants; the astrophysical sites of r-process are still under discussion [5]. Many other nuclear processes were proposed also. As an example it is possible to

mention the Thorne-Żytkow objects [6] which are explained as neutron star under intensive accretion from secondary companion, the huge overabundances of elements with atomic numbers in the range from 30 to 50 are expected [7]. The recent observations of gamma ray burst GRB170817A and its arterglow [8] confirms one of the previously proposed r-process scenarios – namely the merging of two neutron stars, with r-process nucleosynthesis going to the third r-process peak (the corresponding atomic masses are close to A=195).

It should be mentioned that B2FH theory was based only on the abundances of chemical elements in Solar system and in Milky Way stars. The first investigations of high resolution spectra in other Local Group galaxies started in the 80th of previous century. Fornax dwarf spheroidal galaxy is one of the nearest satellites of our Galaxy, the member of Local Group. Here after we show preliminary results of the investigation of heavy element abundances in the atmosphere of BL138 – red giant of this satellite. In the subsequent sections we describe the observations and the abundance determinations, compare the derived abundances with previous investigations and solar system r- and s-process isotopic composition, and discuss the obtained results.

2 Observations, Data Reduction and Abundance Determination

We used the spectrum of BL138 obtained by Letarte et al. [9] using FLAMES/GIRAFFE multi-object spectrograph with high resolution setup installed at the Very Large Telescope of European Southern Observatory. The observation was made with spectral resolution R=30,000 in the wavelength intervals 5339-5608, 6119-6397, and 6308-6689 Å, signal to noise ratio is in the range from 30 to 100 for different wavelengths. Initial reduction of the spectrum was made by the authors of [9] ans is described in this paper.

We calculated synthetic spectrum of BL138 for the whole wavelength range and compare it with observed spectrum. For synthetic spectra calculations we used Kurucz program SYNTHE [10] and atmosphere parameters of BL138 derived by [9]: effective temperature T_{eff}=3939 K, surface gravity log=0.71, microturbulent velocity v_{micro}=2.3 km s^{-1}, metallicity [Fe/H]=-1.01. It allowed us to make the identification of absorption lines of heavy elements, namely elements with atomic numbers Z>30.

Comparison of observed and synthetic spectra, identification of nonblended spectral lines, and measurements of equivalent widths of these lines were made using URAN software [11]. Abundances of chemical elements were found with Kurucz [10] WIDTH9 program. Synthetic spectra calculations were made with Kurucz [10] SYNTHE program.

Table 1 contains the list of identified lines of heavy elements in the spectrum if BL138. The columns of the table contain the identification of line, the wavelength, the measured equivalent width, the used oscillator strength, the energy of low level, and the calculated abundances in the scale logN(H)=12. The last column contains the equivalent widths of the line, measured by Letarte et al. [9]. The equivalent widths and abundances for actinium and thorium lines are discussed as only the upper limits.

In the next section we will provide the abundance of actinium calculated with spectrum synthesis method, found with using URAN software [11] and Kurucz [10] SYNTHE program in semiautomatic mode. More detailed description of used methodic can be found in our previous publications.

Table 2 shows the mean abundances if chemical elements in the atmosphere of BL138. This table contains also the results, found by Letarte et al. [9]. The columns of the tables are the identification of chemical element and its ionization stage, the mean abundances with respect to the solar photosphere value taken from [12], the errors, and the number of individual spectral lines, used for this calculation in this study and in Letarte et al. [9].

Figure 1 illustrates the abundance pattern of BL138 derived in our research, and also in Letarte et al. [9].

Table 1 – Lines of heavy elements in the spectrum of BL138

Ident.	Wavelength (Å)	Eq. Width (mÅ)	log gf	E_{low} (eV)	logN	Eq. Width (mÅ) [9]
Y I	6222.578	21.5	-1.70	0.000	1.149	–
Y I	6435.004	58.1	-0.82	0.066	0.905	–
Y II	5402.774	35.5	-0.51	1.839	1.027	32.2
Y II	5509.895	109.0	-1.01	0.992	1.396	–
Y II	5544.611	22.3	-1.09	1.738	1.187	–
Zr I	5385.151	52.2	-0.71	0.519	1.381	–
Zr I	5502.149	22.3	-1.18	0.999	2.106	–
Zr I	6121.922	20.0	-1.16	0.999	1.973	–
Zr I	6127.457	110.0	-1.06	0.154	1.669	–
Zr I	6134.548	87.3	-1.28	0.000	1.403	–
Zr I	6143.203	128.0	-1.10	0.071	1.769	–
Nb I	5350.722	24.4	-0.91	0.267	0.544	–
Mo I	5533.031	72.0	-0.07	1.335	0.892	–
Mo I	5570.444	62.4	-0.34	1.335	1.040	–
Mo I	6619.134	12.9	-1.25	1.335	0.981	–
Ru I	5484.328	13.7	-1.66	1.002	1.285	–
Ru I	5456.126	27.5	-1.62	1.139	1.804	–
La II	6320.376	83.5	-1.61	0.173	0.608	80.4
La II	6390.477	67.0	-1.41	0.321	0.424	65.2
Ce II	5582.556	12.0	-0.57	1.666	1.210	–
Ce II	6570.799	20.3	-2.06	0.529	1.296	–
Pr II	5513.562	14.2	-0.81	0.923	0.393	–
Pr II	6566.762	17.0	-1.72	0.216	0.293	–
Nd II	5442.264	64.0	-0.91	0.680	0.910	–
Nd II	5485.696	41.0	-0.12	1.264	0.626	36.3
Nd II	5508.398	27.3	-1.23	0.859	0.916	–
Nd II	5533.820	23.2	-1.23	0.559	0.396	–
Nd II	5581.591	27.4	-1.19	0.859	0.870	–
Nd II	5595.802	17.5	-1.53	0.859	0.973	–
Nd II	5603.648	37.7	-1.69	0.380	0.861	–
Nd II	6183.897	30.0	-0.92	1.160	1.050	–
Nd II	6248.274	24.4	-1.05	1.225	1.154	–
Nd II	6539.924	19.9	-1.90	0.745	1.192	–
Nd II	6637.187	15.4	-0.84	1.452	1.015	–
Eu II	6645.064	72.0	0.20	1.380	0.201	69.0
Dy II	5368.200	14.0	-2.81	0.103	0.852	–
Dy II	5399.936	12.0	-2.49	0.538	1.080	–
Er II	5414.631	22.7	-2.50	0.000	0.513	–
Lu II	6221.890	43.2	-0.76	1.542	-0.059	–
Hf I	5438.741	17.6	-2.72	0.000	1.095	–
Hf I	6185.125	20.1	-2.48	0.000	0.840	–
Hf I	6386.231	18.0	-2.29	0.292	1.044	–
Hf II	6248.924	12.9	-1.62	1.497	0.954	–
Ac II	6164.750	≤14.3	-0.85	0.588	≤ -1.586	–
Th II	6619.944	≤4.0	-1.81	0.514	≤ -0.505	–
Th II	5488.629	≤5.2	-2.61	0.000	≤-0.270	–
Th II	6619.944	≤6.0	-1.81	0.514	≤-0.320	–

Table 2 – The mean abundances of heavy elements in the atmosphere of BL138

	This investigation			Letarte et al. [9]		
	ΔlogN	**σ**	**n**	**ΔlogN**	**σ**	**n**
Mg I				-1.09	0.10	3
Si I				-0.72	0.17	1
Ca I				-1.19	0.08	9
Ti I				-1.11	0.06	8
Ti II				-0.86	0.12	3
Cr I				-1.28	0.17	1
Fe I				-1.01	0.06	43
Fe II				-0.58	0.13	5
Ni I				-1.11	0.08	14
Y I	-1.14	0.12	2			
Y II	-0.97	0.15	3	-1.16	0.17	1
Zr I	-0.83	0.27	6			
Nb I	-0.89		1			
Mo I	-0.87	0.06	3			
Ru I	-0.17	0.26	2			
Ba II				-0.54	0.14	2
La II	-0.56	0.09	2	-0.59	0.17	1
Ce II	-0.29	0.04	2			
Pr II	-0.34	0.05	2			
Nd II	-0.47	0.22	11	-0.78	0.14	3
Eu II	-0.28		1	-0.28	0.17	1
Dy II	-0.09	0.11	2			
Er II	-0.38		1			
Lu II	-0.12		1			
Hf I	0.18	0.11	3			
Hf II	0.14		1			
Ac II	≤ -1.60		1			
Th II	≤ -0.49		3			

3 Discussion

Tables 1, 2 and Figure 1 show the good coincidence of our results with values obtained by Letarte et al. [9]. The star clearly exhibits the enhancement of heavy elements abundances with respect to α-process elements. The increased number of identified lines of heavy elements allows us to confirm the Letarte et al. [9] conclusion that the nucleosynthesis in AGBs is responsible for 90% of the neutron-capture elements via the s-process and only 10% is contributed by the r-process. Note that this conclusion is based in the measured abundances of only few heavy elements, namely on the abundances of yttrium, barium, lanthanum, neodymium and europium, but these abundances were found in the atmospheres of 81 stars.

We have the abundances of only 12 stable heavy elements but measured only in one star. We compare our abundances in the photosphere of BL138 and the abundances obtained in [9] with solar system r- and s-process isotopes abundance distribution taken from [13]. The result is shown in Figure 2.

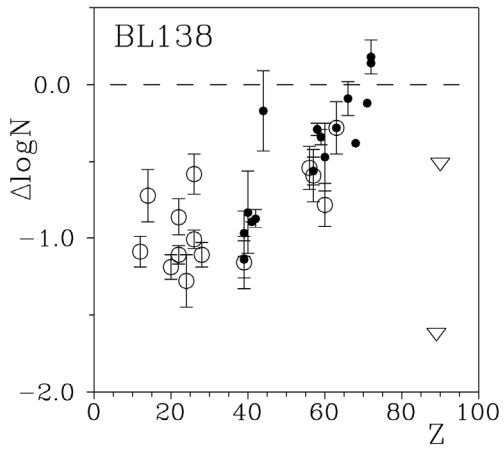

Figure 1 – The abundances of chemical elements in the photosphere of BL138 with respect to solar photosphere values. Filled circles – this investigation, open circles – Letarte et al. [9]. Triangles – upper limits for actinium and thorium abundances. Dashed line marks the solar abundances. Note that the solar system actinium abundance is not known, that is why the actinium point shows the upper limit of actinium abundance in the absolute scale logN(Ac)≤1.6 where logN(H)=12

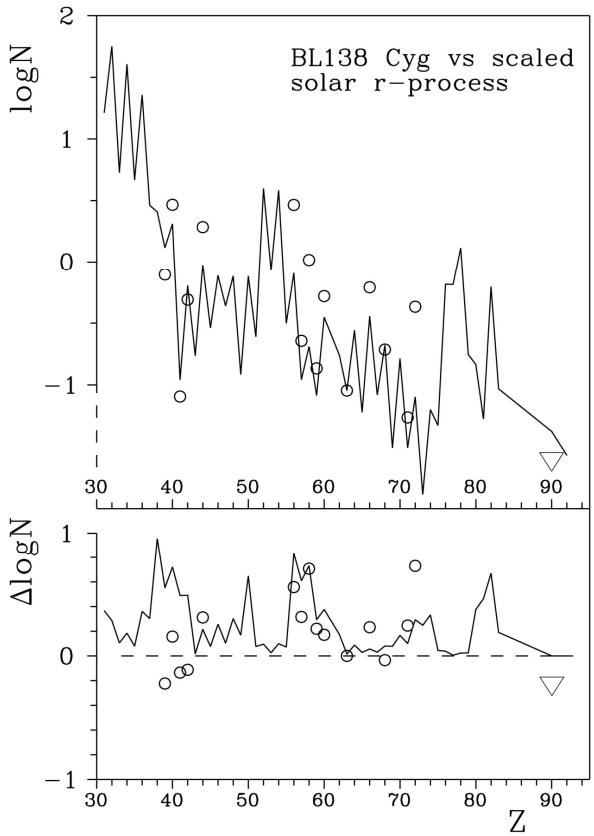

Figure 2 – Upper panel: the comparison of the surface abundances in BL138 (circles) with the solar system r-process abundance distribution [13] scaled at the observed Eu abundance (line). Triangle is the upper limit of thorium abundance. Bottom panel: the differences of observed abundances in BL138 and scaled solar system r-process abundances (circles). The line is the deviations of solar photosphere abundances from the solar r-process abundance distribution. The maximums of this curve are expected for the elements with the highest relative s-process contributions. The actinium abundance is not shown

The upper panel of this figure confirms that r-process is not important in the abundance pattern of BL138. The bottom panel indicates the increased abundances of part of s-process elements, namely, barium, lanthanides and hafnium. But the light s-process elements (yttrium to ruthenium) are relatively less abundant. s-process cannot start from barium. The abundances of elements with atomic numbers less than 56 should confirm the s-process abundance distribution, but we found the relative underabundances of these elements. It can be the result of different scenario of chemical elements synthesis in the atmosphere of BL138, and, maybe, in the Fornax dwarf galaxy.

Note that two groups of chemical elements namely the elements from yttrium to ruthenium and from barium to hafnium were clearly synthesized in different nuclear processes or under the different combinations of already known processes.

Gopka et al. [14] identified two lines of actinium in the spectrum of red supergiant RM_1-667 which belongs to other Galaxy satellite – Large Magellanic Cloud. As the longest-live actinium isotope has a half-life near 20 years it is necessary to suppose the existence of unknown physical process to generate the atoms of this unstable chemical element in the stellar atmosphere continuously. In [14] it was also pointed that one of the actinium lines can be identified in the spectrum of BL138, and that the profile of hydrogen H α line is strongly disturbed in the spectra of both stars: RM_1-667 and BL138. It was supposed that this anomaly can be the result of accretion of hydrogen atoms from interstellar medium on the surface of both RM_1-667 and BL138.

Figure 3 shows the spectrum of BL138 in the vicinity of actinium line. Synthetic spectrum method allows the stronger limitation on the abundance of this element. The actinium abundance can be close to logN(Ac)=-1.9 in the scale logN(H)=12. We used the resent investigation of oscillator strengths and partition functions for actinium [15, 16] and the new value of ionization potential of neutral actinium (5.38 eV) determined in 2012 [17]. Note that the actinium abundance in the atmosphere of RM 1-667 is logN(Ac)=-1.3±0.1 [14]. It means that the actinium abundance in the atmosphere of BL138 is at least 0.6 dex lower than the abundance of this element in RM_1-667.

Hydrogen line H α and other regions of BL138 spectrum exhibit the signs of possible emissions, more detailed inspection of all Fornax red giant stars is necessary to confirm or to reject the existence of unknown process which can continuously generate actinium in stellar atmosphere.

Figure 4 shows the relative abundances of chemical elements in the atmosphere of BL138 as a function of second ionization potentials of these elements. Greenstein [18] was the first who found these dependence and explain it as a result of charge-exchange reactions between hydrogen atoms and the atoms of other chemical elements with second ionization potentials close the the ionization potential of hydrogen atom, namely to 13.6 eV.

As a result the atoms can leave the star, produce the underabundance of certain chemical element and also brake the stellar rotational velocity. More detailed theory of this process was proposed in early 70th of the former century [19, 20] but not developed in later investigations. One of the possible results of this scenario was found to be the decreasing of rotational velocities of magnetic chemically peculiar stars of the upper main sequence.

The energy released as a result of braking the rotational velocities from several hundred kilometres per second to the observed close to zero velocity values is similar to the total energy of Galactic cosmic rays with energies less than 200 MeV/nucleon. Böhm-Vitense [21] and Yushchenko et al. [22] showed the resent observational results which can be explained by this effect. In few words the signs of this scenario were found in several hundreds usual main sequence stars, including the stars without strong magnetic fields. The detailed physical picture of this mechanism needs improvement, first of all it is necessary to investigate its observational signs in different type stars.

Figure 4 confirms the relative deficiency of chemical elements with second ionization potentials close to 13.6 eV in the atmosphere of BL138. It also confirms the trends of abundances with second ionization potentials similar to those published by Yushchenko et al. [22]. Note that Yushchenko et al. [22], as well as Bohm-Vitence [21] found these dependencies for stars with radiative photospheres, but Kang et al. [23] showed that similar dependencies can exist in convective photospheres under the condition of strong accretion of interstellar or circumstellar matter. It should be mentioned, that the energy transport in the photospheres of red giant stars are mainly radiative, that is why even small peculiarities of chemical composition created by any physical scenario can be conserved for long time.

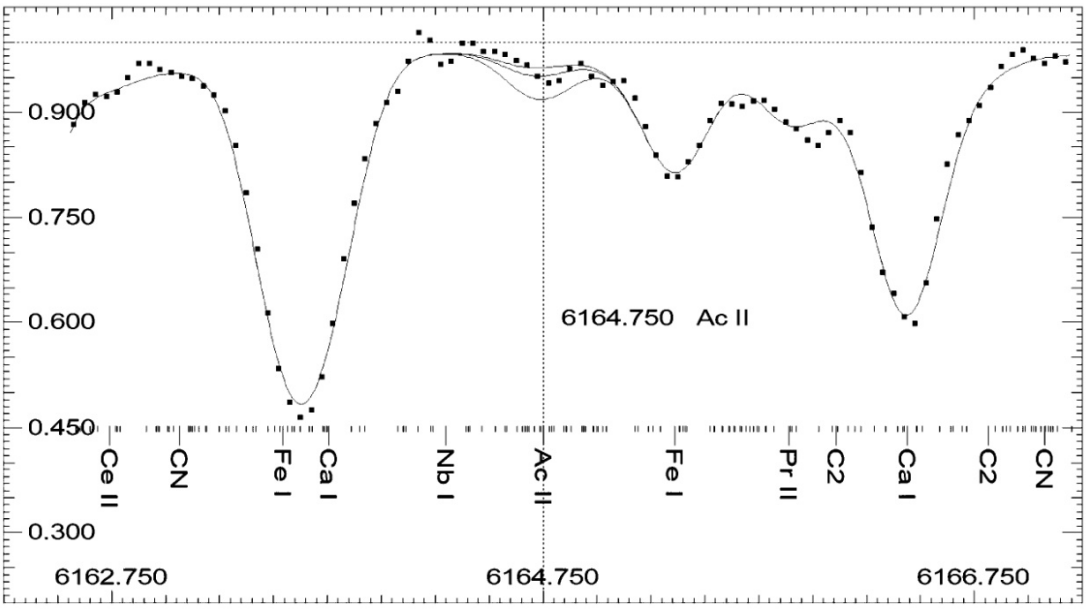

Figure 3 – The plot of BL138 spectrum in the vicinity of actinium line 6164.75 Å.
The axes are wavelength and relative flux. The points denote the observed spectrum, the lines – synthetic spectra. The positions of the spectral lines, which were taken into account in the calculations, are marked in the bottom part of the figure by short and long dashes (faint and strong lines, respectively). The identifications are shown for the strongest lines. Three synthetic spectra in the vicinity of actinium line were calculated with the best abundance of this element, and the abundances increased and decreased by 0.5 dex. The best actinium abundances is logN(Ac)=-1.9 in the scale logN(H)=12,

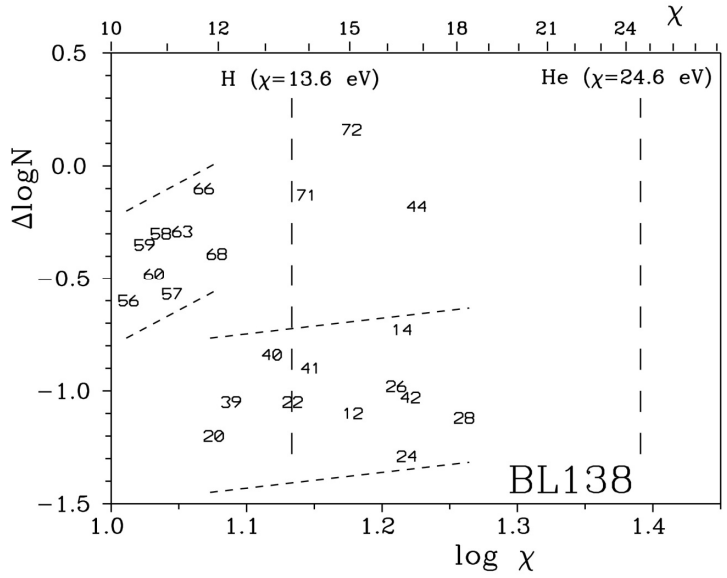

Figure 4 – Plot of relative surface abundances of chemical elements in BL138 (with respect to the solar photosphere abundances) as a function of the second ionization potentials (χ) of these elements. The positions of elements are marked by atomic numbers.
The positions of the ionization energies of hydrogen and helium are marked by vertical dashed lines. The logarithms of ionization potentials are shown on the bottom parts of the panels and the potentials themselves on the upper parts. The inclined dashed lines define the possible trends.

The relatively high abundances of several chemical elements, namely lutetium, hafnium and ruthenium can not be explained by this hypothesis. As it is shown in Figure 2 hafnium is located at one of the peaks of s-process abundance distribution. The overabundance of ruthenium as well as the relatively low abundances of yttrium to molybdenum elements can not be easily explained by any known nuclear process.

Of course, different physical scenarios should take place in the atmosphere of any star. Maybe the chemical composition of BL138, as well as of other Fornax dwarf spheroidal galaxy stars can be the result of unusual combination of well known physical processes, but the relative parts of these processes are different in giant spiral galaxy – in our Milky Way and in Fornax dwarf spheroidal galaxy.

5 Conclusions

In present paper we derived the abundances of 12 stable heavy elements in the atmosphere of BL138, and also discuss the radioactive elements, namely we found the actinium abundance and limit the abundance of thorium. Comparison of our results with earlier investigation of this star showed a good coincidence. The analysis of abundance pattern allowed the conclusion that r- and s-processes of nuclear synthesis can not fully describe the chemical composition of BL138. The most important differences are found for chemical elements from yttrium to ruthenium. It can be the result of unknown nuclear processes which took place in the evolutionary history of Fornax dwarf spheroidal galaxy.

The possible detection of actinium in the atmosphere of BL138 also confirms the necessity of new scenarios for explanation of observed abundances. One of these scenarios can be the accretion of hydrogen from interstellar medium. The signs of this accretion are observed in the distribution of elemental abundances with respect to second ionization potentials of these elements and in the profiles of strong lines.

The careful investigation of BL138 and other Fornax galaxy stars with spectrum synthesis method can confirm or reject the possible differences in evolutionary history of Milky Way and its satellites.

Acknowledgments

The authors express their gratitude to Vanessa Hill for providing us the observed spectrum of BL138.

References

1. E.M. Burbidge, G.R. Burbidge, W.A. Fowler, F. Synthesis of the elements in stars // Reviews of Modern Physics -1957. – Vol. 29. – P. 547-650.

2. W.A. Fowler. How now, no cosmological helium? // Comments on Astrophysics and Space Physics. – 1970. – Vol. 2. – P. 134-137.

3. J.V. Narlikar, R.G. Vishwakarma, A. Hajian, T. Souradeep, G. Burbidge, F. Hoyle. Inhomogeneities in the microwave background radiation interpreted within the framework of the quasi-steady state cosmology // The Astrophysical Journal. – 2003. – Vol. 585. – P. 1-11.

4. G. Burbidge. B2FH, the cosmic microwave background and cosmology // Publications of the Astronomical Society of Australia. – 2008. – Vol. 25. – P. 30-35.

5. G. Wallerstein et al. Synthesis of the elements in stars: forty years of progress // Reviews of Modern Physics. – 1997. – Vol. 69. – P. 995-1084.

6. K.S. Thorne, A.N. Żytkow. Red giants and supergiants with degenerate neutron cores // The Astrophysical Journal. – 1975. – Vol. 199. – P. L19-L24.

7. G.T. Biehle. Observational prospects for massive stars with degenerate neutron cores // The Astrophysical Journal. – 1994. – Vol. 420. – P. 364-373.

8. N.R. Tanvir et al. The emergence of a lanthanide-rich kilonova following the merger of two neutron stars // The Astrophysical Journal – 2017. – Vol. 848. – P. L27-L35.

9. B. Letarte et al. A high-resolution VLT/FLAMES study of individual stars in the centre of the Fornax dwarf spheroidal galaxy // Astronomy and Astrophysics. – 2010. – Vol. 523. – A17-A56.

10. R.L. Kurucz. Atomic data for opacity calculations // Kurucz CD-ROM – 1993. – No. 1–2. (Smithsonian Astrophys. Obs., Cambridge, MA, 1993).

11. A.V. Yushchenko. URAN: A software system for the analysis of stellar spectra // Proc. 20th Stellar Conf. of the Czech and Slovak Astronomical Inst., Brno, Czech Republic, Nov. 5–7, 1997, Ed. by J. Dušek (Nicolaus Copernicus Obs. and Planetarium Brno, 1998). -P. 201–204.

12. N. Grevesse, P. Scott, M. Asplund, A.J. Sauval. The elemental composition of the Sun. III. The heavy elements Cu to Th // Astronomy and Astrophysics. – 2015. – Vol. 573. – A27.

13. J. Simmerer, C. Sneden, J.J. Cowan, J. Collier, V.M. Woolf, J.E. Lawler. The rise of the s-process in the galaxy // The Astrophysical Journal. – 2004. – Vol. 617. – P. 1091–1114.

14. V.F. Gopka et al. Actinium abundance in the atmospheres of three red supergiants in the Magellanic Clouds // Kinematics and Physics of Celestial Bodies. – 2018. – Vol. 34. – P. 123–133.

15. P. Quinet, C. Argante, V. Fivet, C. Terranova, A.V. Yushchenko, É. Biémont. Atomic data for radioactive elements Ra I, Ra II, Ac I and Ac II and application to their detection in HD 101065 and HR 465 // Astronomy and Astrophysics. – 2007. – Vol. 474. – P. 307–314.

16. G. Urer, L. Ozdemir. The level structure of singly-ionized actinium // J. Korean Phys. Soc. – 2012. – Vol. 61. – P. 353–358.

17. J. Roßnagel, S. Raeder, A. Hakimi, R. Ferrer, N. Trautmann, K. Wendt. Determination of the first ionization potential of actinium // Physical Review A. – 2012. – Vol. 85. – P. 012525.

18. J.L. Greenstein. Analysis of the metallic-line stars. II. // The Astrophysical Journal. -1949. – Vol. 109. – P. 121–138.

19. O. Havnes. Abundances and acceleration mechanisms of cosmic rays // Nature – 1971. – Vol. 229. P. 548–549.

20. O. Havnes, P.S. Conti. Magnetic accretion processes in peculiar A stars // Astronomy and Astrophysics. – 1971. Vol. – 14. -P. 1–11.

21. E. Böhm-Vitense. The puzzle of the metallic line stars // The Publications of the Astronomical Society of the Pacific. – 2006. – Vol. 118. – P. 419-435.

22. A.V. Yushchenko, V.F. Gopka, Y.-W. Kang et al. The chemical composition of ρ Puppis and the signs of accretion in the atmospheres of B–F-type stars // The Astronomical Journal. – 2015. – Vol. 149. – A.59 (22 p.).

23. Y.-W. Kang, A.V. Yushchenko, K. Hong, E.F. Guinan, V.F. Gopka. Signs of accretion in the abundance patterns of the components of the RS CVn-type eclipsing binary star LX Persei // The Astronomical Journal. – 2013. – Vol. 145. – A167 (15 pp.).

IRSTI 29.15.03; 29.19.49

Description of the related and resonant states of the nuclei $^{6}_{3}$Li of the lie in the method of resonant groups

N.K. Kalzhigitov [1,*], K. Kato [2], V.S. Vasilevsky [3],
V.O. Kurmangaliyeva [1] and N. Zh. Takibayev [1]

[1]*Institute of Experimental and Theoretical Physics, 71, al-Farabi Ave., Almaty, Kazakhstan*
[2]*Nuclear Reaction Centre, Faculty of Science, Hokkaido University, Sapporo, Japan*
[3]*Bogolyubov Institute for Theoretical Physics, 14-B, Metrolohichna Str., Kiev, Ukraine*
[*]*e-mail: knurto@mail.ru*

To consider the interactions between light nuclei, as well as the nature of the nuclear forces between them, and the test was made of the coupled and resonant positions of the nucleus $^{6}_{3}$Li using the technique of the "Algebraic version of the resonant group method (AV RGM)", which takes into account the Pauli principle, and the cluster approximation. As a result, the nucleus $^{6}_{3}$Li was considered as a bound and resonant position formed by the interaction of two clusters. This approach can greatly facilitate the ongoing calculations, reducing the interaction between the set of nucleons, to the interaction of individual clusters. That's way; the calculations carried out are an example of the applicability of this technique for studying interactions between light nuclei in the low-energy region up to 10 MeV. Also, special attention has the influence of nuclear forces, which are used for the description different nucleon-nucleon potentials. Consideration of the interaction between two clusters using alternately several different nucleon-nucleon potentials will allow us to better understand and determine the nature of nuclear force, which will be manifested through the obtained parameters of the bound and resonance positions, as well as the type of the built-up phase shifts. All calculations were performed using different values of nuclear parameters and quantum numbers.

Key words: light nuclei, clusters, bound and resonance states.
PACS numbers: 21.60.Gx.

1 Introduction

The isotope of the nucleus $^{6}_{3}$Li refers to even-odd light nuclei, which are often used as a visual and effective representation of these nuclei as cluster systems [1, 2, 3, 4] for the purpose of testing and conducting methods for calculating the properties of these nuclei by modern computational programs.

Corresponding calculations were carried out taking into account cluster representations and microscopic methods [5] of the group of nuclei. Earlier, the characteristics of the nuclei were researched: $_{2}$He^{5}, $_{3}$Li^{5} and $^{6}_{3}$Li [6]. The results obtained were in agreement with earlier experimental data [7]. Moreover, a description was given of the processes associated with interactions of clusters inside the nucleus, and the interaction of nucleons with these clusters, as well as the interaction of incident particles on the cluster core [8].

When considering the states and structure of the nucleus$^{6}_{3}$Li, the interaction forces between cluster components and nucleons inside a given nucleus are of particular importance, taking into account the values of their quantum numbers: rear s, orbital angular momentum L, parity π and angular momentum J. Taking into account the peculiarities of the interactions between nucleons and clusters, three kinds of nucleon-cluster potentials were used in the proposed work: modified Hasegawa-Nagata [9, 10], potential Volkov's V2 [11] and potential of Minnesota [12]. Each of these potentials has its own peculiarities; in particular, the first of them takes into account the model three-component interaction of an alpha particle with a deuteron, including Coulomb, centrifugal and spin-orbital forces between these clusters, Volkov's potential takes into account the two-component interaction of clusters, and the Minnesota potential is based on three potentials of the

Gaussian type. Into these potentials are included the values of exchange waves for a more accurate description of nuclear interactions between nucleons and clusters.

Note that the "algebraic version of the method of resonant groups" (AV RGM) [13, 14, 15], first proposed by G. F. Filippov, proved like very effective and has been widely used in studies of the properties of various cluster structures.

This method was used by us in this work, and became the basis for the calculation programs used by us. Such a calculation technique, called "2cl_SpectrPhases.exe", was further improved by Vasilevskiy V.S. – one of the co-authors of this work [13, 14]. In this way, AV RGM is now one of the widely used methods for calculating microscopic states in cluster models. In particular, the nucleus $^{6}_{3}$Li was considered as the state of the interacting clusters α and d:

$$\alpha + d \rightarrow {}^{6}_{3}\mathrm{Li}^{*} \rightarrow \alpha + d \qquad (1)$$

Such a representation allows us to consider instead of a large number of nucleons involved in the reaction only two compact clusters. In this way, problems with a large number of interacting nucleons can be reduced to the problem of two or three bodies, which in many respects simplifies the scheme of calculating the computing time of computer systems without losing sufficient accuracy of calculations.

This method was used for numerical calculations of the reactions using the calculation program proposed here, which makes it possible to investigate in detail the amplitudes and phases of the scattering of reactions, such as reactions (1). The obtained data showed good consent with the experimental values [7]. All calculations were carried out in the low-energy range from 0 to 10 MeV, in the program "2cl_SpectrPhases.exe" programmed to calculate the reactions involving light nuclei.

2 Principal

The considered elastic scattering reactions (1) with the participation of two clusters and the formation of the nucleus $^{6}_{3}$Li were performed in the program "2cl_SpectrPhases.exe" for given initial parameters, indicating the type of interacting clusters (Table 1).

Table 1 – Types of clusters considered by the program "2cl_SpectrPhases.exe" for two cluster reactions

Clu_name_1	$^{4}_{2}$He	$^{4}_{2}$He	$^{4}_{2}$He	$^{4}_{2}$He	$^{4}_{2}$He	$^{4}_{2}$He	$^{4}_{2}$He
Clu_name_2	n	p	2n	d	t	$^{3}_{2}$He	$^{4}_{2}$He

Assuming reactions, the program always takes the first particle cluster α, using as an incident cluster the particles indicated in the tables under the group: Clu_name_2, in particular, in the framework of this work, an incident particle chooses to be deuterium d.

Then, quantum numbers of interacting clusters are inputs, which are install parameters (Table 2).

Table 2 – Nucleus and basic input parameters

Nucleus	$^{5}_{2}$He	$^{5}_{3}$Li	$^{6}_{2}$He	$^{6}_{3}$Li	$^{7}_{3}$Li	$^{7}_{4}$Be	$^{8}_{4}$Be
Na	5	5	6	6	7	7	8
tot_spin	0.5	0.5	0	1	0.5	0.5	0

In addition to the install parameters showed in Table 2, in configuration file "2cl_calc_spec.cfg", sets the parameters:

- lm – orbital angular momentum
- tot_mom – total angular momentum of the system;
- r_0 – oscillator length;
- majoran – Majorana parameter, which sets by a definite value for each of the potentials in this work. In this case, the modified Hasegawa-Nagata potential equal to – 0.0009. The Majorana parameter

chooses to reproduce the experimental value of the ground-state energy of the nucleus;

- n_ob_funs – parameter that established the number of basic functions which the wave function of the relative motion of clusters. Calculations were conducted by 200 basic functions;
- npot – parameter responsible for the selection of the nucleon-nucleon potential, which will be used in the calculations (Table 3). Their classification is embedded in the program, where each of the potentials was marked with its number. At the work used: modified Hasegawa-Nagata potential (npot = 1), Volkov's potential B2 (npot = 3) and the potential of Minnesota (npot = 6);

Table 3 – Classification of nucleon-nucleon potentials [4]

npot	Name of potentials
1	Modified Hasegawa-Nagata potential [10]
2	Volkov's potential V1 [11]
3	Volkov's potential V2 [11]
4	Brink-Boker potential B1
5	Brink-Boker potential B2
6	potential of Minnesota [12]

- E_ini, E_fin – parameters that determine the energy interval in which the phases and scattering cross sections will be calculated. The parameter E_ini specifies initial energy, E_fin sets the final energy. In this work the scattering reaction is α + d will be considered in the energy range from 0 to 10 MeV. In this connection, the parameters will have values: for start energy E_ini = 0, for final energy E_fin = 10 MeV;

After entering all the install parameters for reactions (1). Program start to calculation which task is: calculation of the Hamiltonian of two cluster systems$\hat{H}$, and phase-scattering related, also resonant positions. As a result, the wave function describing the positions of two clusters and their interactions with each other will be represented in the form [13, 14]:

$$\Psi_J = \hat{A}\{[\varphi_1(A_1)\varphi_2(A_2)]_s\psi_{LS}^J(\vec{q})\}, \quad (2)$$

where $\hat{A}$ this is an operator of the antisymmetrization – indistinguishability system from A nucleons by permutations of all nucleon pairs

$$\hat{A} = \sum_{p=1}^{N!} \varepsilon_p \hat{P_p}, \quad (3)$$

$\hat{P_p}$ – an operator that performs a permutation on A nucleons, $N!$ – the sum of all permutations in A of the particles, $\varepsilon_p = \pm 1$ – the sign of this permutation, where +1 – for an even permutation, -1 – for an odd permutation.

$\varphi_1(A_1)$ – internal wave function of nucleons(A_1) in first α – cluster, dependent on the coordinates of the first four of nucleons – $\overrightarrow{r_1}$, $\overrightarrow{r_2}$, $\overrightarrow{r_3}$, $\overrightarrow{r_4}$.

$\varphi_2(A_2)$ – internal wave function of nucleons (A_2) in the second d-cluster, which depends on the coordinates of the second part of the nucleons – $\overrightarrow{r_5}$,$\overrightarrow{r_6}$.

$\psi_{LS}^J(\vec{q})$ – the wave function of the relative motion of two clusters, in this work the alpha deuterium, which depends on the Jacobi vector.

$\vec{q}$ – the Jacobi vector, which is proportional to the vector $\vec{r}$ [8, 13, 14, 15]

$$\vec{q} = \vec{r}\sqrt{\frac{A_1A_2}{A_1+A_2}}, \quad (4)$$

where $\vec{r}$ – determines the relative distance between the centers of mass of interacting clusters [8, 13, 14].

$$\vec{r} = \left[\frac{1}{A_1}\sum_{i\in A_1}\vec{r}_i - \frac{1}{A_2}\sum_{J\in A_2}\vec{r}_j\right], \quad (5)$$

where $\vec{r}_i$ – it's coordinate of i nucleons (i = 1, 2, 3, …, A_1) from first cluster, and $\vec{r}_j$ – it's coordinate j nucleons ($j = A_1$+1, A_1+2,…, $A_1 + A_2$) from second cluster.

Internal wave functions $\varphi_1(A_1)$ and $\varphi_2(A_2)$, describing the motion of nucleons within both clusters, within the framework of the cluster approximation and the microscopic method of AV RGM, must be fixed, and constructed in the form of Slater determinants from the oscillator functions of the translationally invariant shell model [15, 16]. As a result, the functions $\varphi_1(A_1)$ and $\varphi_2(A_2)$ depend from oscillator length of r_0, inputted with install parameters.

Carrying out calculations using AV RGM, the wave function of the relative motion of the clusters $\psi_{LS}^J(q)$ can be reduced to a simple algebraic form, using for this purpose the expansion of the intercluster function with respect to the complete set of $\psi_n(q, r_0)$ of normalized radial oscillator functions in the coordinate and momentum spaces [13].

$$\psi_{LS}^J(q) = \sum_{n=4}^{\infty} C_{nL}\,\psi_{nL}(q, r_0), \quad (6)$$

$$\psi_{LS}^J(\mathrm{p}) = \sum_{n=4}^{\infty} C_{nL}\,\psi_{nL}(\mathrm{p}, r_0). \quad (7)$$

where q – vector modul $\vec{q}$ [13],

$$\psi_{nL}(q, r_0) = (-1)^n N_n r_0^{-\frac{3}{2}} \rho^L e^{-\frac{\rho^2}{2}} L_n^{L+1/2}(\rho)^2, \quad (8)$$

$$\rho = \frac{q}{r_0}, \qquad N_n = \sqrt{\frac{2\Gamma(n+1)}{\Gamma(n+L+\frac{3}{2})}},$$

$$\psi_{nL}(\mathrm{p}, r_0) = N_n r_0^{\frac{3}{2}} \rho^L e^{-\frac{\rho^2}{2}} L_n^{L+1/2}(\rho)^2, \quad (8.5)$$

$$\rho = \mathrm{p} \cdot r_0,$$

where n – number of oscillator quanta (knots),r_0 – oscillator radius, G – known gamma function [17], $L_n^{L+1/2}$ – generalized Laguerre polynomial [18], C_{nL} – Fourier coefficients.

After that, the recording of formula (2) of the total wave function of two cluster systems in the algebraic version of the method of resonant groups takes the form of a generalized Fourier series [13, 16, 19]

$$\Psi_J = \sum_{n=4}^{\infty} \mathrm{C}_{nL} \Psi_{nL}, \quad (9)$$

where

$$\Psi_{nL} = \hat{A}\{[\varphi_1(A_1)\varphi_2(A_2)]_s \psi_{nL}(q, r_0)\}, \quad (10)$$

Ψ_{nL} – This is the basis of many-particle oscillator functions, which is used to describe this cluster system of light nuclei.

Due to the presence of correct boundary conditions, this method is well used for describing the position of both continuous and discrete spectra. A feature of the AV RGM is the reduction of the problem of finding the wave function of the relative motion of clusters $\psi_{LS}^J(\vec{q})$ to the problem of finding the unknown coefficients of the Fourier expansion C_{nL}[11]. What is the wave function of the relative motion of two clusters in a discrete oscillator representation, satisfying a system of linear algebraic equations [19, 20]

$$\sum_{m=4}^{\infty}[\langle \Psi_{nL}|\hat{\mathrm{H}}|\Psi_{mL}\rangle - \mathrm{E} \cdot \langle \Psi_{nL}|\Psi_{mL}\rangle]\mathrm{C}_{mL} = 0, \quad (11)$$

where $\langle \Psi_{nL}|\hat{\mathrm{H}}|\Psi_{mL}\rangle$ are the matrix elements of the Hamiltonian between the cluster oscillator functions. Dirac brackets mean integration over spatial coordinates and summation over spin and isospin variables of all nucleons. $\langle \Psi_{nL}|\Psi_{mL}\rangle$ – the normalization of nucleus or the overlap integral of the oscillator functions (10) [19, 20]

$$\langle \Psi_{nL}|\Psi_{mL}\rangle = \delta_{n,m}\lambda_n, \quad (12)$$

where λ_n – eigenvalues of the antisymmetrization operator. At λ_n = 0 position Ψ_n is a prohibited position of Pauli. Such positions do not participate in the construction of the wave function (2) and do not describe the dynamics of two cluster systems. For this, positions only allowed Pauli principle are used, for which $\lambda_n > 0$.

Then, in carrying out the renormalization of the basis functions and the Fourier coefficients due to the influence of the antisymmetrization operator $\hat{A}$, the equation (11) was reduced to the standard matrix form of the Schrödinger equation with an orthonormal basis of the function. Because of this, has obtained endless system of linear homogeneous algebraic equations of the form [13, 20, 21]

$$\sum_{m=4}^{\infty}[\langle \bar{n}L|\hat{\mathrm{H}}|\bar{m}L\rangle - \mathrm{E} \cdot \delta_{n,m}]\bar{\mathrm{C}}_{mL} = 0, \quad (13)$$

where $\hat{\mathrm{H}}$ – multi particle nuclear Hamiltonian, E – total energy of the nuclear system, $\langle \bar{n}\mathrm{L}|\hat{\mathrm{H}}|\bar{m}L\rangle$ – matrix elements of the Hamiltonian on functions Ψ_{nL}, n and m – indexes that numbers only positions accepted by Pauli principle.

By this, the problem of solving the wave function of interacting clusters reduces to the matrix problem of the expansion of the inter cluster wave function over the complete system of oscillator functions, where the eigenvalues and eigenfunctions of the Hamiltonian. Negative eigenvalues determine the energy of bound positionsE_α, and the corresponding eigenfunctions determine the wave functions of the bound positions of Ψ_α nucleus.

The positive eigenvalues and eigenfunctions represent the state of the continuous spectrum of the nucleus.

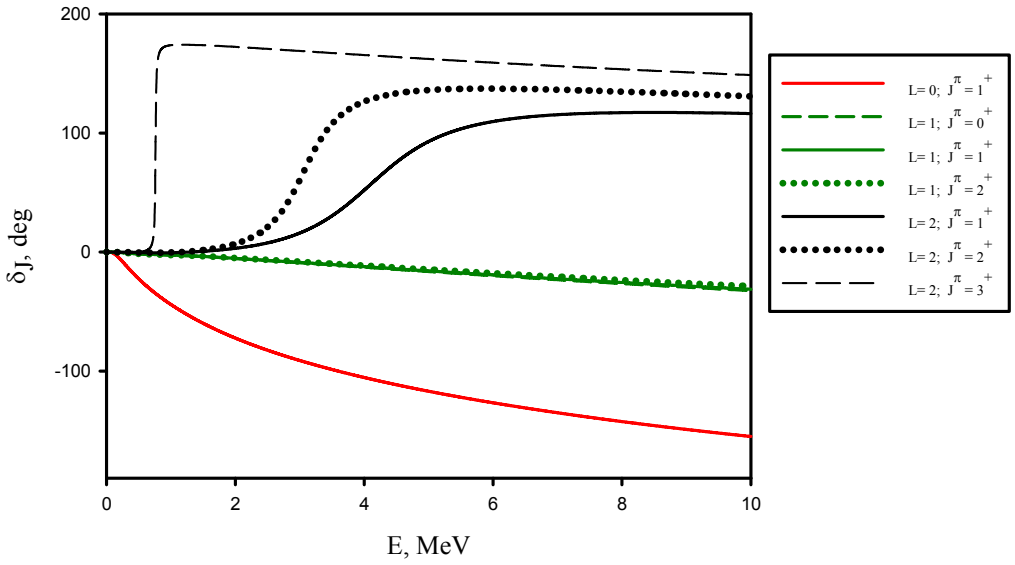

Figure 1 – The phase shifts for elastic scattering d + α constructed using the modified Hasegawa-Nagata potential

The phase shifts shown in Figure 1 were constructed using the modified Hasegawa-Nagata potential.

In the graph above (Figure 1), the built-up phase shifts showed the presence of bound positions for the values L = 0 and L = 1 through channels with values $J^{\pi} = 0^{+}$, 1^{+} , 2^{+} that they were marked with red and green lines. As the orbital angular momentum increases till L = 2 for channels with value of $J^{\pi} = 0^{+}$, 1^{+} , 2^{+} there appeared resonance positions marked with black lines. The presence of these resonance positions indicated an increase in the influence of the centrifugal barrier in the inter particle interaction and its role in the formation of resonance positions. Also, using the modified Hasegawa-Nagata potential, which takes into account not only the centrally nuclear but also the spin-orbit component, it is possible to analyze the effects of the spin component on the resonances formed and their lifetime. For what was taken into account the ratio of resonance energy to its width and lifetime: $E=\frac{\Gamma}{2}=\frac{\hbar}{2\tau}$, $\tau=\frac{\hbar}{\Gamma}$; where E – resonance energy, G – width of resonance, τ – lifetime of resonance.

The existence times of these resonance positions were determined. As a result, resonances for the values analyzed for $J^{\pi} = 1^{+}$, 2^{+} , 3^{+} showed an increase in the lifetime of the resonance with respect to the increasing value of its spin-orbit component. So it was calculated that the lifetime τ for the resonance with the value of $J^{\pi} = 3^{+}$ form $\tau = 3.43562 \times 10^{-21}$s. which was two orders of magnitude higher than the lifetime for the resonance with the value of $J^{\pi} = 1^{+}$ constituting $\tau = 2.792579 \times 10^{-23}$s. and $\tau = 6.49688 \times 10^{-23}$s. for $J^{\pi} = 2^{+}$ respectively. These values, like the phase shifts in Figure 1, showed the dependence of the resonance states and their parameters on the available quantum numbers.

Figure 2 shows the obtained phase shifts using the Volkov's potential B2.

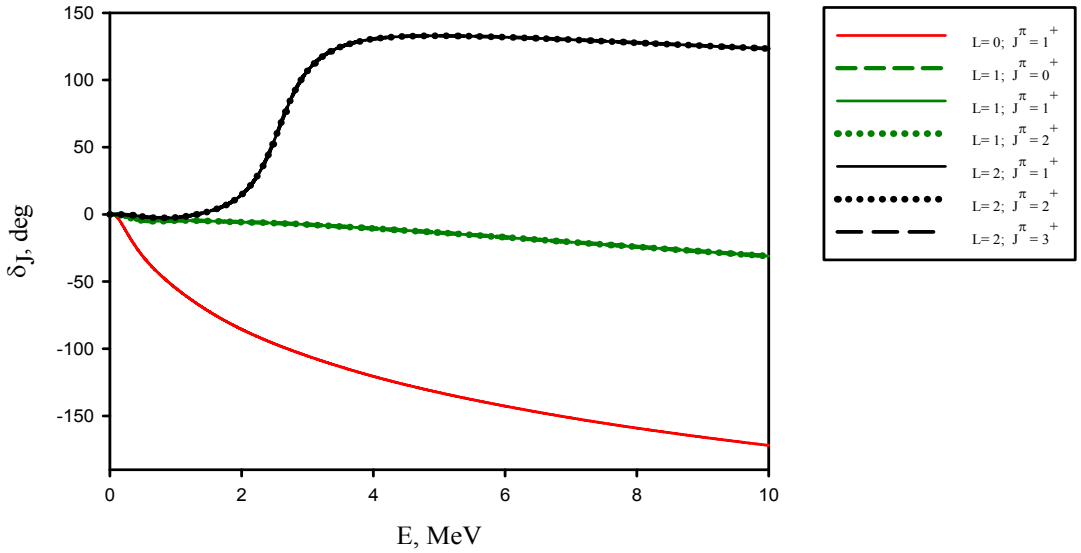

Figure 2 – The phase shifts for elastic scattering d + α constructed using the Volkov's potential V2

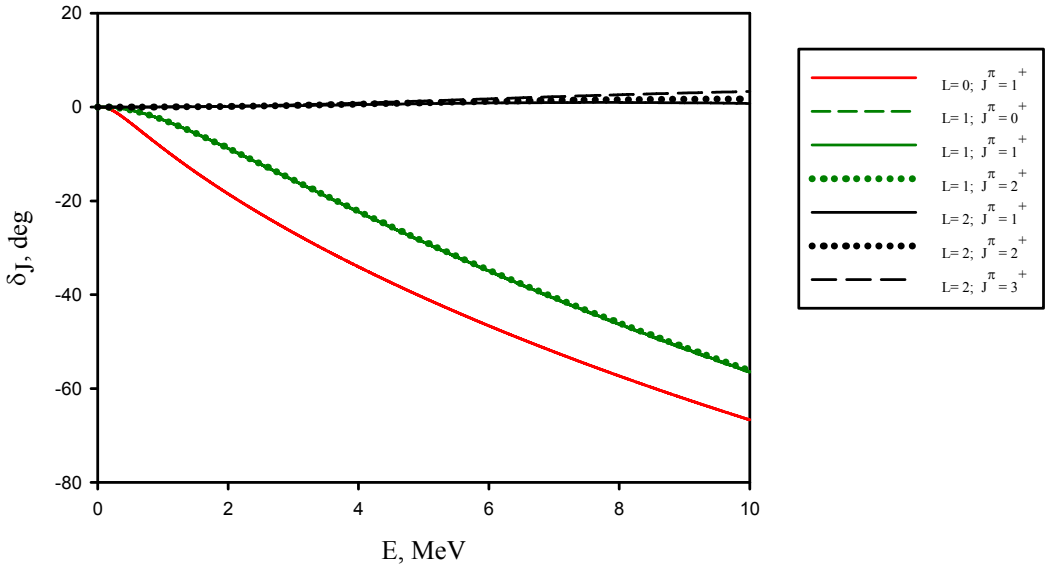

Figure 3 – The phase shifts for elastic scattering d + α constructed using the Minnesota potential

In Figure 3, the phase shifts were obtained using the Minnesota potential.

3 Results

In the result of calculations for the scattering of light nuclei α + d with the formation of bound and resonance positions in the form of a compound nucleus ^{6}Li, data were obtained describing these positions and the conditions for their appearance. All calculations were made at low energies from 0 to 10 MeV, using nucleon-nucleon potentials: Hasegawa-Nagata (modified) [10], Volkov's V2 [11] and Minnesota [12], each of which had its own exchange parameters and characteristics, which were clearly expressed in the results obtained. Due to this, the phases of scattering of bound and resonance positions were constructed, presented in Figures 1 – 3. The

scattering phase data calculated for elastic scattering of α + d with different values: of total orbital angular momentum L, total angular momentum J and definition π, which showed significant differences in the formed positions. What indicated the influence: Coulomb and centrifugal barriers on the lifetime of three formed resonance positions: $J^{\pi}= 3^{+}$, $J^{\pi}= 2^{+}$ and $J^{\pi}= 1^{+}$ at L = 2. Received scattering phases as well as the scattering phases constructed on the using of modified Hasegawa-Nagata potential showed the presence of resonant positions in the range of L = 2. However, the scattering phases obtained by using the Volkov's potential V2 shown in Figure 2 featured significant differences from our previous results obtained by using the Hasegawa-Nagata potential. It is important that in the case of the Volkov's potential there are no phase shifts in the resonances that were manifested in the case of the Hasegawa-Nagata potential. But in the case of the Volkov's potential, it turns out that the resonance generation energy for the positions with Jπ = 1+, 2+, 3+ is the same and equal to $E_{res.}$ = 2.567 MeV.

Such differences can be a consequence of the peculiarities of Volkov's' potential V2, which consists of two Gaussian functions and does not describe the interactions associated with the change in the spin and isospin parameters. In this regard, the graph presented in Figure 2 does not show changes in the scattering phases, which could be related to the influence of the spin component on them.

The Minnesota potential (Figure 3), like the modified Hasegawa-Nagata potential, takes into account the spin-orbit interaction, which is determined by three Gaussian functions. However, using the Minnesota potential to solve the problems posed and for construct the scattering phases obtained with it, the results doesn't showed the presence of resonant positions, but in this case they yielded results only for bound positions. The associated positions described by the Minnesota potential gave good consent with the results obtained using the modified Hasegawa-Nagata potential.

All values of the parameters of bound and resonant positions for different values of L and J^{π} were obtained by using various nucleon-nucleon potentials that were compared and were in consent with the experimental data. Results showed at Table 4.

Table 4 – Experimental and theoretical values of the parameters of bound and resonant positions using different nucleon-nucleon potentials

Potential	L; J^{π}	$E_{rel.}$(MeV)	$E_{res.}$(MeV)	G(MeV)
Modified Hasegawa-Nagata potential	0; 1^{+}	-1.432517	-	-
	1; 0^{+}	0.443289	-	-
	1; 1^{+}	0.443270	-	-
	1; 2^{+}	0.443229	-	-
	2; 1^{+}	0.607098	4.1	2.356595
	2; 2^{+}	0.606985	3.063	1.013097
	2; 3^{+}	0.601944	0.763	0.019158
Volkov's's potential V2	0; 1^{+}	-0.886018	-	-
	1; 0^{+}	0.403692	-	-
	1; 1^{+}	0.403692	-	-
	1; 2^{+}	0.403692	-	-
	2; 1^{+}	0.543601	2.567	0.900432
	2; 2^{+}	0.543601	2.567	0.900432
	2; 3^{+}	0.543601	2.567	0.900432
Minnesota potential	0; 1^{+}	0.348620	-	-
	1; 0^{+}	0.464726	-	-
	1; 1^{+}	0.464722	-	-
	1; 2^{+}	0.464715	-	-
	2; 1^{+}	0.640570	-	-
	2; 2^{+}	0.640567	-	-
	2; 3^{+}	0.640564	-	-
Experimental values [7]	0; 1^{+}	-1.4743	-	-
	2; 2^{+}	-	2.838 ±22	1.30 ± 100
	2; 3^{+}	-	0.712 ±2	0.024 ± 2

4 Conclusion

Calculations of the investigation of bound and resonance positions of the ^{6}Li nucleus by using the program "2cl_SpectrPhases.exe" showed the dependence of the resonant positions on the centrifugal and spin-orbit components. This dependence is particularly important in phase shifts and lifetimes of resonances with different quantum numbers. The presence of exchange parameters in the calculations and using of three nucleon-nucleon potentials made it possible to obtain the characteristics of connected and resonant positions.

It was obtained the magnitude of the exchange forces on the parameters of each of the potentials, calculated shifts of the scattering phases and an analysis of their dependences on the magnitude of the exchange forces. Thereby, was determined the potential of each components in the description of the formation of bound and resonant positions in the low-energy range.

Dispersion phases, formed as a result of work and the main characteristics of resonance states, obtained from calculations and formed in the field of low energy from 0 to 10 MeV, have given an essential information about the nature and influence of nuclear forces in system of interest. Also, comparing obtained theoretical results and experimental data, have shown applicability of the method used in this work and cluster approximation for description of reactions involving lightweight nucleus in the field of low energy.

References

1. K. Wildermuth, Y.C. Tang. A unified theory of the nucleus // Academic Press. – 1977. – Vol. 8. – P. 9-53.
2. M. Freer. Clustering in light nuclei from the stable to the exotic // Lecture Notes in Physics. – 2014. – Vol. 879. – P. 1-4.
3. J.A. Wheeler. On the mathematical description of light nuclei by the method of resonating group structure // Physical Review. – 1937. – Vol. 52. – P. 1107–1122.
4. W. von Oertzen, M. Freer., Y. Kanada-En'yo. Nuclear clusters and nuclear molecules // Physics Reports. – 2006. – Vol. 432. – P. 43-113.
5. H. Horiuchi., K. Ikeda. Cluster model of the nucleus // World Scientific Publishing Co. – 1987. – P. 43-138.
6. V.S. Vasilevsky, K. Kato, V. Kurmangaliyeva, A.D. Duisenbay, N. Kalzhigitov and N. Takibayev. Investigation of Discrete and Continuous Spectrum States in Two-Cluster Systems // Hokkaido University Collection of Scholarly and Academic Papers. – 2017. – P. 60.
7. D.R. Tilley, C.M. Cheves, J.L. Godwin, G.M. Hale, H.M. Hofmann, J.H. Kelley, C.G. Sheu, H.R. Weller. Energy levels of light nuclei A =5, 6, 7 // Nucl. Phys. A. – 2002. – Vol. 708. – P. 3–163.
8. G.F. Filippov, V.S. Vasilevsky, A.V. Nesterov. On the structure of monopole resonances of light atomic nuclei // Kiev. – 1984. – P. 32. (Preprint Inet.Theor. Phys.: ITP-84-15E).
9. A. Hasegawa, S. Nagata. Ground State of ^{6}Li // Progress of Theoretical Physics. – 1971. – Vol. 46. – P. 1786-1807.
10. F. Tanabe, A. Tohsaki, R. Tamagaki. α-α Scattering at Intermediate Energies: Applicability of Orthogonality Condition Model and Upper Limit of Isoscalar Meson-Nucleon Coupling Constants Inferred from Potential Tail // Prog. Theor. Phys. – 1975. –Vol. 53. – P. 677-691.
11. A.B. Volkov. Equilibrium deformation calculations of the ground state energies of 1p shell nuclei // Nuclear Physics. – 1965. – Vol. 74. – P. 33-58.
12. I. Reichstein, Y.C. Tang Study of N + α system with the resonating-group method // Nuclear Physics. – 1970. – A158. – P. 529-545.
13. Yu.A. Lashko, G.F. Filippov, V.S. Vasilevsky Dynamics of two-cluster systems in phase space // Nuclear Physics. – 2015. – A941. – P. 121-144.
14. G.F. Filippov, V.S. Vasilevsky, V.S.; T.P. Kovalenko. Algebraic version of resonating group method // Soviet Journal of Particles and Nuclei. – 1981. – Vol. 13. – P. 234-257.
15. G.F. Filippov, V.S. Vasilevsky, L.L. Chopovsky Solution of problems in the microscopic theory of the nucleus using the technique of generalized coherent states // Soviet Journal of Particles and Nuclei. – 1985. – Vol. 16. – P. 153–177.
16. G.F. Filippov, V.S. Vasilevsky, L.L. Chopovsky Generalized coherent states in nuclear-physics problems // Soviet Journal of Particles and Nuclei. – 1984.- Vol.15. – P.1338-1383.
17. M. Abramovitz, I. Stigan Handbook of special functions with formulas, graphs and mathematical tables // Science, Moscow. – 1979.
18. A.G. Sveshnikov, A.N. Bogolyubov, V.V. Kravtsov Lectures on mathematical physics // Moscow. – 1993. – P. 352.
19. Yu. A. Lashko, G. F. Filippov Cluster structure of a low-energy resonance in tetraneutron // Physics of Atomic Nuclei. – 2008. – Vol. 71. – P. 209–214.
20. V. S. Vasilevsky, F. Arickx, A.V. Nesterov Resonances in three-cluster continuum of ^{5}H nucleus // Yaderna Fyizika ta Energetika. – 2007. – Vol. 39. – P. 29-37.
21. V.S. Vasilevsky, F. Arickx. Algebraic model for quantum scattering: Reformulation, analysis, and numerical strategies // Physical Review A. – 1997. – Vol. 55. – P. 265–286.

IRSTI 31.23.27

Synthesis of keratin foaming agent

Zh.B. Ospanova*, K.B. Musabekov and N. Abeu

Faculty of Chemistry and Chemical Technology, al-Farabi Kazakh National University,
71, al-Farabi ave., 050040, Almaty, Kazakhstan
**e-mail: zhanar.ospanova@kaznu.kz*

The samples of technical protein foaming agents based on keratin materials like wool were obtained by method of alkaline hydrolysis. The optimal parameters for the hydrolysis of keratin-containing raw materials were established: the duration of the process was 3 hours, the concentration of the NaOH reagent solution was 5%, the reaction temperature was 403K, the feedstock ratio was NaOH = 1:7.5. Conducted by IR-spectroscopic studies of the hydrolysis reaction products were shown the identify of the samples of keratin foaming agents, obtaining at 403K and at 433K. It is established that at a temperature above 403K the quality of the product of hudrolysis significantly not improve. Proposed structure of the samples has α-helical configuration of laying chain and samples of amino acids with peptide bonds. The samples obtained by hydrolysis of keratin materials are natural surfactants and after modification ther can used as foaming agents in fire fighting and foamers for construction.

Key words: foaming agent, protein, keratin, wool, hydrolysis, foam stability, IR-spectroscopic studies.
PACS numbers: 82.80.−d.

1 Introduction

In the south of Kazakhstan accumulate huge amounts of junk rough wool of sheep. Only fine-wool Merino wool is the production of textiles, and the bulk of coarse wool, finding the application is disposed of. Therefore, the creation of coarse wool processing technology is an urgent task.

Wool is 90% composed of keratin, a fibrillar structure [1, 2], which has an α-helical form (triple woven spiral). It is composed of 20 to 23 amino acids. The basic amino acid cystine peptide residues it contains disulphide bonds which are crosslinked spaced apart remains the same or different chain polypeptide chain. These crosslinks give keratin protein insolubility in water [3].

Depending on the destination of the final product offered considerable variety of methods of destruction of keratin materials, which allow to translate the keratin in soluble form [4-6]. One widely used method is the destruction of keratin hydrolysis in the presence of denaturing agents – acids, alkalis, and salts which, when dissolved in water to form a hydrolyzed alkalis. Foaming agents obtained by hydrolysis of keratin materials are natural surfactants, and their solutions lyophilic colloids. At the interfaces they are able to form thin layers and films, which are formed as a result of surface phenomena (monolayers, asymmetrical adsorbtion layers, wettable film and symmetrical, double-sided thin film) [7, 8]. Such foaming agents are widely used in fire fighting and foams for construction [9].

The aim of this work was to determine the optimum reaction temperature hydrolysis of keratin material (wool), provides high-quality foam and IR spectroscopic study of alkaline hydrolysis products (hydrolysate) keratin, depending on the conditions of their receipt.

2 Experimental

To determine the effect on the process temperature hydrolysis hydrothermal bomb of stainless steel of at least 200 ml was charged with 20 g of wool were poured 150 ml of various concentrations of NaOH, the bomb sealed, and then the reaction mixture was

heated to the desired temperature. In this mode, the hydrolysis was carried out for a certain time. After hydrothermal bomb was cooled, and filtered hydrolyzate is neutralized with sulfuric acid solution with vigorous stirring until pH = 6 ÷ 7 [10, 11].

The foam is generated by passing air through the solution obtained foam for 1 min. Foam stability is determined by the time the destruction of the foam column.

To determine the composition and structure of the hydrolysis products pre-dried samples were keratin hydrolysates IR – Fourier spectrometer Spectrum – 65 were studied in the range 4000 – 400 cm^{-1} at room temperature.

3 Results and Discussion

In order to obtain a qualitative keratinous foaming agent, alkaline hydrolysis of wool was carried out using NaOH. The main goal at this stage of work was to establish optimal parameters for the hydrolysis of keratin-containing raw materials (duration of the process, concentration of the reagent solution, reaction temperature, raw material: solution ratio), which ensures the production of a high-quality product.

To determine the effect of the duration of hydrolysis on the quality of the reaction product, the synthesis was carried out as described above, monitoring the appearance and color of the resulting hydrolyzate every hour.

In this mode, the hydrolysis process was carried out 1, 2, 3, 4, 5 hours (Table 1). Then, the hydrothermal bombs were cooled to a temperature of 291-293K, the cooled hydrolyzate was filtered and neutralized with a solution of acetic acid with vigorous stirring to pH = 6-7.

Table 1 – Study of wool hydrolysis as a function of reaction time

Time of hydrolysis, hour	Appearance of the product and color
1	Contains unreacted wool residues
2	Contains wool particles
3	Brown
4	Dark brown
5	Dark brown

It was found that the optimum hydrolysis time is 3 hours. When the time of hydrolysis is shortened, the remainder of undissolved wool is present in the product, which indicates that the duration of hydrolysis was insufficient and the reaction did not go to the end. As the hydrolysis time increases, the resulting product becomes viscous and clots appear in it, which is undesirable.

It is known [12-14] that the wool fibers can be converted to a soluble protein using denaturants – acids, alkalis, arsenic compounds, secondary amines, trialkyl phosphines, etc. The majority of researchers, compared to acid hydrolysis keratin preferred alkaline hydrolysis. Perhaps this is due to the fact that the acid hydrolysis reactor of the manufacturer requires acid-resistant materials, increasing chain process, which leads to higher production costs.

Solubility keratin depends on the alkali concentration, treatment time and temperature. As mentioned above, obtained by hydrolysis of protein hydrolysates comprise amino acid residues that are essentially macromolecular surfactants may be used as effective foam stabilizers.

To establish the influence of temperature, hydrolysis study was carried out at a temperature of 353, 373, 403, 433K at the other parameters constant. After each reaction, the samples neutralized hydrolysate obtained and examined its foam stability. The results of studies of the effect of temperature on the quality of the foam are shown in Figure 1.

As can be seen an increase in the data base concentration decreases wool unreacted (residue) and a total yield hydrolyser ≈ 88 % increase in temperature above 403K does not significantly improve the quality of foam leads to an additional overrun of electricity, so increasing the temperature above 403K is impractical.

Naturally occurring foam constituent and surfactant proteins with intriguing structures and functions are now being identified from a variety of biological sources [15].

The relatively non-specific foaming of denatured proteins is commonplace and widely exploited in food technology and other processes [16, 17]. However, this usually requires much higher protein concentrations (typically N=10 mg ml^{-1}) and much more vigorous physical treatment (whipping and sparging) than is the case with the specialized surfactant and related proteins to be described here. The process is generally acknowledged to be associated with the higher hydrophobicity and/or increased viscosity of denatured protein

in which physical entrapment of air bubbles is facilitated in concentrated viscous mixture. This is usually the dominant mechanism in common culinary processes such as the whipping of cream or preparation of meringue from egg white, for example. Other familiar examples include the use of protein products to stabilize “instant whips”, beer foam, and other products. Denatured, fluorinated whey and soy proteins are also used on a large scale in fire-fighting foams [18, 19].

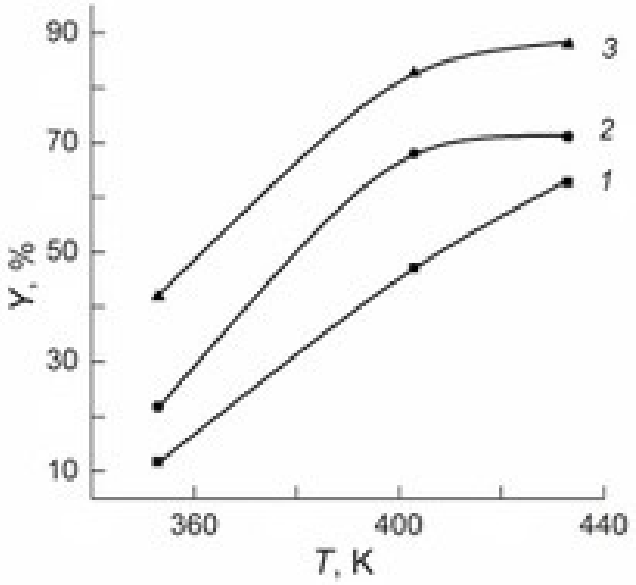

Figure 1 – Dependence of the reaction products from the hydrolysis temperature at a concentration of NaOH in the mixture:
1 – 1% 2 – 3% 3 – 5%.

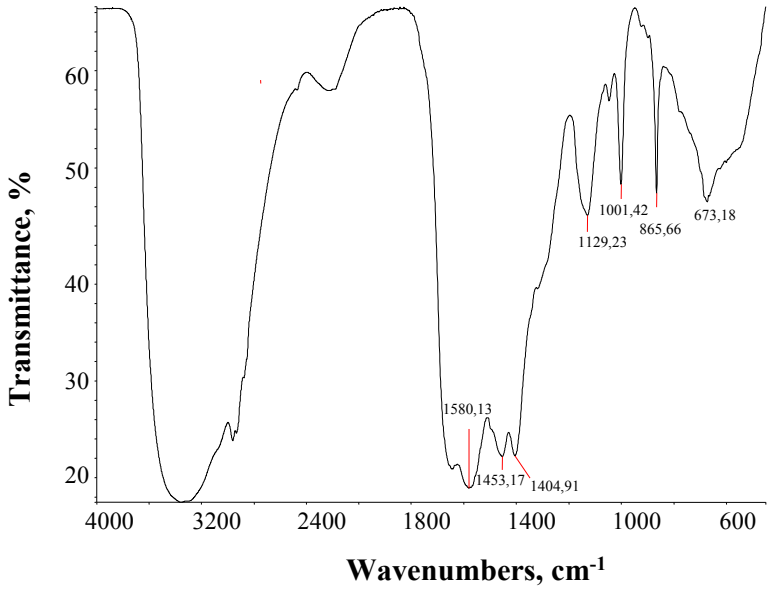

Figure 2 – The IR- spectrum of keratin hydrolysate is synthesized at 353K

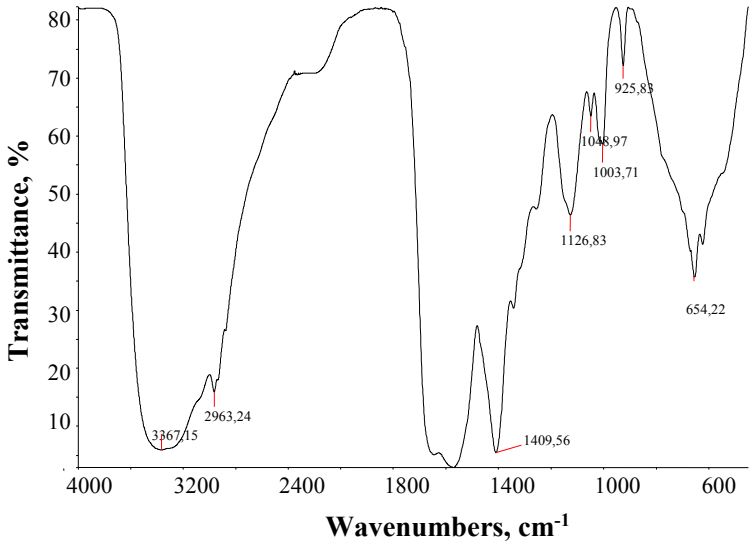

Figure 3 – The IR- spectrum of keratin hydrolysate is synthesized at 403K

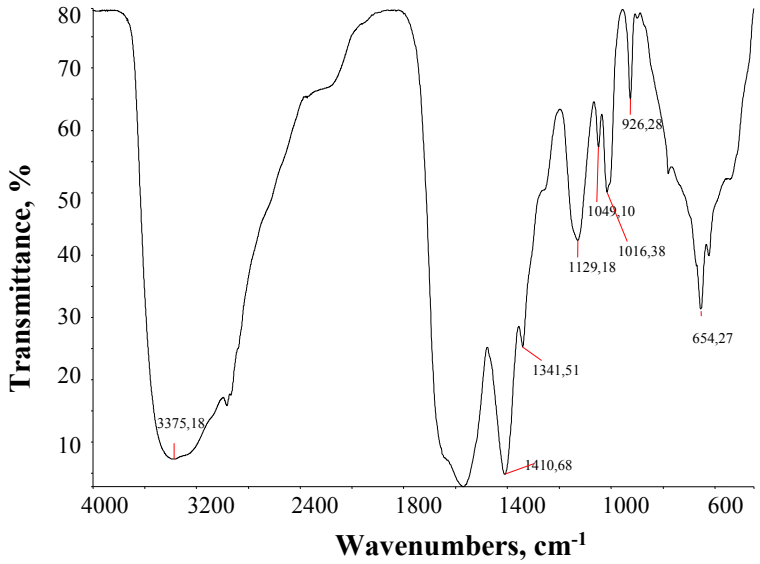

Figure 4 – The IR- spectrum of keratin hydrolysate is synthesized at 433K.

To determine the structure and composition of keratin hydrolysate were investigated IR spectra of samples hydrolysates synthesized at 353, 403, 433K. For the sample obtained at a temperature of 353K (Figure 2) fluctuations in the 3355cm^{-1} correspond to the presence of NH_2 groups, 2920 cm^{-1} – CH_2, CH, 1580cm^{-1} and 865cm^{-1} – NH groups 1453cm^{-1} and 404cm^{-1} – CH_2 and 1630 cm^{-1} – the presence of the C=O.

In the samples obtained at a temperature of 403K (Figure 3), and 433K (Figure 4). IR – spectra are virtually identical: fluctuations in 3367-3371 cm^{-1} – indicate the presence of NH_2 groups, 2963 cm^{-1} are assigned to the links CH, 1573cm^{-1} and NH – groups. Results IR – spectroscopic investigation indicates the presence of amino acids in the sample with a peptide bond.

The absorption bands in the region below 1400 cm^{-1} are associated with fluctuations, which involved the entire polypeptide backbone of the molecule. Lack of absorption bands at 1685 cm^{-1}, 1629 cm^{-1} indicates that the protein virtually no β-configuration with laying anti parallel chains [20]. This eliminates the need for a hydrolysis at higher temperatures.

Proposed structure of the samples corresponds to the content in which α- helical configuration and laying chain amino acids present in the sample with a peptide bond.

To determine the ratio of raw materials: NaOH solution conducted a series of 4 experiments. To do this, the amount of wool needed to hydrolyze was changed in the initial mixture. Raw material ratio: NaOH solution was 1:30, 1:15, 1:7.5, 1:6. All other parameters of the hydrolysis reaction remained unchanged – temperature 403K, duration of the process – 3 hours. After the end of the reaction, the stability of the foams generated from the neutralized hydrolyzate samples was determined.

The stability of foams was 1:30 – 5 minutes, 1:15 – 8 minutes, 1:7.5 – 10 minutes, 1:6 – 5 minutes without the addition of a stabilizer. As can be seen from these data, with a low content of raw materials (wool), foaming agents are formed, giving insufficiently stable foam, and an increase in the content of wool in the reaction mixture leads to the formation of a poor-quality product with low foaming capacity. It was found that the optimum ratio of raw materials: NaOH solution is 1:7.5.

Thus, as a result of the studies, the optimal parameters for the hydrolysis of keratin-containing raw materials were established: the duration of the process was 3 hours, the concentration of the NaOH reagent solution was 5%, the reaction temperature was 403K, the feedstock ratio was NaOH = 1:7.5. Conducted by IR spectroscopic studies showed the identity of keratin foam samples obtained at 403 and 433K.

4 Conclusions

As a result of the research, a technology has been developed for the synthesis of new polyfunctional foaming agents based on widely available domestic raw materials – keratin wool. It has been established that foaming of aqueous solutions of keratinous foaming agents depends on the ratio of keratin raw material, alkali, temperature and time of the process. The process was controlled by pH. Optimum parameters of hydrolysis of keratin containing raw materials (wool), ensuring the production of a quality product, were established: the duration of the process was 3 hours, the concentration of the NaOH reagent solution was 5%, the reaction temperature was 403K, the feedstock ratio was NaOH = 1:7.5.

The composition and structure of wool keratin hydrolysates synthesized at 353, 403, 433K, were studied by IR spectroscopy. The proposed structure corresponds to the content in the samples of the α-helical configuration of chain packing and the presence of peptide-bonded amino acids in the samples.

References

1. M. Cardamone, A. Nuñez, R.A. Garcia, M. Aldema-Ramos. Characterizing Wool Keratin // Research Letters in Materials Science. – 2009. – Article ID 147175. – 5 p.
2. S.G. Lieberman. Production of dry animal feed and technical fats. – Moscow: Food Industry, 1976. – 216 p.
3. L.A. Gartseva, V.V. Vasiliev Chemical technology of textile materials: the text of the lectures. – Ryazan branch of the ISTA: ISTA, 2004.-124 p.
4. L.V. Antipova, Ch.Yu. Shamkhanov, O.S. Osminin, G.A. Pozdova. Biochemical characteristics of enzymatic hydrolysis of keratin-containing Syria in the poultry processing industry // Food technology. – 2003. – No. 5-6.-S.59-64.
5. V.M. Stepanov Molecular biology. Struts and funktsii proteins. – M.: High school, 1996. – 238 p.
6. Ch.Yu. Shamkhanov, L.V. Antipova, V.F. Selemenev. Confusional changes in the protein keratin in the ego of enzymatic hydrolysis. // Food technology. – 2012. – No. 2 -3. – S. 44-45.
7. V.A. Izmailova, G.P. Yampolskaya, B.D. Summ Surface phenomena in protein systems – M.: Chemistry, 1982.-155p.
8. Cs. Kotsmar, V. Pradines, V.S. Alahverdjieva, E.V. Aksenenko, V.B. Fainerman, V.I. Kovalchuk, J. Kragel, M. Leser, B.A. Noskov, R. Miller Thermodynamics, ad-sorption kinetics and rheology of mixed protein-surfactant interfacial layers // Advances in Colloid and Interface Science. -2009. -V.150, N.1. – P.41-54.
9. E.V. Gurova Effect of alkali concentration on the physico -chemical properties of the protein keratin hydrolysates // Improving the quality of materials and road constructions: Sat. Scientific. tr. – Omsk, 2001. – P. 75-79.
10. N. Abeu, Zh. Ospanova, K. Musabekov, Zh. Toktarbay. Preliminary tests and slots for new keratin foaming agents // Mater. IV Int. Conf. on colloid chemistry and physicochemical machanics. – 2013. – CP01. – 365p.
11. Zh.B. Ospanova, K.B. Musabekov, Zh. Toktarbay, M.O. Ikakhov, O.G. Koblanova Obtaining new foam former on basic of wool keratin // Chemical Bulletin of KazNU – 2012. – № 3 (67). – P. 207-210.

12. L.S. Gorbunova, N.V. Rogachev, L.G. Vasilyeva Primary processing of wool – M.: Light and food industry, 1981.-352 p.

13. M. Feughelman // Journal of Applied Polymer Science. – V.83, 2002. – P. 489.

14. Z. Wang, M. Lienemann, M. Qiau, M.B. Linder. Mechanisms of protein adhesion on surface films of hydrophobin // Langmuir. – 2010, V.26.- P.8491–8496.

15. Reger M., Hoffmann H. Hydrophobin coated boehmite nanoparticles stabilizing oil in water emulsions// J. Colloid Interface Sci. – 2012, V.368. – P.378–386.

16. B.S. Murray, K. Durga, A. Yusoff, S.D. Stoyanov. Stabilization of foams and emulsions by mixtures of surface active food-grade particles and proteins// Food Hydrocoll. – 2011, V.25. – P.627–638.

17. H.H. Kisil', Eh.M. Sarkisyan. Obtaining amino aside preparations from waste, meat and poultry processing industry // Storage and processing of agricultural raw materials. – 2006. – №7. – P. 66-67.

18. ST RK 1609-2014 Foaming agents for extinguishing fires. General technical requirements. Test methods

19. ST RK 1608-2014 Foaming agents of a special purpose for under-layer extinguishing of fires of oil and oil products in tanks. General technical problems. Methods of Emission

20. A.V. Vassiliev, E.V. Hrynenko, A.O. Shchukin, T.G. Fedulina. Infrared spectroscopy of organic and natural products: the manual. – St. Petersburg: SPb FTA, 2007. – 54 p.